TECHNISCHE
UNIVERSITÄT
WIEN
Vienna University of Technology

INSTITUT FÜR
MECHANIK UND
MECHATRONIK
Mechanics & Mechatronics

Diplomarbeit

Nonlinear non-isothermal distributed-parameter observer for PEM Fuel Cell Systems

ausgeführt zum Zwecke der Erlangung des akademischen Grades eines Diplom-Ingenieurs
unter der Leitung von

Univ.Prof. Dr. Stefan Jakubek
Institut für Mechanik und Mechatronik
Abteilung für Regelungstechnik und Prozessautomatisierung

eingereicht an der Technischen Universität Wien

Fakultät für Maschinenwesen und Betriebswissenschaften

von

Benjamin Fuchs

Wien, am 21. November 2023

Benjamin Fuchs

Eidesstattliche Erklärung

Ich erkläre eidesstattlich, dass ich die Arbeit selbständig angefertigt, keine anderen als die angegebenen Hilfsmittel benutzt und alle aus ungedruckten Quellen, gedruckter Literatur oder aus dem Internet im Wortlaut oder im wesentlichen Inhalt übernommenen Formulierungen und Konzepte gemäß den Richtlinien wissenschaftlicher Arbeiten zitiert, durch Fußnoten gekennzeichnet bzw. mit genauer Quellenangabe kenntlich gemacht habe.

Wien, am 21. November 2023 Benjamin Fuchs

Danksagung

An dieser Stelle möchte ich mich zuerst bei meinem Betreuer, Prof. Dr. Stefan Jakubek, bedanken, welcher die vorliegende Arbeit nicht nur mit großem Engagement betreut hat und jederzeit bei Fragen bereitstand, sondern auch durch seine Vorlesungen während meines Studiums mein Interesse an der Regelungstechnik erweckt hat.

Des Weiteren gilt mein besonderer Dank Martin Vrlić und Maximilian Schelle, die bei jeglichen Anliegen immer erreichbar waren, mich bei der Erstellung dieser Diplomarbeit unterstützt haben und mich in den letzten Monaten an ihrer Arbeit teilhaben lassen. Außerdem möchte ich mich bei den Mitarbeitern der Forschungsgruppe Regelungsmethoden-Antriebssysteme des Instituts für Mechanik und Mechatronik für die interessanten Diskussionen bedanken, an denen ich teilnehmen durfte und welche sehr motiviert haben.

Ich möchte mich darüber hinaus bei meinen Studienkollegen bedanken, die mir über das ganze Studium hinweg gezeigt haben, dass mit Teamwork jede noch so große Herausforderung bewältigt werden kann und die von Kollegen zu Freunden wurden.

Besonders inniger Dank gilt meiner Freundin Viktoria, die mir auch in intensiven Phasen zur Seite stand, in jeder erdenklichen Hinsicht für mich da ist und mich jeden Tag aufs Neue motiviert.

Nicht zuletzt bedanke ich mich bei meinen Eltern, Cornelia und Karl-Heinz, die jederzeit an mich geglaubt haben und mir durch ihre jahrelange Unterstützung mein Studium und damit auch diese Arbeit ermöglicht haben.

Kurzfassung

Eine der vielversprechendsten Technologien, um klimaneutrale Energie zu erzeugen, ist die Polymerelektrolytmembran-Brennstoffzelle (PEMFC, engl. *polymer electrolyte membrane fuel cell*) unter Verwendung von grünem Wasserstoff. Trotz fortschreitender Entwicklung stellt der hochdynamische Betrieb von PEMFCs wegen des Auftretens schädlicher Betriebszustände, z.B. Austrocknen der Membran, eine Herausforderung dar. Um solche ungünstigen Betriebszustände zu vermeiden, ist es erforderlich, den Zustand der Brennstoffzelle durch Messungen entscheidender physikalischer Größen zu überwachen. Die Messung interner Größen der Brennstoffzelle erweist sich jedoch als schwierig. Um interne Zustandsgrößen dennoch nachbilden zu können, werden Zustandsbeobachter eingesetzt, welche die internen Zustände der Zelle aus gemessenen Eingangs- und Ausgangsgrößen und mithilfe eines PEMFC-Modells rekonstruieren. In dieser Arbeit wird ein Zustandsbeobachter auf Basis eines erweiterten Kalman Filters (EKF) entwickelt, dem ein nicht-isothermes quasi-2D PEMFC-Modell zugrunde liegt. Der Fokus liegt dabei auf der Schätzung der Temperaturverteilung in der Brennstoffzelle. Zusätzlich werden die Verteilungen von Stromdichte, Membran-Wasserbeladung und Gaszusammensetzungen in den Gaskanälen geschätzt. Das nicht-isotherme quasi-2D Modell hoher Ordnung wird zur Prädiktion der Zustandsverteilungen herangezogen. Für effiziente und praktikable Zustandsschätzung wird die Zustandskorrektur mithilfe eines Modells reduzierter Ordnung berechnet, welches das dominante Verhalten des Modells hoher Ordnung wiedergibt und durch ein geeignetes Verfahren zur Modellreduktion erlangt wird. Der EKF-Algorithmus wird erklärt, sowie mögliche Sensorplatzierung erörtert. Eine Beobachtbarkeitsanalyse wird im Anschluss durchgeführt. Der entwickelte Beobachter wird gegenüber einer simulierten Realität validiert und dabei mit einer Simulation ohne Beobachter verglichen. Die Ergebnisse zeigen, dass der Beobachter die Zustände schneller gegen die wahren Zustände konvergieren lässt als die Simulation ohne Beobachter, selbst mit falscher Initialschätzung der Zustände, Messrauschen und mehreren veränderlichen Systemeingängen. Abschließend wird die Schätzung ausgewählter Modellparameter in den EKF-Algorithmus eingebunden. Die Ergebnisse zeigen, dass der Beobachter zusätzlich zur Zustandsschätzung, in der Lage ist, auch anfänglich falsch gesetzte Parameter zu korrigieren.

Abstract

One of the most promising technologies for climate-neutral energy production is the polymer electrolyte membrane fuel cell (PEMFC) when using green hydrogen as fuel. Despite advancing development, highly dynamic operations are still challenging due to the potential occurrence of adverse fuel cell states, e.g., membrane drying. To avoid such operating states, the fuel cell has to be monitored by measuring vital physical quantities of the cell. However, measuring internal fuel cell states with sensors is difficult. To still reconstruct internal states, state observers are used. State observers use measured inputs and outputs and a PEMFC model to estimate the actual internal states of the fuel cell. In this thesis, a state observer based on the extended Kalman filter (EKF) algorithm is developed that uses a non-isothermal quasi-2D PEMFC model. The focus lies on the estimation of the temperature distribution within the fuel cell. Additionally, the current density and membrane water content distribution as well as the species concentrations in the gas channels are estimated. The non-isothermal quasi-2D model of high order is used to predict the state distributions. For feasible and efficient estimation, the state update is computed using a reduced-order model, obtained by a suitable model order reduction method, that retains the high-order system's dominant behavior. The EKF algorithm is explained and possible locations for sensors are discussed. An observability analysis of the system is carried out afterwards. The developed observer is validated against a simulated reality and compared to a simulation without an observer. The results show that the observer drives the states faster to the actual states than the simulation without an observer, even with wrong initialization, measurement noise, and multiple manipulable inputs. In the end, an estimation of selected model parameters is added to the EKF algorithm. The results show that the observer is also able to correct initially wrong parameters while estimating the PEMFC states accordingly.

Contents

List of Figures

List of Tables

Nomenclature

In general, bold printed lowercase letters indicate vector quantities and bold printed uppercase letters indicate matrix quantities. Tilde denotes matrices and vectors in balanced formulation. A hat denotes estimated quantities. A superscript "−" denotes predicted quantities.

Latin symbols

$a_c L_c$	electrode roughness	[1]
E_{act}	activation energy for O_2 reduction on platinum	$[\frac{\mathrm{J}}{\mathrm{mol}}]$
E_{cell}	cell potential	[V]
E_{OC}	open-circuit potential	[V]
f_1	first conductivity fitting parameter	[1]
f_2	second conductivity fitting parameter	[1]
H_{PEM}	height of the proton exchange membrane	[m]
i	current density	$[\frac{\mathrm{A}}{\mathrm{m}^2}]$
i_0	exchange current density	$[\frac{\mathrm{A}}{\mathrm{m}^2}]$
$i_{0,r}$	reference exchange current density	$[\frac{\mathrm{A}}{\mathrm{m}^2}]$
T	temperature	[K]
$T_{0,r}$	reference temperature	[K]
u, v	gas velocity along and across the cell, respectively	$[\frac{\mathrm{m}}{\mathrm{s}}]$
p	pressure	[Pa]
N	number of nodes	[1]

Greek symbols

α_c	catalyst layer transfer coefficient	[1]
γ_c	pressure dependency factor for electrochemical reaction	[1]
λ	normalised membrane water content	[1]
ρ	density of gas mixture	$[\frac{\mathrm{kg}}{\mathrm{m}^3}]$
σ	membrane ionic conductivity	$[\frac{\mathrm{S}}{\mathrm{m}}]$
ξ	species mass fraction	[1]

Physical constants

R	universal gas constant ($8.314\ \frac{\mathrm{J}}{\mathrm{mol\,K}}$)
F	Faraday constant ($96485.3365\ \frac{\mathrm{C}}{\mathrm{mol}}$)

Vectors and matrices

$\boldsymbol{\chi}$	LIT state vector
$\boldsymbol{\mathcal{A}}$	LIT matrix
$\mathfrak{b}$	LIT vector
$\boldsymbol{x}$	state vector
$\boldsymbol{u}$	input vector
$\boldsymbol{y}$	output vector
$\boldsymbol{\theta}$	parameter vector
$\boldsymbol{A}$	system matrix
$\boldsymbol{B}$	input matrix
$\boldsymbol{C}$	output matrix
$\boldsymbol{l}$	linearization offset vector
$\boldsymbol{X}_N$	state normalization matrix
$\boldsymbol{U}_N$	input normalization matrix
$\boldsymbol{Y}_N$	output normalization matrix
$\tilde{\boldsymbol{T}}$	balanced realization transformation matrix
$\boldsymbol{Q}$	process noise covariance matrix
$\boldsymbol{R}$	measurement noise covariance matrix
$\boldsymbol{P}$	error covariance matrix
$\boldsymbol{K}$	Kalman gain matrix
$\boldsymbol{S}$	innovation covariance matrix
$\boldsymbol{Q}_{ob}$	observability matrix
n_χ	order of LIT-model
n_x	number of full-order states, order of state space model
n_u	number of inputs
n_y	number of outputs
n_r	number of reduced-order states, order of reduced-order model
n_θ	number of estimated parameters

Subscripts & superscripts

cc	cathode side channel
ca	anode side channel
gdl,c	cathode side gas diffusion layer
gdl,a	anode side gas diffusion layer
mem	membrane
sl	slice
in	gas channel inlet
out	gas channel outlet
c	cathode side
a	anode side
bp	bipolar plate
k	current time step
n *or* N	normalized
r	reduced
e	eliminated
avg	average
init *or* 0	initial value
act	actual system
sim	simulation
obs	observer

Abbreviations

PEM	polymer electrolyte membrane *or* proton exchange membrane
FC	fuel cell
CFD	computational fluid dynamics
LIT	linearized in time
EOM	equation of motion (= momentum balance)
PMB	partial mass balance
TMB	total mass balance
EOS	equation of state
EB	energy balance
λB	membrane water content balance
KF	Kalman filter
EKF	extended Kalman filter
UKF	unscented Kalman filter
FCEV	fuel cell electric vehicle
GC	gas channel
GDL	gas diffusion layer
CL	catalyst layer
BP	bipolar plate
H_2	hydrogen
H_2O	water
O_2	oxygen
N_2	nitrogen

Chapter 1

Introduction

The increasing demand for climate-neutral power sources has led to the development of various concepts for the utilization of renewable energies. One of the most promising technologies regarding efficiency and energy density is the polymer electrolyte membrane fuel cell also known as proton exchange membrane fuel cell or abbreviated, PEM fuel cell or PEMFC. When using green hydrogen as fuel, PEM fuel cells represent a fully emission-free technology for electric power production. Further major benefits of PEM fuel cells are a simple structure due to the absence of moving parts, low operating noise as well as relatively low operating temperature and pressure compared to conventional power plants [1, 2].

PEM fuel cells are suitable for a wide range of application. As stationary devices of various sizes, PEMFCs can be used for the energy supply of factory sites, office buildings, and private houses. Because heat is generated as a byproduct of the electric energy production, PEM fuel cells can be utilized as a low-emission alternative to conventional combined heat and power (CHP) units. Also, portable applications like portable power generators for caravans or mobile homes are ascending [3]. In the automotive sector, PEM fuel cells are suited to be applied in numerous areas. In light vehicles such as forklifts or motorbikes as well as in passenger cars, their fast start-up and low operating noise enable them to challenge conventional combustion engines. Fast refueling gives an additional advantage in comparison to battery-powered electric vehicles that are adversely affected by long charging times [2].

Vehicles powered by PEM fuel cells are expected to be cost-competitive with conventional combustion engine vehicles soon, however, the costs of using fuel cells instead of conventional engines are relatively high at the moment. With the advancing development of the PEM fuel cell technology, production processes will be optimized for mass production, and therefore production costs will be lowered in the future [2].

1.1 Motivation

Although the development of PEMFCs is advancing further every year, and fuel cell operations have been extensively investigated experimentally and with the help of computer simulations, dynamical operations of fuel cells are still challenging due to the occurrence of potentially adverse fuel cell states, like membrane drying or flooding. To avoid such operating conditions and therefore ensure fuel cell performance and prevent damaging the cell, monitoring of critical states of the cell is necessary.

Monitoring fuel cells requires the measurement of significant physical quantities. Quantities like temperature, pressure, or voltage can usually be measured by using relatively simple measurement devices that are cost-efficient and easily applicable. For quantities like membrane humidity or species concentration measurement devices exist but are very costly and their implementation is difficult compared to simple measurement devices (e.g., thermometers). However, measuring quantities not at the inlet or outlet manifold but inside the fuel cell comes, if even possible, with high effort, not just for intricately measurable quantities like membrane humidity but also for quantities like temperature or pressure. In [4], for instance, the temperature distribution within a planar solid oxide fuel cell was measured during transient operation using comprehensive and expensive laboratory equipment. To remedy this problem and monitor internal states without directly measuring them, so-called *state observers* are used.

A state observer or state estimator is an algorithm that uses a mathematical model of the fuel cell, known inputs to the system, and easily accessible measurements to estimate the actual quantities or states that cannot be measured directly with justifiable effort. The goal of an observer is to minimize the residual between the simulated model output and the measurement of the actual system and additionally correct the simulated states in such a way that they converge toward the actual system states. The actual state estimation algorithm depends on the chosen observer approach. The model used in the observer must be able to operate in real-time and therefore must not be computationally too expensive. On the other hand, the used fuel cell model needs adequate accuracy to simulate major fuel cell effects.

1.2 Fuel cell models

Developing fast yet accurate PEMFC models usually displays a trade-off problem. Models with very little computational effort often show insufficient accuracy due to the negligence of significant fuel cell effects within the model. Conversely, models that not

only consider major fuel cell dynamics but also cover detailed effects and phenomena are rarely real-time capable due to the concomitant model size.

Numerous PEM fuel cell models of different sizes and complexity covering various fuel cell effects have been developed so far. In [5], multiple common modeling approaches were reviewed and the respective advantages and disadvantages of each approach were discussed. Models that describe steady-state fuel cell relations, e.g., [6, 7], have been introduced. The highly dynamic requirements of automotive applications, however, demand models that are capable of covering transient fuel cell effects.

The dynamics of PEM fuel cells can be modeled covering a different scope of effects. In [8], a dynamic PEMFC model of adequate size, concentrating on dynamic effects associated with reactant flow and reactant pressure was introduced. The dynamic model presented in [9] additionally covers the effects of mass and heat transport and incorporates charge double-layer capacity phenomena. Apart from reactant flow and pressure, transient phase changes of water from vapor to liquid and membrane wetting and drying effects were considered in [10].

The aforementioned dynamic models all have in common that they are constructed based on ordinary differential equations (ODEs) where the model states only depend on time alone. Such models are called zero-dimensional lumped-parameter models because no dependence on the location is considered for the states. For fuel cells particularly this means that no distributions of states, e.g., pressure drop along the gas channels, can be covered. However, for monitoring critical fuel cell operating states it is crucial to know not just one lumped value for the whole cell but to know how the states distribute throughout the individual cell domains. Models capable of multi-dimensional transient effects are described by partial differential equations (PDEs) where the state variables not only depend on time but also on the location within the cell domain. Due to their PDE character, these so-called distributed-parameter models are mostly used in discretized form to decrease computational effort which is generally higher for multi-dimensional models than for zero-dimensional models.

A one-dimensional PEM fuel cell model, developed to describe dynamic effects in temperature gradients and membrane water concentration redistribution across the fuel cell layers was proposed in [11]. For deeper insight on the distributed fuel cell effects considering more than just one dimension across the cell is essential. A two-dimensional modeling approach, as introduced in [12], is capable of describing state distributions across and along the gas channel and allows the consideration of various fuel cell effects. Three-dimensional models additionally consider a third spatial dimension transverse to

the gas channels and are therefore suitable for detailed simulations using computational fluid dynamics (CFD), as presented in [13]. However, due to their higher accuracy, 2D and 3D models are hardly applicable for real-time tasks like model-based state estimation. A compromise between computational effort and accuracy can be achieved by using quasi-2D models, where effects along the gas channels are described with a 1D approach and effects across the cell are described by 1D formulations separately. A dynamic quasi-2D isothermal PEMFC model was introduced in [14] and adapted for the non-isothermal case in [15] to additionally model the temperature distribution in the whole cell domain. Due to the achieved high accuracy and acceptable computational effort, the state estimator presented in this work will use the non-isothermal single-phase quasi-2D PEMFC model as presented in [15]. A detailed explanation of the non-isothermal quasi-2D model is given in 3.3.

1.3 State estimation algorithms

As mentioned, an observer uses a mathematical model of the system, known inputs, and measurable outputs to estimate states of the system that cannot be measured directly. Model-based state estimation knows various observer algorithms. The most common observer strategies used for internal state estimation in PEM fuel cells are characterized and reviewed in [16]. For deterministic systems that do not contain randomness in the form of measurement or process noise, Luenberger observers are a common state estimation approach [17]. However, since random noise will occur in a real system, deterministic state estimation algorithms will not be sufficient in real-life applications.

A well-established group of state estimation techniques for noise-corrupted systems are Kalman filters. Originally introduced for the use in linear systems, the Kalman filter (KF) was developed further to conquer nonlinear systems by using Jacobian matrices of nonlinear systems [18, 19]. To date, this so-called extended Kalman filter (EKF) is considered a state-of-the-art technology for state estimation problems. The Kalman filter and the extended Kalman filter are however limited to the assumption that occurring process or measurement noise is Gauss-distributed white noise. A more general algorithm that is not limited to Gaussian white noise and does not use Jacobians obtained from linearization for nonlinear systems is the unscented Kalman filter (UKF). The UKF uses sample states at specified, so-called sigma points for state estimation utilizing the so-called unscented transform [20]. Since the model equations are solved multiple times for each time step, it is not advisable to use the UKF for computationally expensive models as the quasi-2D model used in this work.

A different approach for estimating system states is the observer formulation of model predictive control (MPC), the moving horizon estimator (MHE). As with an MPC, the MHE solves a finite-horizon optimization task in every time step and is capable of considering state and input constraints [21]. Due to the quadratic optimization task that has to be solved in every time step by quadratic solvers, the MHE is computationally expensive making it inappropriate for estimating states of high-order models, like the quasi-2D PEMFC model presented in [14] and [15] that will be used in this work. Due to its well-established formulation and the fact that it does not add major computational cost, an extended Kalman filter algorithm will be used for state estimation in this thesis. Details on the algorithm can be found in 4.1.

The aim of this thesis is the development of a state observer for PEM fuel cells that allows the estimation of vital fuel cell state distributions to detect the true operating conditions of an actual cell. The observer, an extended Kalman filter, is based on the nonlinear non-isothermal quasi-2D PEMFC model presented in [15]. Therefore, a special focus will be given to the estimation of the temperature field of the cell next to other crucial state distributions, e.g., membrane water content or local current density.

In Chapter 2, the general structure of the observer is shown and the observation task is outlined. The used non-isothermal quasi-2D PEMFC model is described in detail in Chapter 3. The methods applied to obtain efficient and feasible state estimation are presented in 4. These methods include the EKF formulation, model order reduction techniques, and observability analysis of the system. Subsequently, the simulation setup and the obtained results that show the performance of the developed observer for different case studies are discussed in Chapter 5 and Chapter 6.

Chapter 2

Distributed-parameter observation problem for fuel cells

In this chapter, the overall structure of the distributed-parameter observer is shown and its functionality is explained. The difficulties of estimating distributed fuel cell states and the objectives of state estimation are outlined.

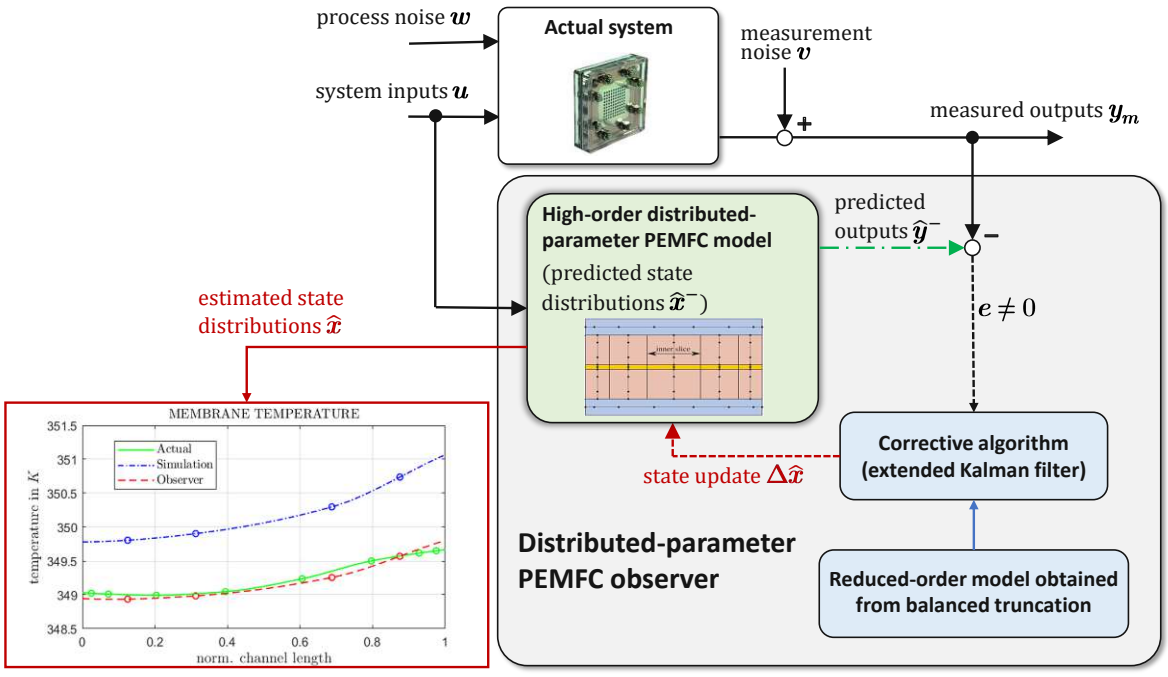

Figure 2.1: General observer structure

The general structure of the distributed-parameter observer can be seen in Fig. 2.1.

Noisy measurements of resulting system quantities, so-called outputs, $\boldsymbol{y}_m$ are taken from an actual real-life system that is affected by process noise $\boldsymbol{w}$ and manipulated by measurable boundary conditions of the system, so-called inputs, $\boldsymbol{u}$. There is no information available for internal system states that cannot be measured. The observer takes the measured system inputs $\boldsymbol{u}$ to predict the system outputs $\hat{\boldsymbol{y}}^-$ and system state distributions $\hat{\boldsymbol{x}}^-$ using the underlying model. The innovation residual $\boldsymbol{e}$ gets formed as the difference between measured output $\boldsymbol{y}_m$ and predicted output $\hat{\boldsymbol{y}}^-$. The corrective algorithm of the observer, an extended Kalman filter, then computes an update $\Delta\hat{\boldsymbol{x}}$ for the state distributions from the innovation residual $\boldsymbol{e}$. The corrected estimation of the state distributions $\hat{\boldsymbol{x}}$ is obtained by adding the state update $\Delta\hat{\boldsymbol{x}}$ to the state prediction $\hat{\boldsymbol{x}}^-$. An example of the estimated temperature distribution within the membrane is given in Fig. 2.1 as well.

For validating the observer performance in this work, a simulated reality is used as actual system since no real system would allow measurements of all vital FC states to verify the observer's estimations. This simulated reality is created by a fine-grid spatial discretization of the quasi-2D model described in 3.3. The observer itself uses a model discretized on a coarse spatial grid. This is done to create a feasible mismatch between the observer model and the real system which will always exist for a real-life system since no model is a perfect representation of reality. The investigate the convergence time of the observer, the results are compared to a simulation without corrective action. The example of the temperature distributions in Fig. 2.1 shows the three compared simulation runs, which will be discussed in more detail in Section 5.1.

The model used for state and output prediction within the observer is the presented nonlinear quasi-2D PEMFC model which is of high order due to the spatial discretization of the underlying partial differential equations. For the corrective action, however, a high-order model would increase the computational cost significantly. Furthermore, it is generally not possible for a system with several hundred states to reconstruct all states from the actual system's measurements. To remedy these problems, the corrective algorithm uses a reduced-order PEMFC model that maintains the dominant behavior of the full-order system. The model order reduction (MOR) technique to obtain th reduced-order correction model is selected to be balanced truncation. How the corrective algorithm is designed to not add significant run-time for the state correction and allow feasible estimation is shown in detail in 4.3.

The objective of the state observer presented in this thesis is the estimation of all states with the main focus lying on the following quantities:

- Temperature distribution in the fuel cell
- Normalized membrane water content distribution along the cell
- Local current density distribution along the cell
- Distribution of species concentrations in both gas channels

Especially the estimation of the temperature distribution within the fuel cell using the quasi-2D PEMFC model is of particular interest due to its innovative character. State observers for distributed-parameter PEMFC models have been investigated using an isothermal model (e.g., by Vrlić et al. [22] or Luna [23]), but to the author's best knowledge, a state observer to estimate the temperature distribution in the PEM fuel cell has not yet been introduced.

Chapter 3

Distributed-parameter non-isothermal PEM fuel cell model

In this chapter, the distributed-parameter PEMFC model for the non-isothermal case is discussed. First, a general introduction to fuel cells is given and the functionality of the PEM fuel cell is outlined. Then, the structure of the used non-isothermal quasi-2D PEMFC model is explained in detail and the strong coupling of the temperature fields to all other states through the model equations is discussed.

3.1 Historical background

The principle of fuel cells, that is generating electric current from the electrochemical reaction between hydrogen and oxygen as an inverted process of electrolysis, was discovered by C.F. Schönbein in the middle of the 19$^{\text{th}}$ century. Based on his work, Sir W. Grove later introduced the first functioning fuel cell, back then referred to as *gas battery*. The first practically applied fuel cell was developed by F.T. Bacon in the first half of the 20$^{\text{th}}$ century and was used in submarines of the Royal Navy during the 2$^{\text{nd}}$ world war. Based on Bacon's patent, Pratt & Whitney produced fuel cells for the use in the NASA Apollo space program in the 1960s. The first polymer electrolyte membrane fuel cell was invented in the 1950s by General Electric under major contributions of T. Grubb and L. Niedrach. These PEM fuel cells were used by NASA in the Gemini program from the mid-1960s on. [1, 24, 25] Since this adolescent era, (PEM) fuel cells have been further investigated and developed to be applied in various fields. In the automotive sector, General Motors presented a hydrogen-powered van in 1966 as the first fuel cell electric vehicle (FCEV). In the early 1990s, Ballard Power Systems developed a fuel cell-powered bus and Energy Partners introduced the first ever PEMFC-driven passenger car [1]. Today, the vast majority of automotive manufacturers, e.g., Toyota, are researching and developing FC-driven electric vehicles, trying to further establish

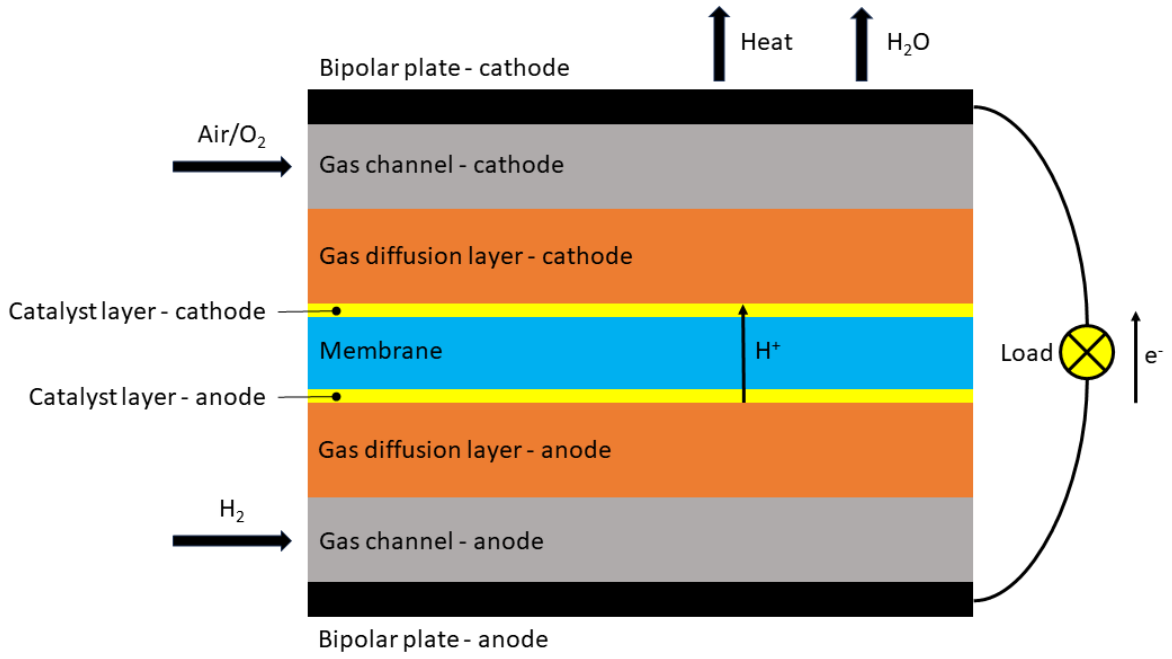

Figure 3.1: Schematic PEM fuel cell

FCEVs [24].

3.2 PEM fuel cell functionality

A PEM fuel cell uses an electrochemical reaction of hydrogen and oxygen to produce electric current and heat as a byproduct. PEM fuel cells are built up in layers. A schematic structure is shown in Figure 3.1.

Hydrogen enters the cell at the negative electrode side or anode side whereas oxygen (either pure or in air) enters at the positive electrode or cathode side. Both anode side and cathode side consist of gas channels (GCs) where the reactant is fed to the fuel cell, a gas diffusion layer (GDL) where the reactants move toward the respective catalyst layer (CL), where the reactions take place. The two sides of the cell are separated by a polymer electrolyte membrane that allows protons to travel through the membrane but is insulating to electrons. The bipolar plates (BPs) or collector plates on both sides of the fuel cell are used to transfer produced heat from the cell, separate adjacent gas channels, and conduct the cell electrically [1].

On the anode side catalyst layer, hydrogen is split up into protons and electrons. The protons travel through the membrane whereas the electrons travel through an external circuit and provide electric current at a consumer load. Equation 3.1 shows the chemical reaction on the anode side. At the cathode side catalyst layer, oxygen reacts with the protons coming through the membrane and the electrons coming from the external circuit and forms water as a product. The reaction at the cathode side is shown in Equation 3.2.

$$H_2 \longrightarrow 2H^+ + 2e^- \tag{3.1}$$

$$\frac{1}{2}O_2 + 2H^+ + 2e^- \longrightarrow H_2O \tag{3.2}$$

Combining Equations 3.1 and 3.2, the overall reaction equation for the fuel cell (3.3) can be obtained. Due to the lower formation enthalpy of the product (H_2O) compared to the formation enthalpy of the reactants (H_2 and O_2), the overall reaction is exothermic, meaning that heat will be released.

$$H_2 + \frac{1}{2}O_2 \longrightarrow H_2O + \text{heat} \tag{3.3}$$

The electric current provided by the electrons traveling from the anode side to the cathode side via the external circuit is utilized to drive electric systems, e.g., DC motors.

3.3 Non-isothermal quasi-2D PEMFC model description

As mentioned before, the PEMFC model that will be used in this work is a non-isothermal, single-phase quasi-2D model on the basis of the model introduced by Murschenhofer et al. [14] and further developed and implemented in MATLAB for the non-isothermal case by Altmann [15].

The general modeling approach can be seen in Figure 3.2. Figure 3.2a shows a 3D geometry of the cell where the red dashed lines mark the boundaries of one single cell domain to be modeled. The green 2D plane shows the considered plane for the quasi-2D approach. This considered 2D plane is shown in projected view in Figure 3.2b. The layers of the fuel cell as described in Section 3.2 are labeled and displayed differently in color. The catalyst layers of the model, located between gas diffusion layers and membrane, are assumed to be infinitely thin and therefore not shown in the graphic. The indicated black points along and across the cell are nodes of arbitrary

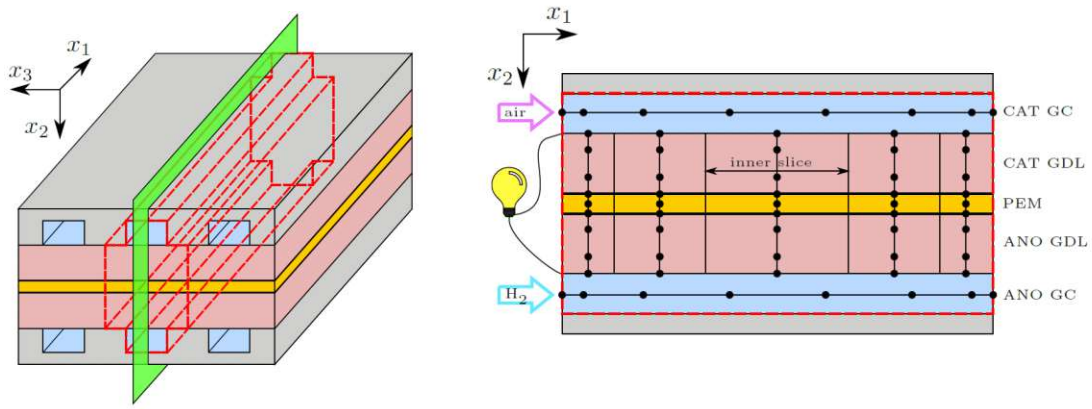

(a) (b)

Figure 3.2: Structure of PEMFC modeling domains in the quasi-2D model. (a) 3D geometry of the cell with marked 2D plane that will be considered in the model. (b) Considered 2D plane with respective modeling domains and nodes for discretization [15].

number used for spatial discretization. The model is discretized one-dimensional along the channel and one-dimensional multiple times across the gas diffusion layers (GDLs) and the membrane along an arbitrary number of so-called *inner slices*. Therefore, the discretization of the two dimensions of the modeled plane leads to an unidimensional formulation of the discretized model.

Major assumptions for the underlying model are [15]:

- The gas mixture is composed of ideal gases
- Properties of the gas mixture (viscosity, heat capacity, etc.) depend on the species composition
- Material properties are constant within the expected temperature and pressure range
- The flow, hydrodynamically and thermally, is treated as laminar and locally fully developed
- The flow is incompressible, therefore the density of the gas mixture depends only on species composition and temperature

The modeled cell domains are governed by respective partial differential and algebraic equations, e.g., equations of motion, mass balances, closure equations, equations of

state, energy balances, etc. Between the individual modeling domains, coupling conditions are applied. The electrochemical model of the non-isothermal FC model (Equations 3.4-3.6) is the same as for the isothermal case in [14] with the temperature T not being a constant for the non-isothermal model like in the isothermal model. The second and third term in the cell potential equation (Eq. 3.4) depict cathode activation polarization and ohmic losses, respectively. All applied equations for all domains are listed and explained in detail in [15].

$$E_{cell} = E_{OC} - \frac{RT}{\alpha_c F} ln(\frac{i}{i_0}) - i \int_0^{H_{PEM}} \frac{dx_2}{\sigma(\lambda)} \tag{3.4}$$

$$i_0 = i_{0,r} a_c L_c (\frac{p_{O_2}}{p_{O_2,r}})^{\gamma_c} \, exp[\frac{-E_{act}}{RT}(1 - \frac{T}{T_{0,r}})] \tag{3.5}$$

$$\sigma = (-0.326 f_1 + 0.5139 f_2 \lambda) \, exp(\frac{1286}{303} - \frac{1286K}{T}) \tag{3.6}$$

3.3.1 Gas channels

The flow in both gas channels is described by 7 state variables at each channel node:

- velocity of the gas mixture along the channel u
- oxygen mass fraction ξ_{O_2} (cathode side only)
- hydrogen mass fraction ξ_{H_2} (anode side only)
- nitrogen mass fraction ξ_{N_2} (cathode and anode side)
- water vapor mass fraction ξ_{H_2O} (cathode and anode side)
- pressure of the gas mixture p
- density of the gas mixture ρ
- temperature of the gas mixture T

For a number of N_{cc} and N_{ca} nodes in the cathode and anode channel, respectively, the state vectors for the channels $\boldsymbol{\chi}_{cc}$ and $\boldsymbol{\chi}_{ca}$ are constructed with the aforementioned states (Equation 3.7).

3.3.2 Gas diffusion layers

The states in each node of one inner slice of the GDLs are similar to the states in the channel nodes. A major difference is that the gas velocity in the GDLs v is considered across the cell and not along the channels. For a number of $N_{gdl,c}$ and $N_{gdl,a}$ nodes per inner slice in the GDL on cathode and anode side, respectively, the GDL state vectors of one arbitrary slice j from N_{sl} slices $\boldsymbol{\chi}^j_{gdl,c}$ (cathode side) and $\boldsymbol{\chi}^j_{gdl,a}$ (anode side) are displayed in Equation 3.7.

$$\boldsymbol{\chi}_{cc} = \begin{bmatrix} u_1 \\ \vdots \\ u_{N_{cc}} \\ \xi_{O_2,1} \\ \vdots \\ \xi_{O_2,N_{cc}} \\ \xi_{N_2,1} \\ \vdots \\ \xi_{N_2,N_{cc}} \\ \xi_{H_2O,1} \\ \vdots \\ \xi_{H_2O,N_{cc}} \\ p_1 \\ \vdots \\ p_{N_{cc}} \\ \rho_1 \\ \vdots \\ \rho_{N_{cc}} \\ T_1 \\ \vdots \\ T_{N_{cc}} \end{bmatrix}, \boldsymbol{\chi}_{ca} = \begin{bmatrix} u_1 \\ \vdots \\ u_{N_{ca}} \\ \xi_{H_2,1} \\ \vdots \\ \xi_{H_2,N_{ca}} \\ \xi_{N_2,1} \\ \vdots \\ \xi_{N_2,N_{ca}} \\ \xi_{H_2O,1} \\ \vdots \\ \xi_{H_2O,N_{ca}} \\ p_1 \\ \vdots \\ p_{N_{ca}} \\ \rho_1 \\ \vdots \\ \rho_{N_{ca}} \\ T_1 \\ \vdots \\ T_{N_{ca}} \end{bmatrix}, \boldsymbol{\chi}^j_{gdl,c} = \begin{bmatrix} v^j_1 \\ \vdots \\ v^j_{N_{gdl,c}} \\ \xi^j_{H_2,1} \\ \vdots \\ \xi^j_{H_2,N_{gdl,c}} \\ \xi^j_{N_2,1} \\ \vdots \\ \xi^j_{N_2,N_{gdl,c}} \\ \xi^j_{H_2O,1} \\ \vdots \\ \xi^j_{H_2O,N_{gdl,c}} \\ p^j_1 \\ \vdots \\ p^j_{N_{gdl,c}} \\ \rho^j_1 \\ \vdots \\ \rho^j_{N_{gdl,c}} \\ T^j_1 \\ \vdots \\ T^j_{N_{gdl,c}} \end{bmatrix}, \boldsymbol{\chi}^j_{gdl,a} = \begin{bmatrix} v^j_1 \\ \vdots \\ v^j_{N_{gdl,a}} \\ \xi^j_{H_2,1} \\ \vdots \\ \xi^j_{H_2,N_{gdl,a}} \\ \xi^j_{N_2,1} \\ \vdots \\ \xi^j_{N_2,N_{gdl,a}} \\ \xi^j_{H_2O,1} \\ \vdots \\ \xi^j_{H_2O,N_{gdl,a}} \\ p^j_1 \\ \vdots \\ p^j_{N_{gdl,a}} \\ \rho^j_1 \\ \vdots \\ \rho^j_{N_{gdl,a}} \\ T^j_1 \\ \vdots \\ T^j_{N_{gdl,a}} \end{bmatrix} \tag{3.7}$$

3.3.3 Membrane

In all nodes of every inner slice of the polymer electrolyte membrane, the state of the membrane is described by the membrane water content λ and the temperature T. For N_{mem} membrane nodes per slice, the membrane state vector of one arbitrary slice j from N_{sl} slices $\boldsymbol{\chi}^j_{mem}$ is shown in Equation 3.8.

$$\boldsymbol{\chi}_{mem}^{j} = \begin{bmatrix} \lambda_1^j \\ \vdots \\ \lambda_{N_{mem}}^j \\ T_1^j \\ \vdots \\ T_{N_{mem}}^j \end{bmatrix} \tag{3.8}$$

3.3.4 State-space formulation

The overall state vector is obtained by combining the individual state vectors of each domain and for each slice. Additionally, for each slice j the local current density i^j is added as a state. The cell potential (voltage) E_{cell} of the whole cell forms the last state. With the temperature being a considered state in every FC domain, the full temperature distribution within the cell can be computed by the model. The full state vector is given by

$$\boldsymbol{\chi} = \left[\begin{array}{c} \boldsymbol{\chi}_{cc} \\ \boldsymbol{\chi}_{ca} \\ \hdashline \boldsymbol{\chi}_{gdl,c}^{1} \\ \boldsymbol{\chi}_{mem}^{1} \\ \boldsymbol{\chi}_{gdl,a}^{1} \\ i^1 \\ \hdashline \vdots \\ \hdashline \boldsymbol{\chi}_{gdl,c}^{N_{sl}} \\ \boldsymbol{\chi}_{mem}^{N_{sl}} \\ \boldsymbol{\chi}_{gdl,a}^{N_{sl}} \\ i^{N_{sl}} \\ \hdashline E_{cell} \end{array}\right]. \tag{3.9}$$

The dashed lines separate the combined state vectors of individual slices of the FC. Having 7 states in each node of the gas channels and gas diffusion layers and 2 states in each membrane node, the order of the state space representation of the discretized model n_χ can be computed by

$$n_\chi = 7N_{cc} + 7N_{ca} + N_{sl}(7N_{gdl,c} + 2N_{mem} + 7N_{gdl,a} + 1) + 1. \tag{3.10}$$

The discretization of the distributed-parameter model leads to a high number of nonlinear equations. Computing the solution to this high-order system of nonlinear equations for every time step is computationally expensive. To avoid additional computational effort, the model is successively linearized in time (LIT) with respect to the previous time step, so only one iteration is required to obtain a solution to the system of equations. A detailed description of the Taylor series expansion-based LIT-methodology is given in [14] and [15]. Applying the LIT approach to all nonlinear equations yields a system of equations that is nonlinear in the states but linear in time, as given in 3.11. To compute the full state vector for the next time step $\boldsymbol{\chi}_k$, the previous state vectors $\boldsymbol{\chi}_{k-1}$, $\boldsymbol{\chi}_{k-2}$, $\boldsymbol{\chi}_{k-3}$ and the previous vector containing the inputs to the system $\boldsymbol{u}_{k-1}$ is needed.

$$\boldsymbol{\mathcal{A}}(\boldsymbol{\chi}_{k-1}, \boldsymbol{\chi}_{k-2}, \boldsymbol{\chi}_{k-3}, \boldsymbol{u}_{k-1})\boldsymbol{\chi}_k = \mathfrak{b}(\boldsymbol{\chi}_{k-1}, \boldsymbol{\chi}_{k-2}, \boldsymbol{\chi}_{k-3}, \boldsymbol{u}_{k-1}) \tag{3.11}$$

The input vector $\boldsymbol{u}$ contains all boundary conditions to the system. For an electrochemically current-driven system with pressure-driven flow, as it will be used in this work, the input vector is given by

$$\boldsymbol{u} = \begin{bmatrix} i_{avg} \\ p_{in}^{cc} \\ p_{in}^{ca} \\ p_{out}^{cc} \\ p_{out}^{ca} \\ \xi_{O_2,in}^{cc} \\ \xi_{N_2,in}^{cc} \\ \xi_{H_2,in}^{ca} \\ \xi_{H_2O,in}^{ca} \\ T_{in}^{cc} \\ T_{in}^{ca} \\ T_{bp}^{c} \\ T_{bp}^{a} \end{bmatrix}. \tag{3.12}$$

The states of the full system (Eq. 3.9) are coupled through the governing partial differential equations and coupling conditions given in [14] and [15]. For the non-isothermal case, like in this work, the coupling of the temperature to the other states is of particular interest. The structure of the system matrix $\boldsymbol{\mathcal{A}}$ in Eq. 3.11 gives detailed insight into the strong coupling between the system states and is shown in Fig. 3.3. The columns of $\boldsymbol{\mathcal{A}}$ show the respective state of the full-order state vector and the rows denote

the corresponding governing equation that couples the states. The strong coupling of the temperature to the other states is visualized by the light grey shading and marks the energy balance (EB) as the temperature's main equation (horizontal shading) and the temperatures of each domain (vertical shading). It is visible that the temperature affects all other states through the energy balance and the equation of state (EOS) as well as through coupling conditions. Because of these strong couplings, the development of a state observer based on a non-isothermal PEMFC model is a challenging task and cannot be done by simply augmenting an already developed observer based on an isothermal model, e.g., [14].

The matrices $\boldsymbol{\mathcal{A}}$ and $\mathfrak{b}$ in Eq. 3.11 are dependent on the state vectors of the last three time steps, meaning that to compute the solution of the following time step k, not just the state vector of the previous time step $k-1$ is required but also the state vectors of the two time steps before, $k-2$ and $k-3$. To obtain a system that describes the state vector solely depending on the previous time step, the LIT system from Eq. 3.11 and its state vector $\boldsymbol{\chi}$ is modified. The new, modified state vector $\boldsymbol{x}_{k-1}$ contains not just the state vector $\boldsymbol{\chi}_{k-1}$ but also the two previous state vectors $\boldsymbol{\chi}_{k-2}$ and $\boldsymbol{\chi}_{k-3}$. The composition of $\boldsymbol{x}_{k-1}$ and its evolution after one time step $\boldsymbol{x}_k$ can be seen in Eq. 3.13.

$$\boldsymbol{x}_{k-1} = \begin{bmatrix} \boldsymbol{\chi}_{k-1} \\ \boldsymbol{\chi}_{k-2} \\ \boldsymbol{\chi}_{k-3} \end{bmatrix} \quad , \quad \boldsymbol{x}_k = \begin{bmatrix} \boldsymbol{\chi}_{k} \\ \boldsymbol{\chi}_{k-1} \\ \boldsymbol{\chi}_{k-2} \end{bmatrix} \tag{3.13}$$

Abbreviating the matrices in Eq. 3.11 with $\boldsymbol{\mathcal{A}}_k$ and $\mathfrak{b}_k$, the augmented state space representation of order $n_x = 3n_\chi$ can be written as

$$\boldsymbol{x}_k = \begin{bmatrix} \boldsymbol{\chi}_{k} \\ \boldsymbol{\chi}_{k-1} \\ \boldsymbol{\chi}_{k-2} \end{bmatrix} = \begin{bmatrix} \boldsymbol{\mathcal{A}}_k^{-1}\mathfrak{b}_k \\ \boldsymbol{\chi}_{k-1} \\ \boldsymbol{\chi}_{k-2} \end{bmatrix} = \boldsymbol{f}(\boldsymbol{x}_{k-1}, \boldsymbol{u}_{k-1}). \tag{3.14}$$

The linear output equation (Eq. 3.15) maps the state vector $\boldsymbol{x}_k$ to the output vector $\boldsymbol{y}_k$ that contains the simulated measurement quantities. Which quantities are measured, i.e. where sensors are placed will be discussed in 4.4.

$$\boldsymbol{y}_k = \boldsymbol{C}\boldsymbol{x}_k \tag{3.15}$$

Equations 3.14 and 3.15 form a nonlinear state space system that will be the basis of the observer design. The spatial discretization of the model used in the observer and

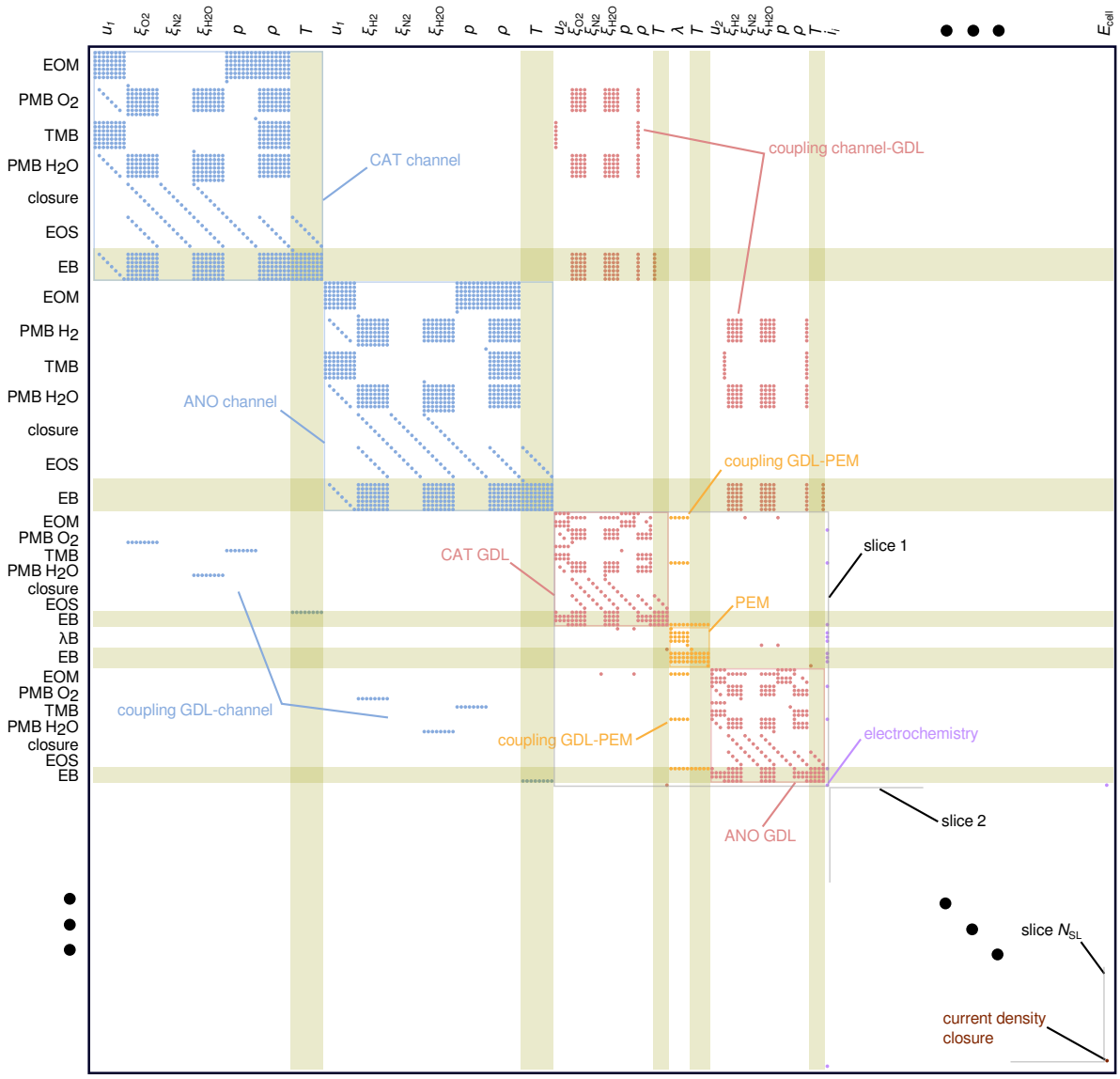

Figure 3.3: Structure of system matrix $\boldsymbol{\mathcal{A}}$. The coupling of the states and the interconnection between the domains is shown by the sparsity pattern. The blocks on the diagonal represent a certain domain, as marked in the figure. The off-diagonal entries show the coupling conditions between the domains.

the obtained order of the model will be discussed along with the simulation setup in 5.1.

Chapter 4

State estimation methodology

In this chapter, the methods used for state estimation are discussed. Detailed information about the extended Kalman filter algorithm and its application in PEMFC systems is given. To obtain the reduced-order system Jacobians for the EKF algorithm, the principle of successive linearization and a model order reduction technique, balanced truncation, are presented. Possibilities to place sensors suitable for state estimation are presented and the observability of the non-isothermal distributed-parameter system is investigated.

4.1 Extended Kalman filter

Extended Kalman filters (EKFs) have been applied numerously in PEMFC systems. Vrlić et al. [22] used an extended Kalman filter approach with model reduction methods to estimate the states of a high-order isothermal quasi-2D PEMFC model. In [26], the EKF formulation was extended to estimate constrained states of a PEMFC model. However, since the quasi-2D model used in this thesis considers closure equations for species concentrations it is not expected for estimated states to violate physical boundaries and an unconstrained formulation is sufficient.

The extended Kalman filter algorithm is, as the name implies, an extension of the ordinary Kalman filter for nonlinear systems. The Kalman filter depicts an optimal estimator of linear systems with Gauss-distributed white process and measurement noise. The difference between KF and EKF is that the EKF uses a nonlinear model to predict the states (see Fig. 2.1). However, although nonlinear systems can be handled with this extension, the EKF is no longer compulsorily an optimal estimator. The nonlinear PEMFC model (Eqs. 3.14-3.15) can be restated with considered noise by

$$\boldsymbol{x}_k = \boldsymbol{f}(\boldsymbol{x}_{k-1}, \boldsymbol{u}_{k-1}) + \boldsymbol{w}_k \tag{4.1}$$
$$\boldsymbol{y}_k = \boldsymbol{C}\boldsymbol{x}_k + \boldsymbol{v}_k, \tag{4.2}$$

where the process noise $\boldsymbol{w}_k$ and the measurement noise $\boldsymbol{v}_k$ are zero-mean, Gauss-distributed, uncorrelated white noises, each. The covariance matrices $\boldsymbol{Q}$ and $\boldsymbol{R}$ are used as tuning parameters of the observer (Eq. 4.3).

$$\boldsymbol{w}_k \sim \mathcal{N}(\boldsymbol{0}, \boldsymbol{Q}) \quad , \quad \boldsymbol{v}_k \sim \mathcal{N}(\boldsymbol{0}, \boldsymbol{R}) \tag{4.3}$$

As the ordinary Kalman filter, the EKF algorithm consists of two single steps. In the first step, the state vector and the error covariance matrix are predicted using known system inputs and the nonlinear prediction model. In the second step, taken measurements are used to update the state vector and error covariance matrix using Jacobians of the nonlinear system. Jacobians are matrices that contain information about the states' sensitivity to each other. As mentioned before, the prediction step uses the full-order nonlinear quasi-2D model from Chapter 3 and the update step uses a reduced-order modal space model which is obtained in this chapter. The reduced-order Jacobians of the modal system that are used in the EKF formulation are $\tilde{\boldsymbol{A}}_r$ which contains information about the system dynamics and $\tilde{\boldsymbol{C}}_r$ which contains information about the reduced-order modal space states' contribution to the system outputs. Their derivation is described in detail in Section 4.3 of this chapter. The reduced-order modal states are denoted by $\tilde{\boldsymbol{x}}_r$.

4.1.1 Prediction step

The nonlinear LIT-model (Eqs. 3.14-3.15) is used to predict the states $\hat{\boldsymbol{x}}_k^-$ and outputs $\hat{\boldsymbol{y}}_k^-$ of the system.

$$\hat{\boldsymbol{x}}_k^- = \boldsymbol{f}(\hat{\boldsymbol{x}}_{k-1}, \boldsymbol{u}_{k-1}) \tag{4.4}$$
$$\hat{\boldsymbol{y}}_k^- = \boldsymbol{C}\hat{\boldsymbol{x}}_k^- \tag{4.5}$$

Additionally, the $(n_r \times n_r)$ error covariance matrix is predicted a priori in modal space using the reduced-order system Jacobian $\tilde{\boldsymbol{A}}_r$ and the process noise covariance matrix in the reduced-order modal form $\tilde{\boldsymbol{Q}}$.

$$\tilde{\boldsymbol{P}}_k^- = \tilde{\boldsymbol{A}}_r \tilde{\boldsymbol{P}}_{k-1} \tilde{\boldsymbol{A}}_r^T + \tilde{\boldsymbol{Q}} \tag{4.6}$$

4.1.2 Update step

At first, the $(n_y \times n_y)$ innovation covariance matrix $\tilde{\boldsymbol{S}}$ is computed using the reduced-order output Jacobian $\tilde{\boldsymbol{C}}_r$ and the measurement covariance matrix $\boldsymbol{R}$.

$$\tilde{\boldsymbol{S}}_k = \tilde{\boldsymbol{C}}_r \tilde{\boldsymbol{P}}_k^- \tilde{\boldsymbol{C}}_r^T + \boldsymbol{R} \tag{4.7}$$

Using $\tilde{\boldsymbol{S}}_k$ from Eq. 4.7, the so-called $(n_r \times n_y)$ Kalman gain $\tilde{\boldsymbol{K}}$ is computed that maps the innovation residual to the reduced-order modal space.

$$\tilde{\boldsymbol{K}}_k = \tilde{\boldsymbol{P}}_k^- \tilde{\boldsymbol{C}}_r^T \tilde{\boldsymbol{S}}_k^{-1} \tag{4.8}$$

The measurements taken at time step k ($\boldsymbol{y}_{m,k}$) and the output prediction (Eq. 4.5) are used to compute the innovation residual $\boldsymbol{e}_k$.

$$\boldsymbol{e}_k = \boldsymbol{y}_{m,k} - \hat{\boldsymbol{y}}_k^- \tag{4.9}$$

From Eqs. 4.8 & 4.9 the reduced-order modal state update $\Delta\tilde{\boldsymbol{x}}_r$ is obtained.

$$\Delta\tilde{\boldsymbol{x}}_{r,k} = \tilde{\boldsymbol{K}}_k \boldsymbol{e}_k \tag{4.10}$$

With the back-transformation matrix from reduced modal to full state space $\boldsymbol{\mathcal{T}}$, the obtained modal state update can be transformed back to the high-order state space:

$$\Delta\hat{\boldsymbol{x}}_k = \boldsymbol{\mathcal{T}} \Delta\tilde{\boldsymbol{x}}_{r,k} \tag{4.11}$$

From the predicted state and the back-transformed state update, the corrected state estimate is obtained in the original state space:

$$\hat{\boldsymbol{x}}_k = \hat{\boldsymbol{x}}_k^- + \Delta\hat{\boldsymbol{x}}_k \tag{4.12}$$

Also, the error covariance matrix is updated in modal space using the obtained Kalman gain:

$$\tilde{\boldsymbol{P}}_k = (\boldsymbol{I} - \tilde{\boldsymbol{K}}_k \tilde{\boldsymbol{C}}_r)\tilde{\boldsymbol{P}}_k^{-}(\boldsymbol{I} - \tilde{\boldsymbol{K}}_k \tilde{\boldsymbol{C}}_r)^T + \tilde{\boldsymbol{K}}_k \boldsymbol{R} \tilde{\boldsymbol{K}}_k^T \tag{4.13}$$

Ultimately, the time step k is shifted to $k-1$ to initiate the following iteration step of the EKF algorithm. With proper tuning of the process noise covariance matrix $\tilde{\boldsymbol{Q}}$, the measurement noise covariance matrix $\boldsymbol{R}$ and the initial estimate of the error covariance matrix $\tilde{\boldsymbol{P}}_0$, the estimated states $\hat{\boldsymbol{x}}$ converge to the actual system states. The initial state error covariance matrix $\tilde{\boldsymbol{P}}_0$, which considers the initial state deviation from the actual system, is used for the first iteration and updated according to Eqs. 4.6 & 4.13 afterwards. The noise covariance matrices $\tilde{\boldsymbol{Q}}$ and $\boldsymbol{R}$ can be tuned using multiple approaches. Mostly, time-invariant matrices are used based on experience but self-tuning algorithms, as presented in [27], can be applied too. For the measurement noise covariance matrix often a diagonal matrix is used because no correlation between measurement noises is expected. The diagonal entries are then the measurement variances of the sensors. If correlation between process noises can also be expected to be non-existent, the process noise covariance matrix is also diagonal. In this work, the tuning matrices are time-invariant and are shown in the respective sections of the result chapters.

4.2 Successive linearization of PEMFC model

For the extended Kalman filter algorithm, as described in the previous section, the Jacobians of the nonlinear system are required. Therefore, the nonlinear model (Eqs. 3.14-3.15) is successively linearized around the current trajectory $(\boldsymbol{x}_{k-1}, \boldsymbol{u}_{k-1})$ to obtain the matrices of the linearized system (Eqs. 4.14-4.15).

$$\Delta \boldsymbol{x}_k = \boldsymbol{A}\Delta \boldsymbol{x}_{k-1} + \boldsymbol{B}\Delta \boldsymbol{u}_{k-1} \tag{4.14}$$

$$\Delta \boldsymbol{y}_k = \boldsymbol{C}\Delta \boldsymbol{x}_k \tag{4.15}$$

Since the output function of the original system is linear as well, no linearization is needed, and the output matrix $\boldsymbol{C}$ is retained from the original system output equation (Eq. 3.15). The system matrix $\boldsymbol{A}$ and the input matrix $\boldsymbol{B}$ are obtained from linearizing Eq. 3.14 by

$$\boldsymbol{A} = \left.\frac{\partial \boldsymbol{f}(\boldsymbol{x}_{k-1}, \boldsymbol{u}_{k-1})}{\partial \boldsymbol{x}}\right|_{\boldsymbol{x}_{k-1}, \boldsymbol{u}_{k-1}} \tag{4.16}$$

$$\boldsymbol{B} = \left.\frac{\partial \boldsymbol{f}(\boldsymbol{x}_{k-1}, \boldsymbol{u}_{k-1})}{\partial \boldsymbol{u}}\right|_{\boldsymbol{x}_{k-1}, \boldsymbol{u}_{k-1}} . \tag{4.17}$$

The vectorial function $\boldsymbol{f}(\boldsymbol{x}_{k-1}, \boldsymbol{u}_{k-1})$ contains the inverse of the high-order LIT system matrix $\boldsymbol{\mathcal{A}}_k^{-1}$. It is possible to analytically compute the derivative of the LIT system matrix $\boldsymbol{\mathcal{A}}_k$, however, due to its size it is not possible to compute its inverse $\boldsymbol{\mathcal{A}}_k^{-1}$ analytically. Therefore, the derivative of the inverse system matrix is computed using the vector calculus identity shown in Eq. 4.18 where the required inverse system matrix is obtained numerically at the current trajectory [28].

$$\frac{\partial \boldsymbol{X}^{-1}}{\partial x} = -\boldsymbol{X}^{-1}\frac{\partial \boldsymbol{X}}{\partial x}\boldsymbol{X}^{-1} \tag{4.18}$$

To obtain the Jacobians $\boldsymbol{A}$ and $\boldsymbol{B}$, the derivatives of the matrix term $\boldsymbol{\mathcal{A}}_k^{-1}\mathfrak{b}_k$ in $\boldsymbol{f}(\boldsymbol{x}_k, \boldsymbol{u}_k)$ is needed. Therefore, Eq. 4.18 and the chain rule is used:

$$\left.\frac{\partial(\boldsymbol{\mathcal{A}}_k^{-1}\mathfrak{b}_k)}{\partial \boldsymbol{x}}\right|_{\boldsymbol{x}_{k-1}, \boldsymbol{u}_{k-1}} = \left.(-\boldsymbol{\mathcal{A}}_k^{-1}\frac{\partial \boldsymbol{\mathcal{A}}_k}{\partial \boldsymbol{x}}\boldsymbol{\mathcal{A}}_k^{-1}\mathfrak{b}_k + \boldsymbol{\mathcal{A}}_k^{-1}\frac{\partial \mathfrak{b}_k}{\partial \boldsymbol{x}})\right|_{\boldsymbol{x}_{k-1}, \boldsymbol{u}_{k-1}} \tag{4.19}$$

$$\left.\frac{\partial(\boldsymbol{\mathcal{A}}_k^{-1}\mathfrak{b}_k)}{\partial \boldsymbol{u}}\right|_{\boldsymbol{x}_{k-1}, \boldsymbol{u}_{k-1}} = \left.(-\boldsymbol{\mathcal{A}}_k^{-1}\frac{\partial \boldsymbol{\mathcal{A}}_k}{\partial \boldsymbol{u}}\boldsymbol{\mathcal{A}}_k^{-1}\mathfrak{b}_k + \boldsymbol{\mathcal{A}}_k^{-1}\frac{\partial \mathfrak{b}_k}{\partial \boldsymbol{u}})\right|_{\boldsymbol{x}_{k-1}, \boldsymbol{u}_{k-1}} \tag{4.20}$$

In Eqs. 4.19 & 4.20, the inverse $\boldsymbol{\mathcal{A}}_k^{-1}$ is obtained numerically and the derivatives of $\boldsymbol{\mathcal{A}}_k$ and $\mathfrak{b}_k$ are computed using MATLAB's Symbolic Math Toolbox [29].

As described in [14], the cubic equation to compute the (normalized) membrane water content from the water vapor activity a_w is approximated by four linear functions of best fit with a_w being the switching variable, deciding which linear function is used at the current time step. This relation represents a *if-then-else*-statement which is solved by if-loops in the MATLAB code of the model. Since if-loops constitute a discontinuous relation, the loops have to be replaced by continuously differentiable functions to compute the (symbolic) derivatives of $\boldsymbol{\mathcal{A}}_k$ and $\mathfrak{b}_k$, shown in Eqs. 4.19-4.20. A similar problem was solved likewise in [10].

If-statements and their switching relations can be approximated by sigmoid functions. A switching relation of the form

$$z(x) = \begin{cases} 0, & x \leq x_{sw,1} \\ 1, & x_{sw,1} < x \leq x_{sw,2} \\ 0, & x > x_{sw,2} \end{cases} \tag{4.21}$$

can be approximated by a continuously differentiable membership function consisting of sigmoid (arc tangent) functions (Eq. 4.22). A comparison between the switching character of the if-statement and the sigmoid activation function is shown in Fig. 4.1. All if-statements within the model are replaced in that manner by respective sigmoid functions. The steepness of the arc tangent functions in the model is set to $\varepsilon = 10^6$ for all switching functions.

$$z^*(x) = \frac{1}{\pi}(\arctan(\varepsilon(x - x_{sw,1})) - \arctan(\varepsilon(x - x_{sw,2}))) \tag{4.22}$$

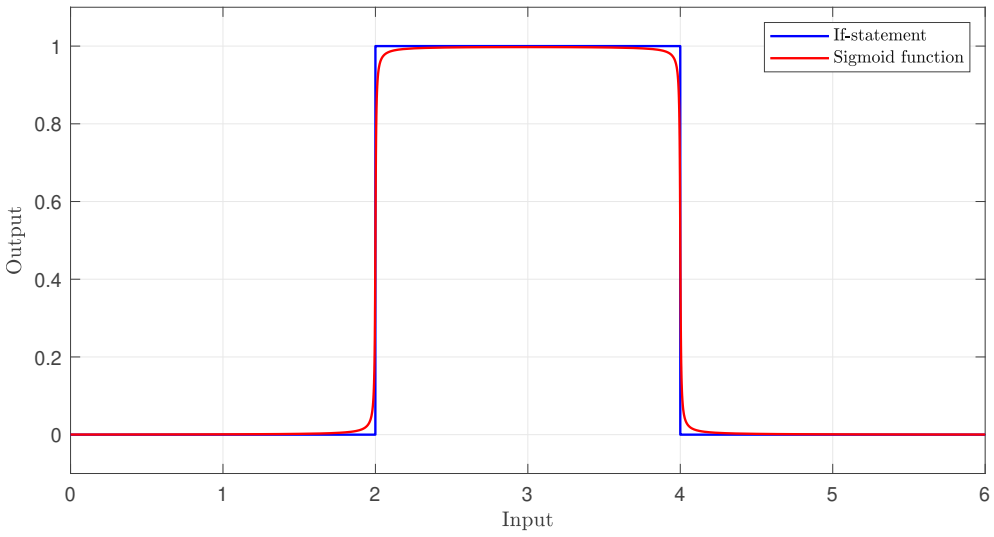

Figure 4.1: Approximation of If-statement with sigmoid activation function (Eq. 4.22). Example with $x_{sw,1} = 2$, $x_{sw,2} = 4$ and $\varepsilon = 250$.

Applying this adaptions to the model, the system matrix $\boldsymbol{A}$ and the input matrix $\boldsymbol{B}$ of the linearized model (Eqs. 4.14-4.15) can be obtained by

$$\boldsymbol{A} = \begin{bmatrix} \left.\frac{\partial(\boldsymbol{\mathcal{A}}_k^{-1}\mathfrak{b}_k)}{\partial \boldsymbol{x}_k}\right|_{\boldsymbol{x}_{k-1},\boldsymbol{u}_{k-1}} \\ \boldsymbol{I} \qquad\quad \boldsymbol{0} \end{bmatrix} \qquad (n_x \times n_x) \tag{4.23}$$

$$\boldsymbol{B} = \begin{bmatrix} \left.\frac{\partial(\boldsymbol{\mathcal{A}}_k^{-1}\mathfrak{b}_k)}{\partial \boldsymbol{u}_k}\right|_{\boldsymbol{x}_{k-1},\boldsymbol{u}_{k-1}} \\ \boldsymbol{0} \end{bmatrix} \qquad (n_x \times n_u). \tag{4.24}$$

In Eq. 4.23, the dimension of $\left.\frac{\partial(\boldsymbol{\mathcal{A}}_k^{-1}\mathfrak{b}_k)}{\partial \boldsymbol{x}_k}\right|_{\boldsymbol{x}_{k-1},\boldsymbol{u}_{k-1}}$ is $(n_\chi \times n_x)$, $\boldsymbol{I}$ is of dimension $(2n_\chi \times 2n_\chi)$ and remaining zero matrix is of proper size. In Eq. 4.23, the dimension of $\left.\frac{\partial(\boldsymbol{\mathcal{A}}_k^{-1}\mathfrak{b}_k)}{\partial \boldsymbol{u}_k}\right|_{\boldsymbol{x}_{k-1},\boldsymbol{u}_{k-1}}$ is $(n_\chi \times n_u)$ with the remaining zero matrix having suitable dimension.

4.3 Model reduction

To obtain the reduced-order Jacobians of the system that are used within the observer algorithm instead of the full-order matrices, model order reduction techniques are used. In [30] various model reduction methods are presented and discussed. For linear and linearized models, so-called *balanced truncation* is a common reduction approach. Balanced truncation reduces the order of the system by transforming the linear system to a modal formulation and then neglecting modes with small Hankel singular values, i.e. only modes associated with dominant behavior are considered and all others eliminated [31]. This procedure additionally avoids the computation of corrections for all states in each node of the high-order system and therefore leads to more efficient state estimation because only few dominant modes are considered in the estimation. Balanced truncation has also been applied to state estimation problems using extended Kalman filters, e.g., in [32] for a latent heat thermal energy storage and in [22] for an isothermal PEMFC model, and will therefore be applied in this work.

For applying balanced realization, however, the linearized model (Eqs. 4.14-4.15) has to be scaled to obtain a normalized state vector $\boldsymbol{x}_n$ where the states are within the same order of magnitude. This has to be done to compute the Gramians that are needed to obtain the transformation matrix that transforms the state space system to its balanced realization.

$$\boldsymbol{x} = \boldsymbol{X}_N \boldsymbol{x}_n \tag{4.25}$$
$$\boldsymbol{u} = \boldsymbol{U}_N \boldsymbol{u}_n \tag{4.26}$$
$$\boldsymbol{y} = \boldsymbol{Y}_N \boldsymbol{y}_n \tag{4.27}$$

With Eqs. 4.25-4.27 the normalized and linearized system becomes:

$$\Delta \boldsymbol{x}_{n,k} = \boldsymbol{X}_N^{-1} \boldsymbol{A} \boldsymbol{X}_N \Delta \boldsymbol{x}_{n,k-1} + \boldsymbol{X}_N^{-1} \boldsymbol{B} \boldsymbol{U}_N \Delta \boldsymbol{u}_{n,k-1} \tag{4.28}$$
$$\Delta \boldsymbol{y}_{n,k} = \boldsymbol{Y}_N^{-1} \boldsymbol{C} \boldsymbol{X}_N \Delta \boldsymbol{x}_{n,k}. \tag{4.29}$$

The balanced realization is executed by the MATLAB-command `balreal`. To use this command, the normalized linear system has to be rearranged so it describes the absolute state and not the increment from the linearization point. $\boldsymbol{l}_{n,k}$ in Eq. 4.30 considers the (normalized) offset from the current linearization point. Using $\boldsymbol{A}_N = \boldsymbol{X}_N^{-1} \boldsymbol{A} \boldsymbol{X}_N$, $\boldsymbol{B}_N = \boldsymbol{X}_N^{-1} \boldsymbol{B} \boldsymbol{U}_N$ and $\boldsymbol{C}_N = \boldsymbol{Y}_N^{-1} \boldsymbol{C} \boldsymbol{X}_N$, Eqs. 4.28-4.29 can be simplified to

$$\boldsymbol{x}_{n,k} = \boldsymbol{A}_N \boldsymbol{x}_{n,k-1} + \boldsymbol{B}_N \boldsymbol{u}_{n,k-1} + \boldsymbol{l}_{n,k-1} \tag{4.30}$$
$$\text{with} \quad \boldsymbol{l}_{n,k-1} = \boldsymbol{X}_N^{-1} [\boldsymbol{f}(\boldsymbol{x}_{k-1}, \boldsymbol{u}_{k-1}) - \boldsymbol{A} \boldsymbol{x}_{k-1} - \boldsymbol{B} \boldsymbol{u}_{k-1}] \tag{4.31}$$
$$\boldsymbol{y}_{n,k} = \boldsymbol{C}_N \boldsymbol{x}_{n,k}. \tag{4.32}$$

The input term and the off-equilibrium term in Eq. 4.30 can be lumped together to form

$$\boldsymbol{x}_{n,k} = \boldsymbol{A}_N \boldsymbol{x}_{n,k-1} + [\boldsymbol{B}_N \quad \boldsymbol{l}_{n,k-1}] \begin{bmatrix} \boldsymbol{u}_{n,k-1} \\ 1 \end{bmatrix} \tag{4.33}$$
$$\text{and further} \quad \boldsymbol{x}_{n,k} = \boldsymbol{A}_N \boldsymbol{x}_{n,k-1} + \bar{\boldsymbol{B}}_N \bar{\boldsymbol{u}}_{n,k-1} \quad . \tag{4.34}$$

Handing over $\boldsymbol{A}_N$, $\bar{\boldsymbol{B}}_N$ and $\boldsymbol{C}_N$ to `balreal`, the square transformation matrix $\tilde{\boldsymbol{T}}$ and its inverse $\tilde{\boldsymbol{T}}_i$ are obtained as output (Eq. 4.35).

$$\tilde{\boldsymbol{x}} = \tilde{\boldsymbol{T}} \boldsymbol{x}_n \Longleftrightarrow \boldsymbol{x}_n = \tilde{\boldsymbol{T}}_i \tilde{\boldsymbol{x}} \tag{4.35}$$

The transformation matrix $\tilde{\boldsymbol{T}}$ $(n_x \times n_x)$ can be split up into two parts. One part maps the normalized states to the reduced-order modal states that are preserved ($\tilde{\boldsymbol{T}}_r$) and the other part maps the normalized states to the eliminated modal states ($\tilde{\boldsymbol{T}}_e$). The inverse transformation matrix $\tilde{\boldsymbol{T}}_i$ is partitioned accordingly. The transformed state vector $\tilde{\boldsymbol{x}}$ can also be partitioned in the same way ($\tilde{\boldsymbol{x}}_r$, $\tilde{\boldsymbol{x}}_e$), resulting in

$$\begin{bmatrix} \tilde{\boldsymbol{x}}_r \\ \tilde{\boldsymbol{x}}_e \end{bmatrix} = \begin{bmatrix} \tilde{\boldsymbol{T}}_r \\ \tilde{\boldsymbol{T}}_e \end{bmatrix} \boldsymbol{x}_n \quad \Longleftrightarrow \quad \boldsymbol{x}_n = \begin{bmatrix} \tilde{\boldsymbol{T}}_{i,r} & \tilde{\boldsymbol{T}}_{i,e} \end{bmatrix} \begin{bmatrix} \tilde{\boldsymbol{x}}_r \\ \tilde{\boldsymbol{x}}_e \end{bmatrix}. \tag{4.36}$$

The order of the reduced system n_r, i.e. the number of most dominant modes that are preserved from the truncation can be chosen arbitrarily. The size of the transformation matrix $\tilde{\boldsymbol{T}}_r$ is $n_r \times n_x$, the size of its inverse $\tilde{\boldsymbol{T}}_{i,r}$ is $n_x \times n_r$. The truncation is executed by simply eliminating all other states ($\tilde{\boldsymbol{x}}_e$). The transformation from the full-order (normalized) model to the reduced-order model is shown in Eq. 4.37.

$$\tilde{\boldsymbol{x}}_r = \tilde{\boldsymbol{T}}_r \boldsymbol{x}_n \quad \Longleftrightarrow \quad \boldsymbol{x}_n = \tilde{\boldsymbol{T}}_{i,r} \tilde{\boldsymbol{x}}_r \tag{4.37}$$

Applying this transformation to Eqs. 4.34 & 4.32, the reduced model of order n_r is obtained:

$$\tilde{\boldsymbol{x}}_{r,k} = \tilde{\boldsymbol{T}}_r \boldsymbol{A}_N \tilde{\boldsymbol{T}}_{i,r} \tilde{\boldsymbol{x}}_{r,k-1} + \tilde{\boldsymbol{T}}_r \bar{\boldsymbol{B}}_N \bar{\boldsymbol{u}}_{n,k-1} \tag{4.38}$$

$$\boldsymbol{y}_{n,k} = \boldsymbol{C}_N \tilde{\boldsymbol{T}}_{i,r} \tilde{\boldsymbol{x}}_{r,k} \quad . \tag{4.39}$$

Using $\tilde{\boldsymbol{A}}_r = \tilde{\boldsymbol{T}}_r \boldsymbol{A}_N \tilde{\boldsymbol{T}}_{i,r}$, $\tilde{\boldsymbol{B}}_r = \tilde{\boldsymbol{T}}_r \bar{\boldsymbol{B}}_N$ and $\tilde{\boldsymbol{C}}_r = \boldsymbol{C}_N \tilde{\boldsymbol{T}}_{i,r}$, the reduced order model becomes:

$$\tilde{\boldsymbol{x}}_{r,k} = \tilde{\boldsymbol{A}}_r \tilde{\boldsymbol{x}}_{r,k-1} + \tilde{\boldsymbol{B}}_r \bar{\boldsymbol{u}}_{n,k-1} \tag{4.40}$$

$$\boldsymbol{y}_{n,k} = \tilde{\boldsymbol{C}}_r \tilde{\boldsymbol{x}}_{r,k} \quad . \tag{4.41}$$

The reduced-order system matrix $\tilde{\boldsymbol{A}}_r$ $(n_r \times n_r)$ and the reduced-order output matrix $\tilde{\boldsymbol{C}}_r$ $(n_y \times n_r)$ are used in the update step of the extended Kalman filter algorithm. The chosen reduced order of the system is presented in 5.1 where the simulation setup is discussed.

Knowing the back-transformation matrix from reduced-order modal space to normalized state space $\tilde{\boldsymbol{T}}_{i,r}$ and the state normalization matrix $\boldsymbol{X}_N$, the transformation matrix $\boldsymbol{\mathcal{T}}$ from Eq. 4.11 that maps the reduced-order modal space to the full-order state space becomes

$$\boldsymbol{\mathcal{T}} = \boldsymbol{X}_N \tilde{\boldsymbol{T}}_{i,r} \quad . \tag{4.42}$$

4.4 Sensor placement

The placement of the sensors whose measurements are used in the state observer is crucial for its performance. Due to financial cost and limited space requirements, using numerous sensors is not recommended. Instead, efficient observers only use a few significant measurements. In PEMFC systems, the resulting cell potential (voltage) is one of the most decisive quantities which is also accessible relatively easily and therefore often used as a measurement variable, e.g., in [26] and [22]. To increase observability more measurement quantities can be taken into account. For a PEM fuel cell, available measurements are most likely quantities at the inlet or outlet of the gas channels. The inlet and outlet pressure on both anode and cathode side of the cell are potentially suitable. However, as mentioned in 3.3.4, the model is assumed to be pressure-driven in this work and therefore, the inlet and outlet pressures on both sides are considered as boundary conditions (system inputs) and thereby do not depict usable measurements (see Eq. 3.12). The bipolar plate temperatures and channel inlet temperatures are input variables as well and therefore also not suitable as measurement variables. The channel outlet temperature, however, is no input and thereby can be added as an additional measurement. For the sake of easier assembly on a real system, only the temperature at the cathode channel outlet will be measured but not the temperature at the anode channel outlet. How observability can be determined and if observability is guaranteed using measurements of the voltage and the cathode channel outlet temperature is investigated in the following chapter. The placement of the voltage and temperature sensor on the 2D plane is shown schematically in Fig. 4.2.

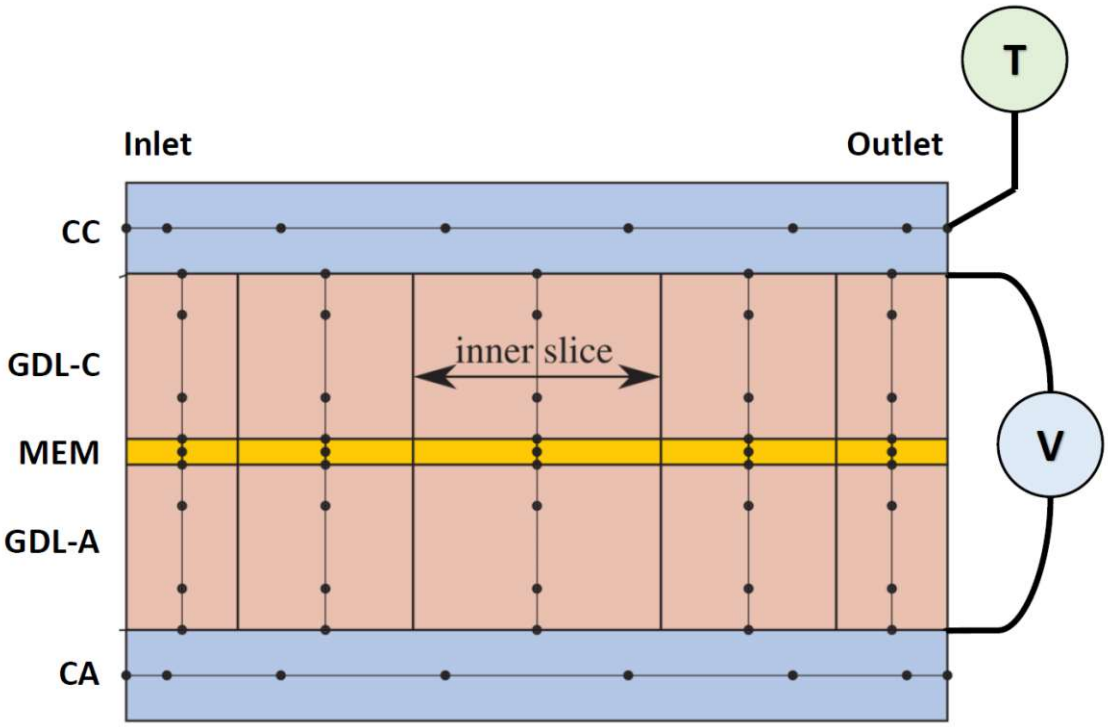

Figure 4.2: Sensor placement on quasi-2D plane from [14]

4.5 Observability analysis

In order to develop a state observer, it has to be guaranteed that it is possible to reconstruct the system states from the system outputs. If it is possible to determine every system state solely from the (measured) system outputs in the range of all possible state and input values in finite time, the system is said to be *completely state observable*. Observability is a crucial property of a system whose states are to be estimated. Methods to analyze the observability of linear systems were investigated by R.E. Kalman [33, 34]. Eq. 4.43 shows the so-called observability matrix which can be computed for a linear or linearized system. The Kalman observability criterion for linear systems (as Eqs. 4.14 & 4.15) is shown in Eq. 4.44.

$$\boldsymbol{Q}_{ob} = \begin{bmatrix} \boldsymbol{C} \\ \boldsymbol{C}\boldsymbol{A} \\ \boldsymbol{C}\boldsymbol{A}^2 \\ \vdots \\ \boldsymbol{C}\boldsymbol{A}^{n-1} \end{bmatrix} \tag{4.43}$$

$$\operatorname{rank}(\boldsymbol{Q}_{ob}) = n_x \tag{4.44}$$

Observability criteria for nonlinear systems have been introduced in [35] and have been applied to PEMFC observation problems using Lie derivatives [23]. However, the observability of a nonlinear system strongly depends on the current working point, and computing the observability as a function of the state vector analytically can be a complex task, especially for a high-order model as it is used in this work. Therefore, the observability of the used model is determined for the successively linearized system presented in 4.2 and 4.3.

4.5.1 Full-order model

The spatial discretization of the non-isothermal quasi-2D model as presented in 3.3 that is used within the observer is shown in Table 4.1. The selected spatial discretization leads to a total number of $n_\chi = 381$ states for one time step (Eq. 3.10) and therefore the order of the linearized system in 4.14 that includes the two previous time steps becomes $n_x = 1143$.

cathode channel nodes	N_{cc}	8
anode channel nodes	N_{ca}	8
cathode GDL nodes	$N_{gdl,c}$	4
anode GDL nodes	$N_{gdl,a}$	4
number of slices	N_{sl}	4
membrane nodes	N_{mem}	5

Table 4.1: Spatial discretization of the model used in the observer

Computing the observability matrix $\boldsymbol{Q}_{ob}$ in Eq. 4.43 for the full-order model requires the computation of high powers of the high-order system matrix $\boldsymbol{A}$ of Eq. 4.14. Because this computation is most likely to create numerical difficulties, it is not advisable to investigate the observability of the full-order system using the Kalman criterion. Another approach to investigate the observability of the full-order system is to investigate the contribution of each state to the most dominant modes. This can be done by checking the rows of the transformation matrix $\tilde{\boldsymbol{T}}_r$ that maps the normalized states to the modes of the system. Each element of row j therefore contains the factors of the states and how strongly they contribute to mode j. Since observability is only investigated for the current time step, it is sufficient to check the first n_χ columns of $\tilde{\boldsymbol{T}}_r$.

Figure 4.3 shows which entries of the first 6 rows of $\tilde{\boldsymbol{T}}_r$ are greater than a certain threshold, that is 10^{-4} in this case, and therefore contribute significantly to the corresponding mode. The entries representing temperature are marked by red dots whereas other states are marked by a blue dot. The contribution of temperature is therefore significantly lower in the second mode than in the others. The abscissa shows the number of the state corresponding to the state vector of the current time step (Eq. 3.9). It is visible that the modes point in the direction of most states with a lack of contribution of the gas channel states, especially in the anode gas channel. This can be explained by the fact that pressures, temperatures, and mass fractions at the channel inlets and pressures at the channel outlets are inputs to the system (Eq. 3.12). Therefore, there is no need to reconstruct these states with the observer since they serve as inputs and are known by definition. Additionally, not all states have to contribute to the modes because of the strong coupling between neighboring states. Considering these properties, reconstructing the states from the modes is feasible and as seen in Chapter 5 and 6 works well.

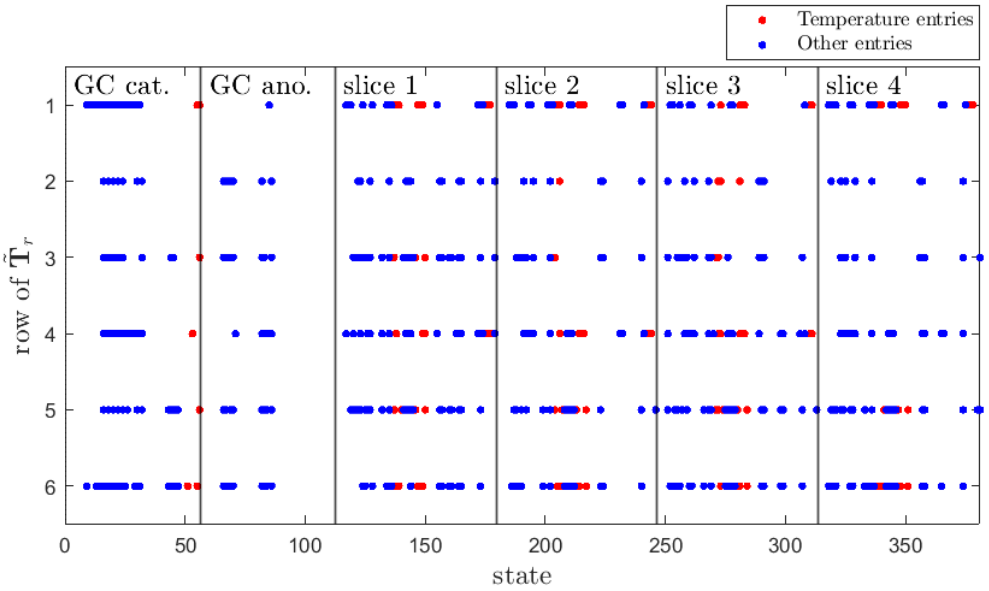

Figure 4.3: Entries of reduction matrix $\tilde{\boldsymbol{T}}_r$. The rows correspond to the respective most dominant mode (the first row corresponds to the first most dominant mode, etc.). The dots denote the significant non-zero entries and indicate in which direction in the state-space each mode points. Red dots indicate entries corresponding to temperature states, blue dots indicate entries corresponding to other states.

4.5.2 Reduced-order model

Since the observer uses the reduced-order model for the EKF update step, the observability is also investigated in the modal space of reduced order. In comparison to the full-order model, however, the Kalman observability criterion (Eq. 4.44) can be applied due to the lower number of modal states. To compute the observability matrix $\boldsymbol{Q}_{ob}$, the reduced order Jacobians $\tilde{\boldsymbol{A}}_r$ and $\tilde{\boldsymbol{C}}_r$ from Eqs. 4.40 & 4.41 are used. To obtain these reduced order matrices, the nonlinear model (Eq. 3.14) is successively linearized around the current trajectory as explained in 4.2.

average current density	i_{avg}	2000	$\frac{A}{m^2}$
cathode channel inlet pressure	p_{in}^{cc}	103500	Pa
anode channel inlet pressure	p_{in}^{ca}	103200	Pa
cathode channel outlet pressure	p_{out}^{cc}	101325	Pa
anode channel outlet pressure	p_{out}^{ca}	101325	Pa
cathode channel inlet oxygen mass fraction	$\xi_{O_2,in}^{cc}$	0.2092	
cathode channel inlet nitrogen mass fraction	$\xi_{N_2,in}^{cc}$	0.6889	
anode channel inlet hydrogen mass fraction	$\xi_{H_2,in}^{ca}$	0.4326	
anode channel inlet water vapor mass fraction	$\xi_{H_2O,in}^{ca}$	0.5674	
cathode channel inlet temperature	T_{in}^{cc}	343.15	K
anode channel inlet temperature	T_{in}^{ca}	343.15	K
cathode-side bipolar plate temperature	T_{bp}^{c}	343.15	K
anode-side bipolar plate temperature	T_{bp}^{a}	343.15	K

Table 4.2: Boundary conditions in representative operating point

Table 4.2 shows the numeric values of the input vector (Eq. 3.12) to the system in a representative working point. The observability analysis of the reduced-order modal system is explained for this operating point, however, the observability was investigated for several potential operating points.

In this thesis, the order of the reduced model $n_r << n_x$ is selected by only considering the first n_r modes whose normalized Hankel singular values cumulate to 0.97 minimum. This means that only those first n_r modes are preserved that together contain at least 97% of the system's energy. For the sensor placement discussed in the previous section (measurement of voltage and cathode channel outlet temperature), the reduced order of the system is thus $n_r = 6$. The observability criterion of Kalman (Eq. 4.44) is satisfied for models of reduced order linearized around the aforementioned operating point as long as $n_r < 47$ holds. Therefore, the reduced-order modal model of order

$n_r = 6$ is completely observable in the considered operating point. Since the linearized model is obtained successively during operation, the local observability is only valid for estimating the system modes in this operating point. However, the local observability of the reduced-order model at other potential operating points was also tested and satisfied the observability matrix rank criterion in all tested points as well.

The overall workflow of the successive linearization-based reduced-order observer algorithm is shown schematically in Fig. 4.4. It has to be pointed out that the presented algorithm using a full-order model for prediction and the reduced-order model preserving the dominant behavior for correction is applicable to every kind of high-order observation problem and is not limited to PEM fuel cell systems.

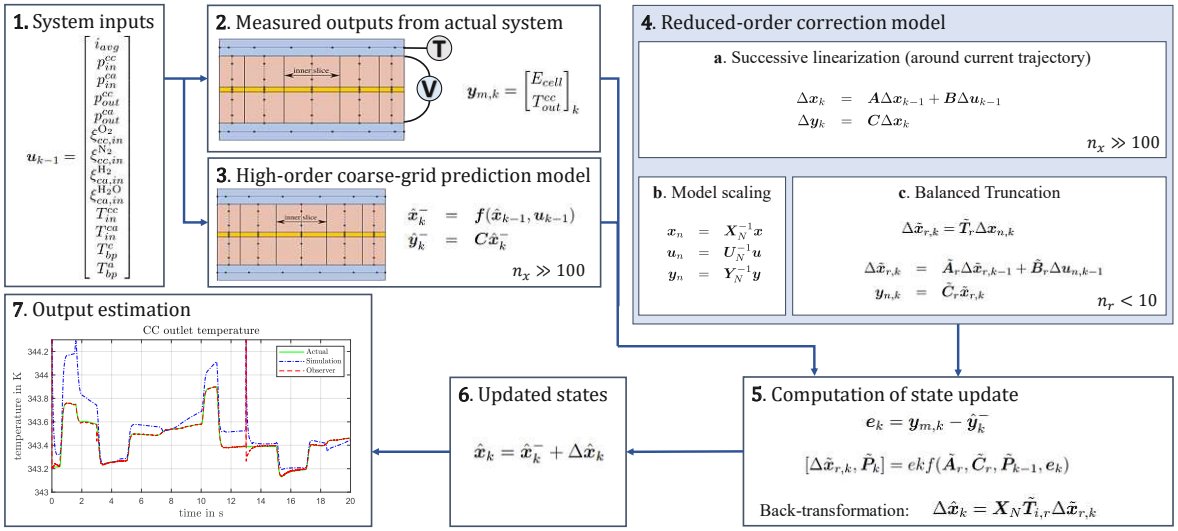

Figure 4.4: Observer workflow

Chapter 5

Results of state estimation

The performance of the state observer using an extended Kalman filter algorithm is presented in this chapter. The setup of the simulation and the validation of the observer performance are discussed. The results of the state estimation dealing with wrong initialization, measurement noise, and state disturbances after the estimation has converged are shown. The results are presented for the case with only the average current density as a single manipulable system input and for the case with the cathode channel inlet pressure as a second manipulable system input.

5.1 Simulation setup

In order to investigate the full performance of the state estimation, measurements of all states of an actual fuel cell system are needed. Since it is physically impossible to measure all internal states of a real PEMFC system and the resulting state distributions, a virtual reality model is generated using a spatially fine-discretized version of the quasi-2D PEMFC model. The fine-grid discretization is shown in Table 5.1.

cathode channel nodes	N_{cc}	20
anode channel nodes	N_{ca}	20
cathode GDL nodes	$N_{gdl,c}$	6
anode GDL nodes	$N_{gdl,a}$	6
number of slices	N_{sl}	8
membrane nodes	N_{mem}	5

Table 5.1: Spatial discretization of the virtual reality fine-grid model

This procedure additionally allows to get actual state distributions without corruption from measurement noise as it always occurs when using real measurements. The

measurement signals for the use in the observer (voltage and cathode channel outlet temperature) are created by overlapping the virtual true quantities with Gaussian, zero-mean white noise of appropriate standard deviation to investigate the observer performance for real, noisy measurements.

As described in 4.5.1, the state observer uses the coarse-grid discretization given in Table 4.1. The resulting mismatch between the observer model and the simulated reality depicts a plant-model mismatch as it would also occur in a real-life system. To show the advantage of using state estimation, a simulation run without an observer is done that uses the same coarse-grid model and the same initialization as the observer. Therefore, the observer performance is investigated by comparing three simulation runs:

- Fine-grid simulated reality giving the true system states that the observer shall estimate
- Coarse-grid simulation without an active observer to investigate the speed of convergence of the observer
- Observer using a coarse-grid model and measurements to estimate the states of the actual system

For the sake of better readability, these three simulations are henceforth referred to as *actual system*, *simulation*, and *observer*.

The initial state of an actual FC system is generally unknown. Therefore, the observer and the simulation start from a different initial state than the actual system. The actual initial state is given by the steady state that is reached when using the boundary conditions given in Table 4.2. The wrong initialization of the observer and the simulation is obtained by assuming the initial average current density is $i_{avg} = 1000 \frac{\mathrm{A}}{\mathrm{m}^2}$ and the temperature in the whole cell is $T = 353.15$ K. How these wrong initial assumptions affect all other initial states of the observer and the simulation can be seen in the graphs of the following sections.

To further test the performance of the observer, a disturbance of the temperature of the whole cell and the membrane water content is implemented after the states have converged from the initial state deviation. This is done by setting the whole cell temperature for the simulation and the observer to $T = 353.15$ K and the membrane water content to $\lambda = 2$ for each membrane node at a selected point in time. For all the simulation runs of the actual system, the simulation and the observer the same constant time step of $\Delta t = 6.25$ ms is used. The changing input signals showing

the excitation of the system are shown in the respective section of this chapter. All simulation experiments are set to be 20 s long.

In the following sections, the performance of the observer is investigated using the three discussed simulation runs *actual system*, *simulation* and *observer* and is satisfactory if the observer manages to estimate the true system states faster than the simulation without correction.

5.2 Results with single dynamic system input

The results for the simulation setup discussed before are presented in this section. As mentioned, the average current density is the only manipulable boundary condition of the system. The excitation signal that serves as dynamical system input is shown in Fig. 5.1. To visualize the results of the internal state distributions, snapshots at specific time steps are taken (0 s, 6 s, 10.5 s, 18.5 s) and visualized in the excitation signal as vertical magenta lines. The covariance matrices of the EKF algorithm that serve as tuning parameters are given below (size of $\tilde{\boldsymbol{P}}_0$ is $(n_r \times n_r)$). To investigate the observer performance when encountering disturbances, the wrong re-initialization of the states, as explained before, is implemented at $t = 13$ s.

$$\tilde{\boldsymbol{Q}} = 5 \cdot 10^{-7} \cdot \mathrm{diag}(20 \;\; 1 \;\; 1 \;\; 1 \;\; 1 \;\; 1) \tag{5.1}$$

$$\boldsymbol{R} = \mathrm{diag}(0.003^2 \;\; 0.001^2) \tag{5.2}$$

$$\tilde{\boldsymbol{P}}_0 = 5 \cdot \boldsymbol{I} \tag{5.3}$$

The obtained system outputs (cell potential E_{cell} and cathode channel outlet temperature T_{out}^{cc}) are shown in Fig. 5.2. The actual output signal, which is unknown to the observer, is displayed by a green line whereas the noisy measurement that is used by the observer is displayed in grey. For both outputs, it can be seen that the observer (red dashed line) is able to estimate the actual signal faster than the simulation without correction (blue dash-dot line) and estimate the true output value despite the measurement noise. It has to be pointed out that the actual states and distributions (green lines) are completely unknown for a real-life system. The estimations from the observer are solely computed from the measurements (grey lines) and the quasi-2D PEMFC model using the known inputs as boundary conditions. The power of the observer is visible especially within the first seconds after the wrong initialization ($t = 0$ s) and the wrong re-initialization ($t = 13$ s), where the simulation alone takes more time to detect the

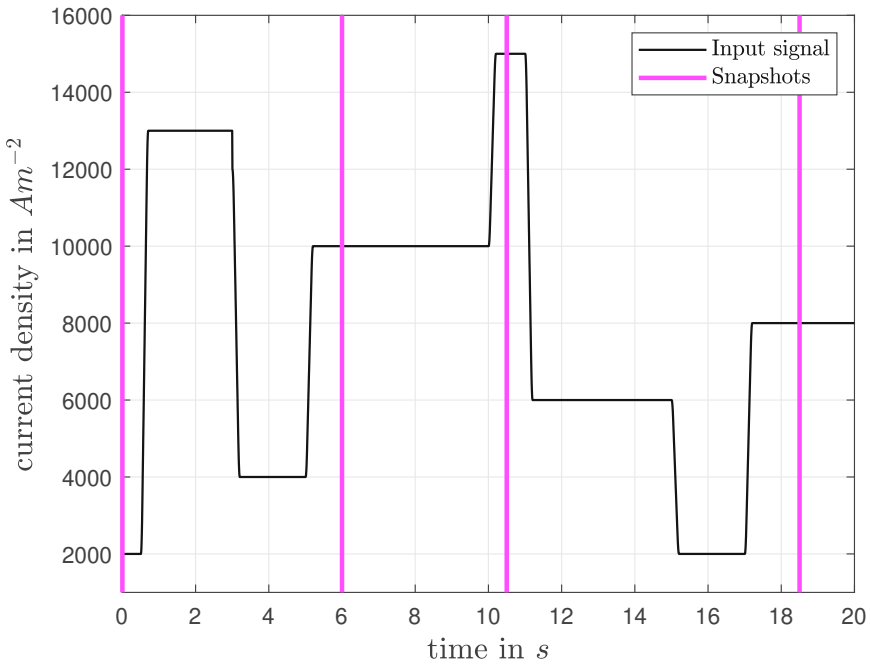

Figure 5.1: Input signal: average current density i_{avg}

actual value. The first few seconds after the initialization of the cathode channel outlet temperature signals are shown in Fig. 5.3b. Fig. 5.3a gives the following seconds after the wrong re-initialization at $t = 13$ s for the cell potential. In both cases, it is visible that the observer is aware of the deviation of the actual system from the measurements and corrects its estimation to match the actual outputs and states. The simulation without correction, however, converges ultimately because the system is asymptotically stable and therefore the initial difference will decay after some time.

As seen, the state observer is able to estimate the actual output values from noisy measurements. However, special interest lies in the estimation of internal state distributions where no measurements are available at all. In the following, the temperature distribution along the cell in both gas channels, both catalyst layers, and within the membrane is shown. Further the distribution of the membrane water content λ, the local current density i_{curr} and the species concentrations in both gas channels ξ_j ($j \in \{O_2,\ H_2,\ N_2,\ H_2O\}$) are compared for the actual system, the simulation and the observer at the snapshot time steps mentioned before.

Fig. 5.4 shows the temperature distribution along the gas channels. Each line of plots

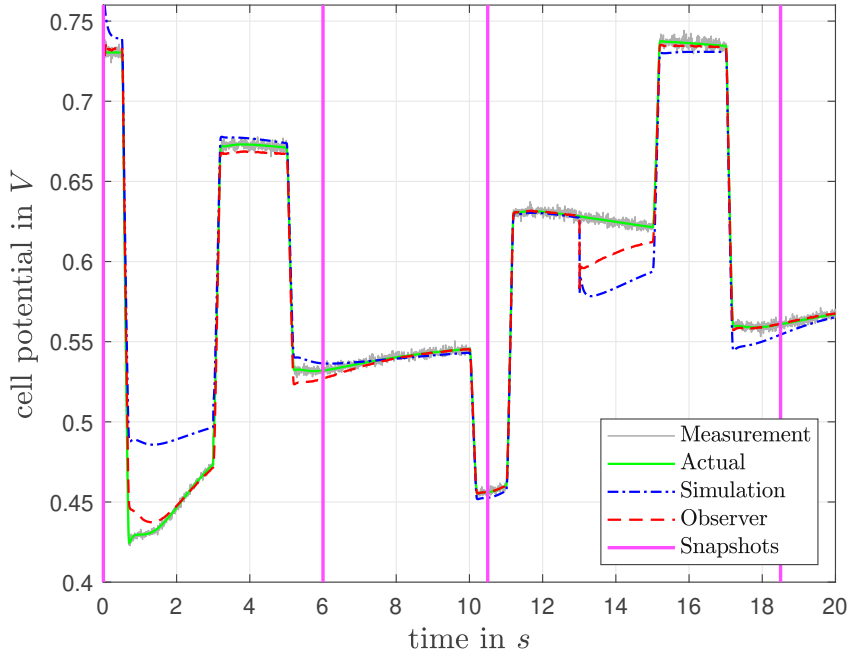

(a) cell potential E_{cell}

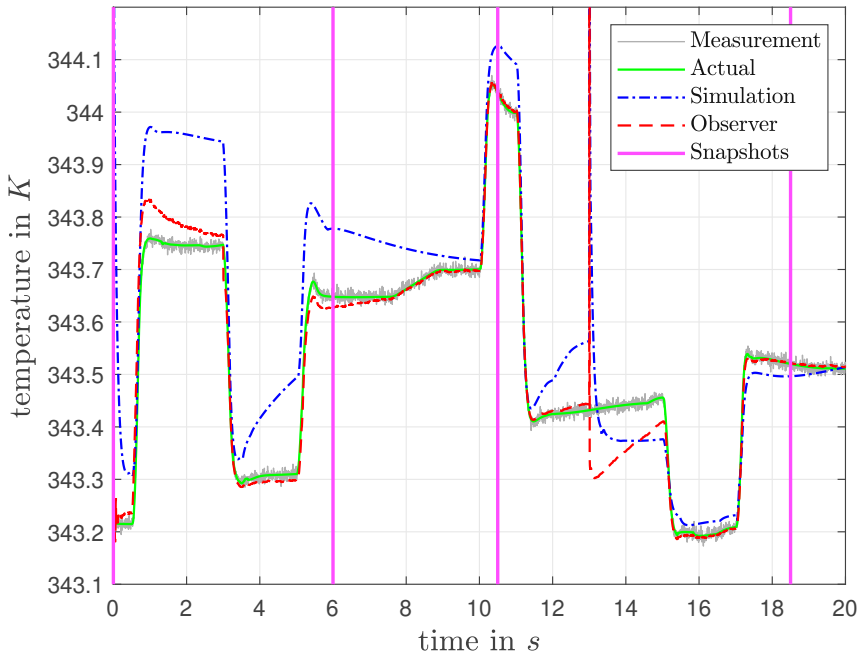

(b) cathode channel outlet temperature T_{out}^{cc}

Figure 5.2: Measured outputs

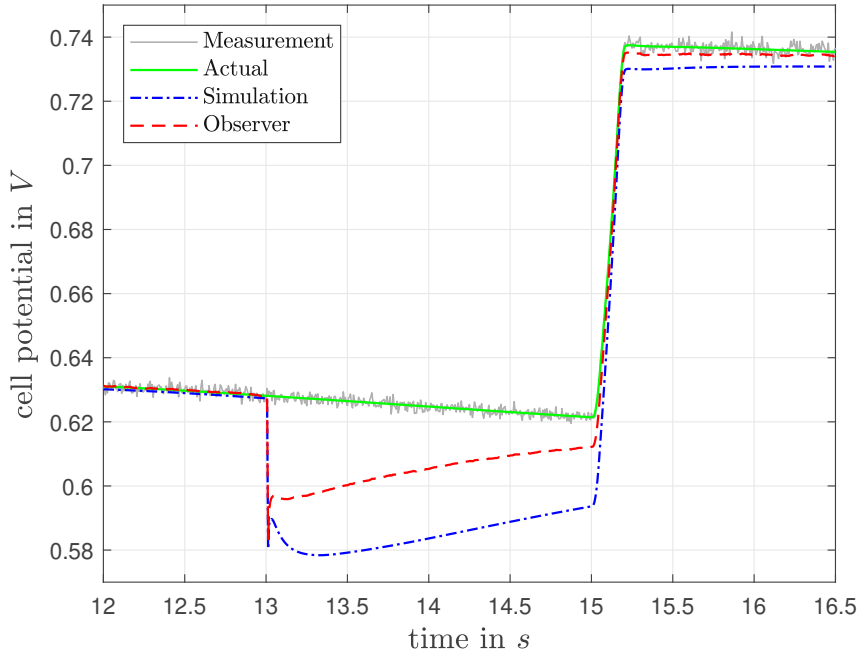

(a) cell potential E_{cell}

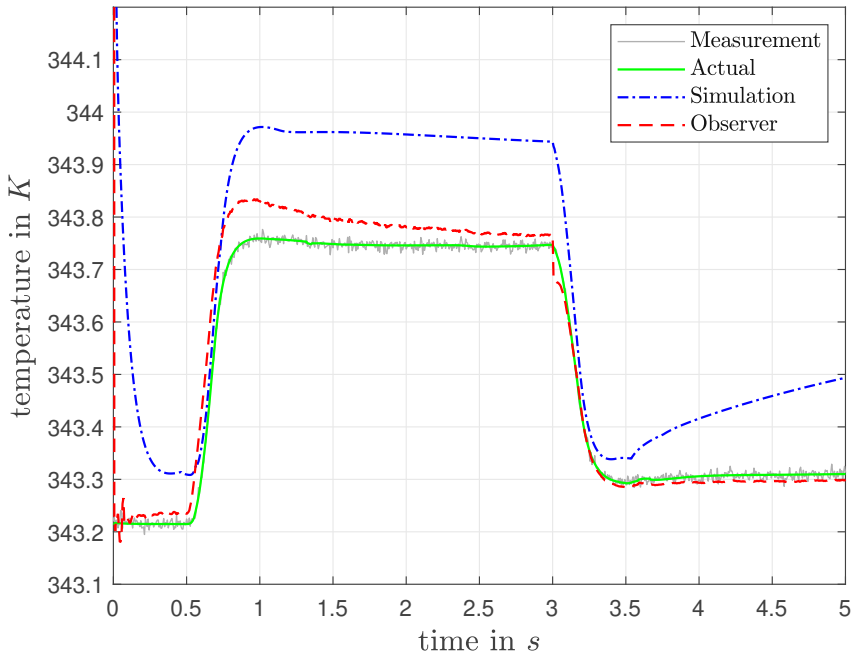

(b) cathode channel outlet temperature T_{out}^{cc}

Figure 5.3: Measured outputs (zoom)

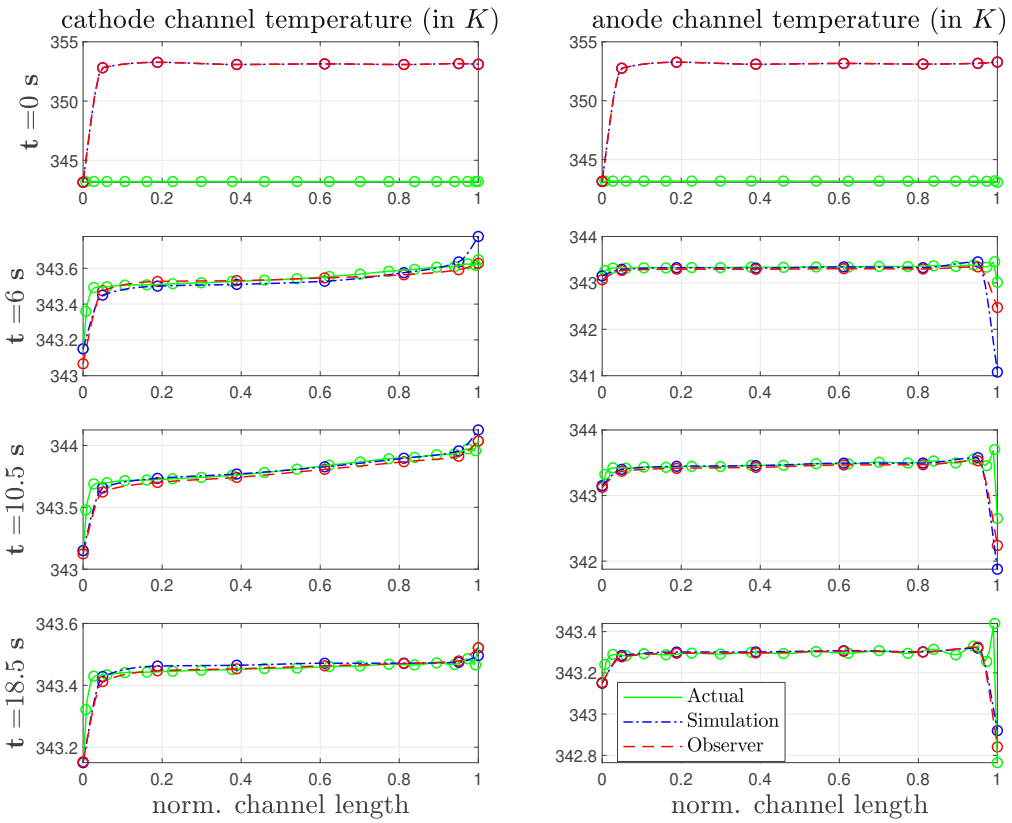

Figure 5.4: Temperature in gas channels

shows the distributions at the time step given on the left. At the abscissa, 0 denotes the inlet side, and 1 denotes the outlet side of the fuel cell. It is visible that the simulated and estimated channel temperatures are very close to the actual distribution. This is easily explained by the fact that the channel inlet temperatures as well as the bipolar plate temperature along the channels are set as constant boundary conditions to the system and therefore strongly limit the channel temperature deviations.

The temperature distribution in the membrane (middle node) and the catalyst layers (interface node between membrane and gas diffusion layer on each side of the cell), however, are of particular interest because the electrochemical reactions and the transport of protons and water take place there. In Fig. 5.5, the relatively high initial deviation decays within a few seconds, so that at $t = 6$ s the estimated temperature fields have converged toward the actual temperature distribution. After $t = 10.5$ s, also the simulation without observer has converged. At $t = 13$ s the re-initialization

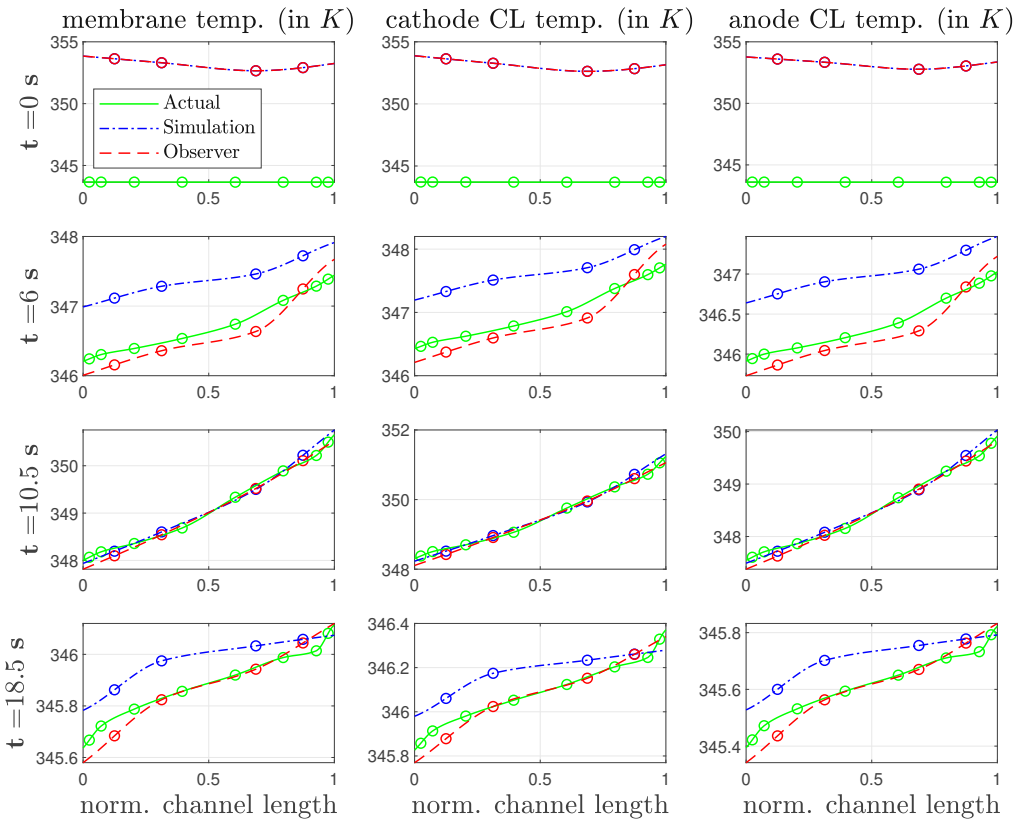

Figure 5.5: Temperature in membrane and catalyst layers

disturbs the states of simulation and observer. However, the observer is aware of the deviation due to the measurements, corrects the estimations, and converges faster back to the true temperature distribution than the simulation, as seen at $t = 18.5$ s. The absolute temperature difference between the true temperature field and the simulation without observer looks small at first sight. However, the temperature gradient from the membrane to the bipolar plates during operation is expected to be in a range of $\sim 5 - 10$ K. In relation to the expected temperature gradient, a difference of 1 K, as occurring at $t = 6$ s and $t = 18.5$ s, already means an error of $10 - 20$ % and is therefore considerable.

In Fig. 5.6, the distributions of the membrane water content at the middle node of the membrane and the local current density are shown. At $t = 0$ s, the wrong initialization can be seen. After 6 s of simulation time, the observer approximates the actual distributions well. As seen at $t = 18.5$ s, the wrongly re-initialized state distributions converge

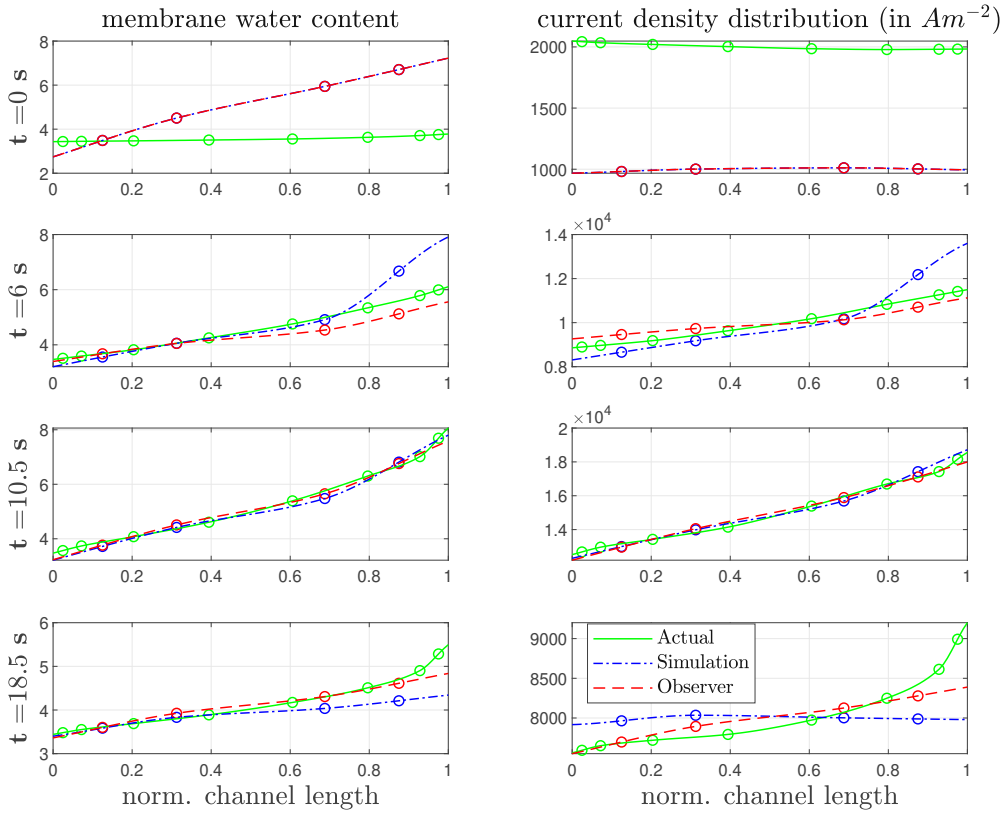

Figure 5.6: Membrane water content & current density distribution

toward the true state distributions faster for the observer than for the simulation alone. For both fields, membrane water content, and local current density, it can be seen that the deviation between simulation and actual distribution is bigger toward the outlet side of the fuel cell than on the inlet side. Although no liquid water is considered in the underlying model, the estimated membrane water content gives a measure of the humidification of the membrane. The observer being able to estimate the true membrane water content distribution is therefore able to monitor the membrane regarding drying or flooding.

The distributed concentrations of the cathode channel species O_2, N_2, and H_2O are shown in Fig. 5.7. The oxygen and water vapor distributions show that, apart from the initial state, only little differences between simulation, observer, and the actual system exist for the whole simulation time. Since air is used as cathode-side gas, nitrogen is the main component in the cathode channel. The estimated nitrogen distribution converges

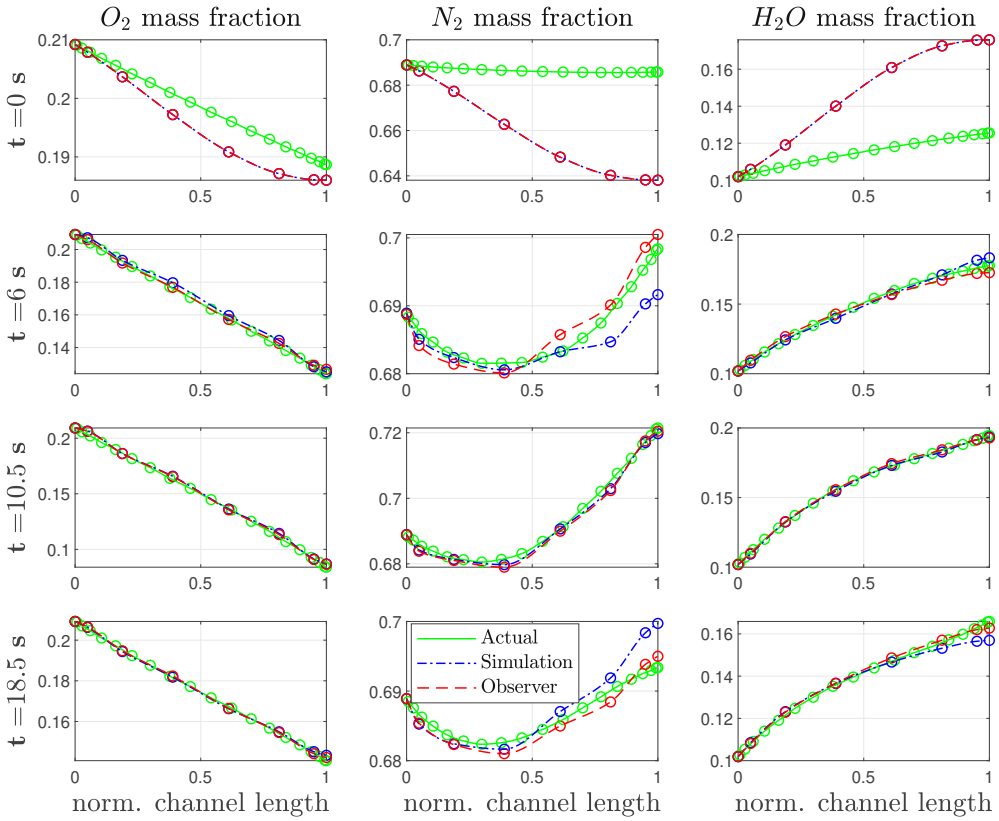

Figure 5.7: Cathode channel species concentrations

toward the actual distribution faster than the simulation without state estimation. After all simulations have converged, the disturbance at $t = 13$ s deviates the states. The observer updates the state estimation, so the N_2 concentration is approaching the true nitrogen concentration faster than the simulation without correction.

Fig. 5.8 displays the distributions of the anode channel species H_2, N_2, and H_2O. The observer is able to detect the true species distributions within a few seconds ($t = 6$ s). Also after the wrong re-initialization, the observer estimates the actual concentrations for each component faster than the simulation without a corrective algorithm. The nitrogen concentration on the anode side grows toward the channel outlet due to nitrogen crossover from the cathode to the anode side leading to smaller hydrogen concentrations at the channel outlet. The results show that the H_2 concentration is estimated well by the observer and therefore allows the detection of potential fuel starvation.

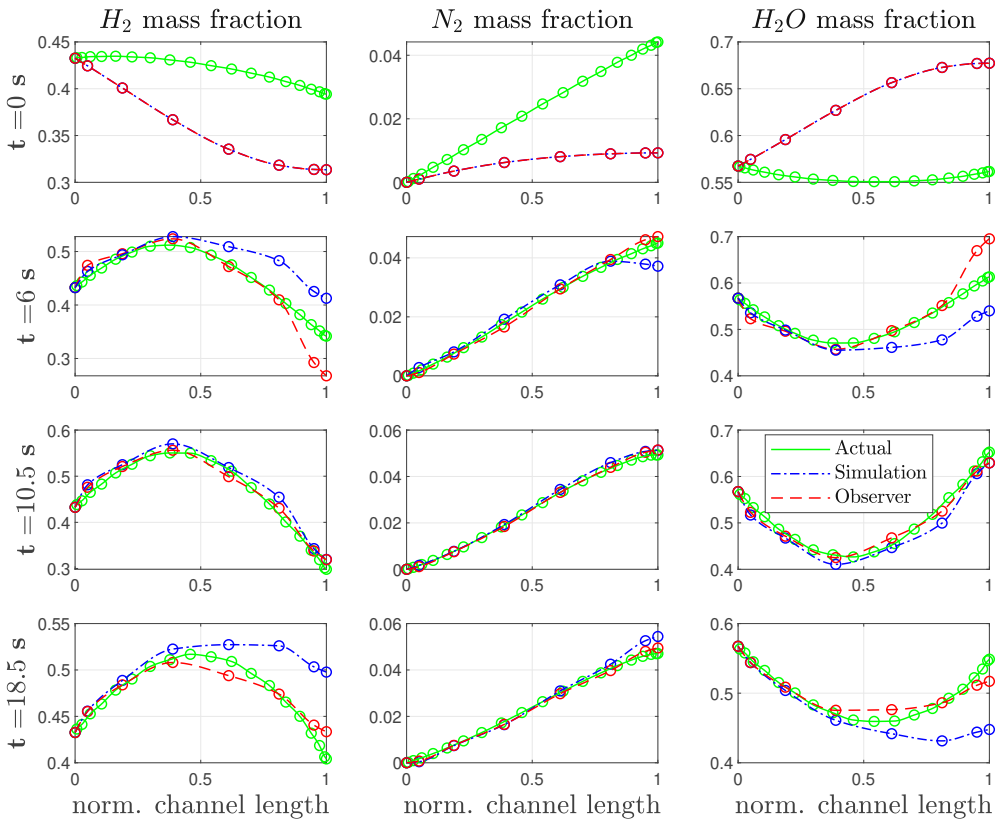

Figure 5.8: Anode channel species concentrations

5.3 Results with multiple dynamic system inputs

The observer works demonstrably well for the operation with one single manipulable boundary condition (average current density i_{avg}). The operation of a real-life fuel cell system, however, is generally dependent on multiple changeable boundary conditions. In the case of pressure-driven operation, as it is assumed in this work, the inlet pressure of the gas channels is a common manipulable system input. To investigate the performance of the observer for more realistic FC operations, the cathode channel inlet pressure p_{in}^{cc} is added as a second dynamic input to the system. The model reduction ($n_r = 6$), application of the EKF algorithm, and simulation setup are analogous to the case with only the average current density as excitation signal. Since the outputs, states, and order of the reduced model have not changed, the observability determined for the single-input system is still valid. Again, the wrong re-initialization of the observer and the simulation is implemented at $t = 13$ s with the same values as in the single-input case. The tuning matrices used within the extended Kalman filter for the multi-input case are stated below (size of $\tilde{\boldsymbol{P}}_0$ is $(n_r \times n_r)$).

$$\tilde{\boldsymbol{Q}} = 1.5 \cdot 10^{-9} \cdot \mathrm{diag}(30 \;\; 1 \;\; 1 \;\; 1 \;\; 1 \;\; 1) \tag{5.4}$$

$$\boldsymbol{R} = \mathrm{diag}(0.00029^2 \;\; 0.00004^2) \tag{5.5}$$

$$\tilde{\boldsymbol{P}}_0 = 2 \cdot \boldsymbol{I} \tag{5.6}$$

The input signals of average current density and cathode channel inlet pressure are shown in Fig. 5.9 where the magenta lines again mark the times of the snapshots used to visualize the internal state distributions ($t \in \{0\text{ s},\ 4\text{ s},\ 9\text{ s},\ 17\text{ s}\}$).

The output signals are shown in Fig. 5.10 where the noisy measurement that is handed over to the observer is depicted in grey and the true signal, which is unknown to the observer, is displayed in green. Fig. 5.10a shows the cell potential and how much faster the observer converges toward the true value than the simulation alone. This is visible at the beginning of the simulation experiment as well as after the re-initialization at $t = 13$ s. Fig. 5.11a shows the first 3.5 s of the simulation run where the decay of the wrong initialization can be seen in detail.

The cathode channel outlet temperature signals are depicted in Fig. 5.10b. While the observer is converging quickly, the simulation without correction is not able to converge at all during the simulation run due to the highly dynamic operation with two

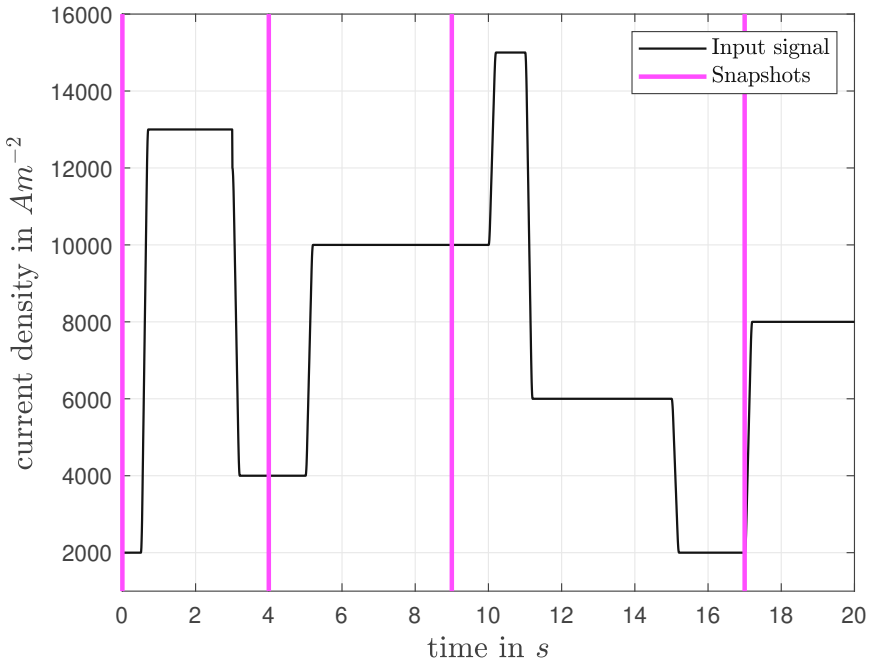

(a) average current density i_{avg}

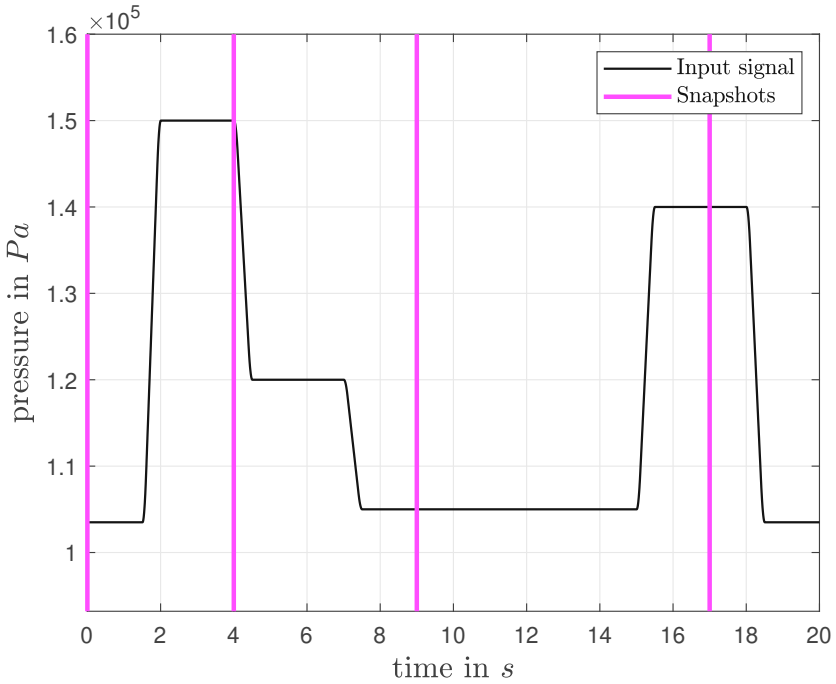

(b) cathode channel inlet pressure p_{in}^{cc}

Figure 5.9: Input signals to system for experiment with two dynamic inputs

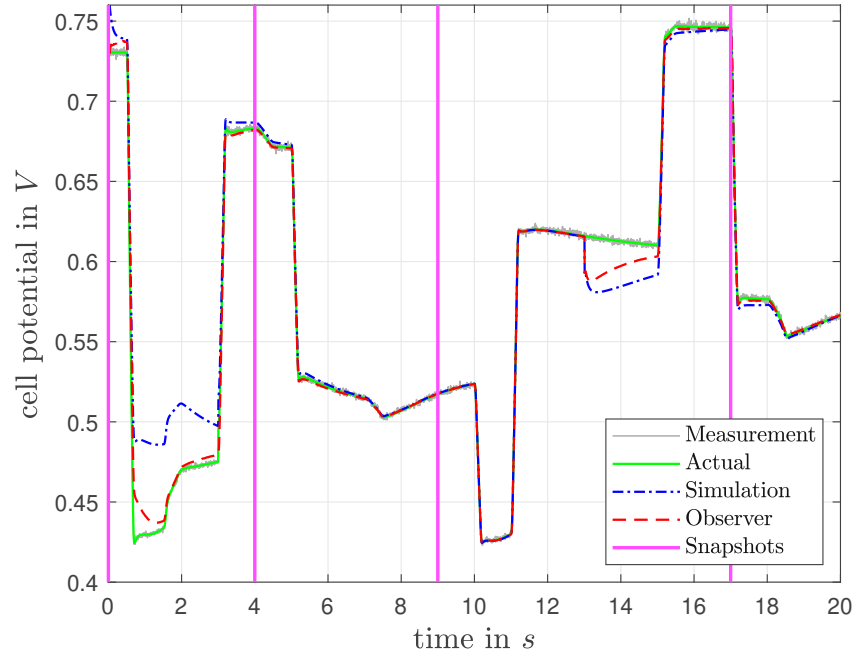

(a) cell potential E_{cell}

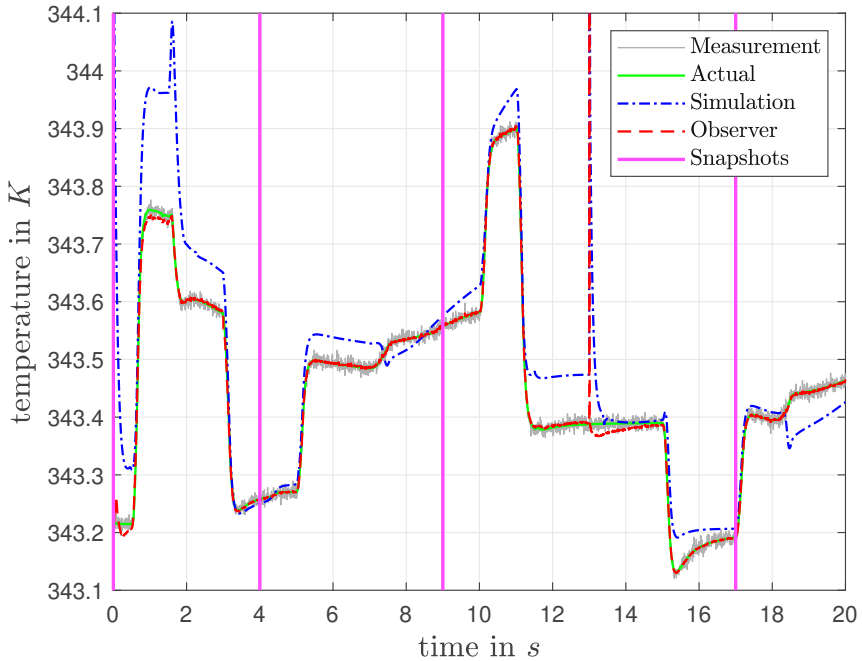

(b) cathode channel outlet temperature T_{out}^{cc}

Figure 5.10: Measured outputs for experiment with two dynamic inputs

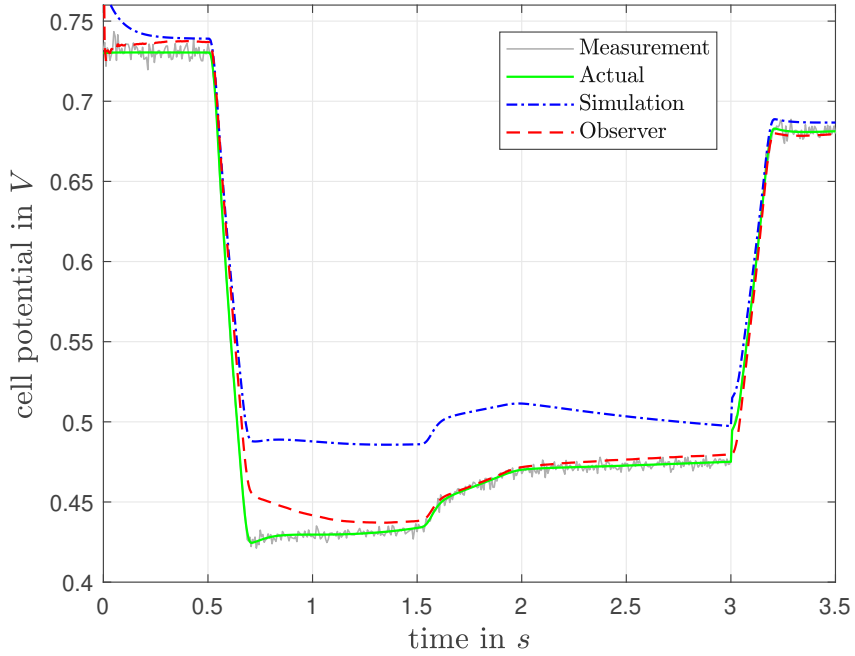

(a) cell potential E_{cell}

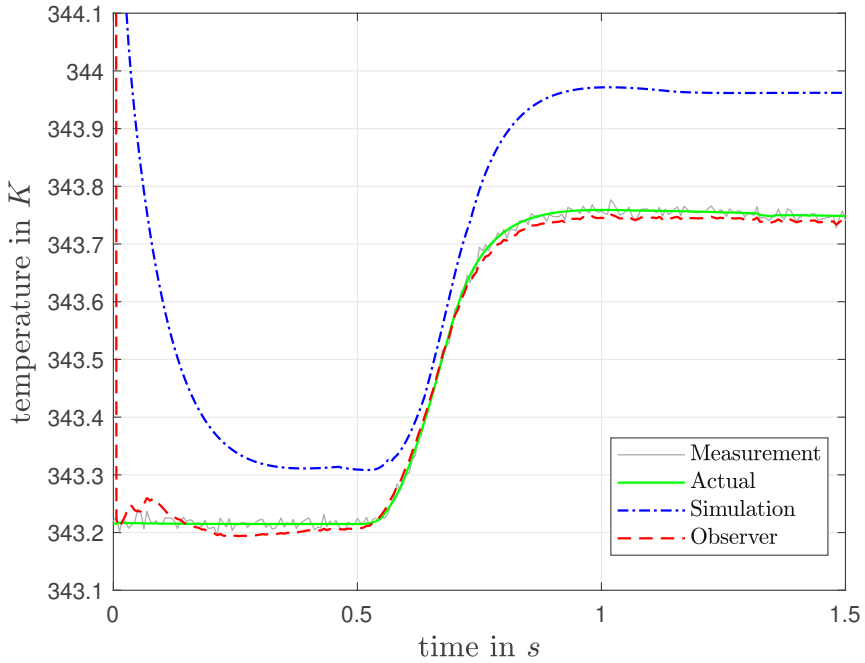

(b) cathode channel outlet temperature T_{out}^{cc}

Figure 5.11: Measured outputs for experiment with two dynamic inputs (zoom)

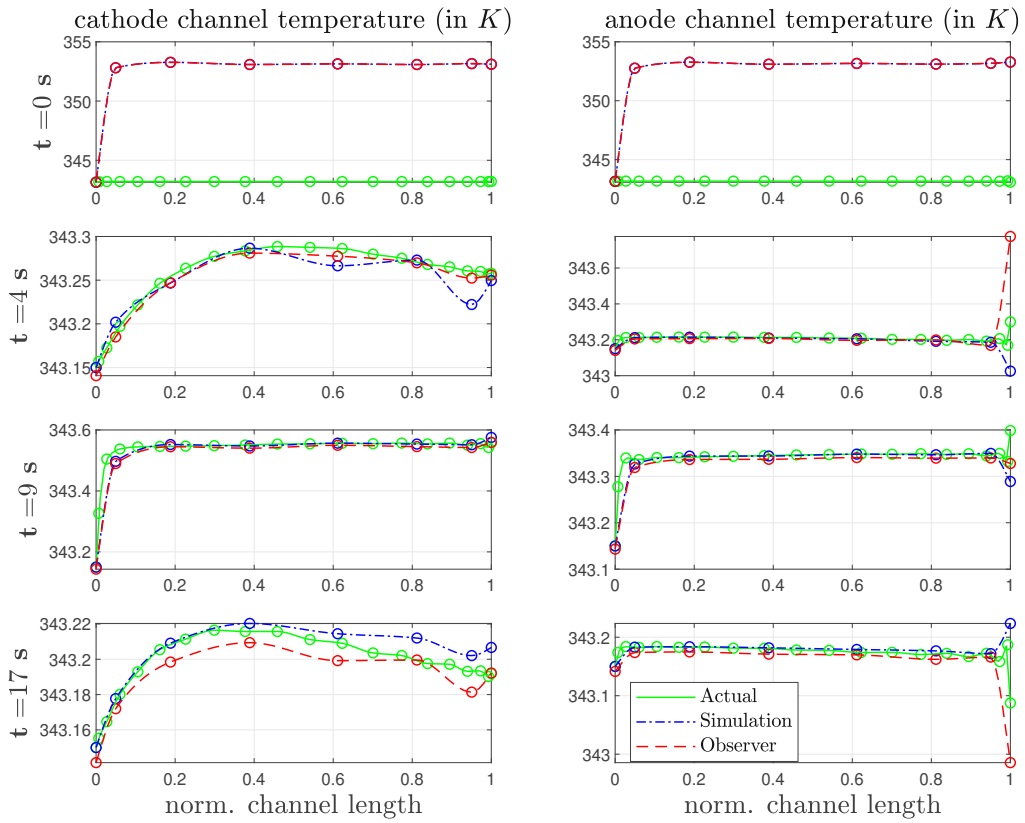

Figure 5.12: Temperature in gas channels for experiment with two dynamic inputs

manipulable input signals. The first 1.5 s that show the fast convergence of the cathode channel outlet temperature is visible in Fig. 5.11b.

The temperature distributions in the gas channels are displayed in Fig. 5.12. Again, the differences between simulation, observer, and actual distribution are very low because the channel inlet temperatures and the bipolar plate temperatures along the whole channels are constant boundary conditions and therefore strongly limit the effects of wrong initialization.

However, due to more temperature-sensitive materials, especially the polymer of the membrane, the temperature field within the membrane and catalyst layers (Fig. 5.13) is of higher interest anyway. The observer uses the measurements of the cell potential and the cathode channel outlet temperature to correct its estimated states and therefore

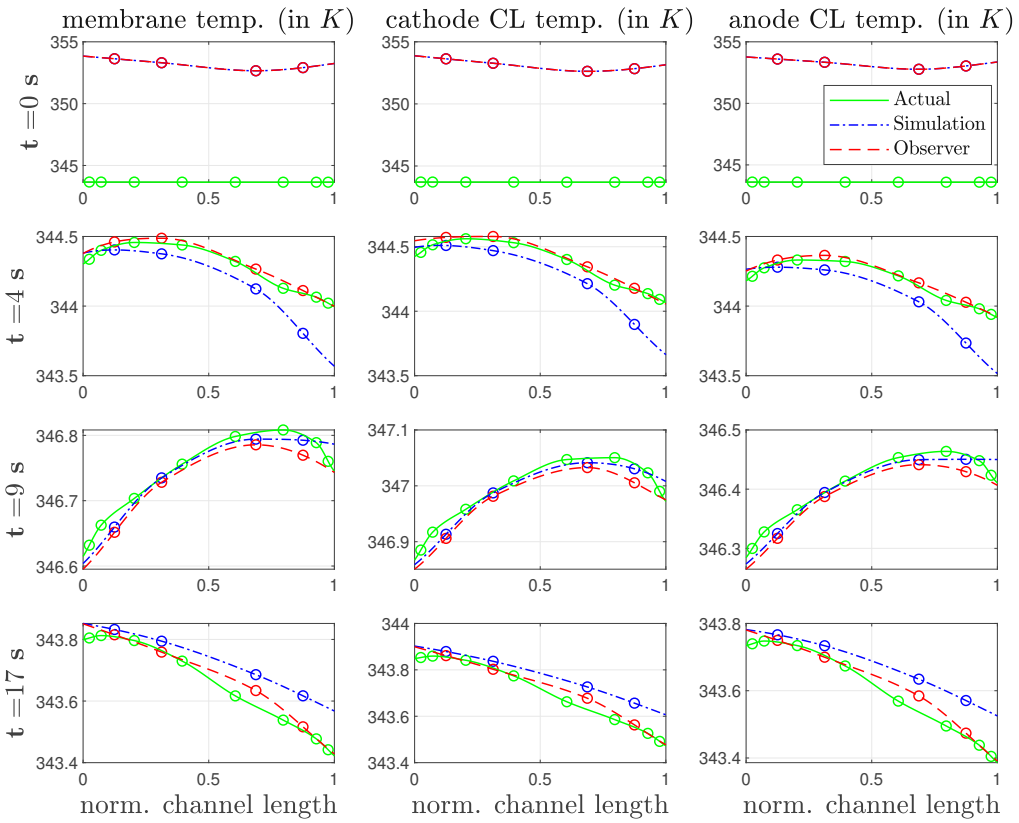

Figure 5.13: Temperature in membrane and catalyst layers for experiment with two dynamic inputs

reaches the true temperature field faster (after 4 s) than the simulation without observer (9 s). After the state disturbance at $t = 13$ s, the observer reacts to the deviation and again converges faster to the true temperature than the simulation ($t = 17$ s) and therefore is proven to allow more precise temperature estimation also for multiple changing input signals.

The distributions of the membrane water content (middle node) and the local current density are given in Fig. 5.14. Especially the initial deviation for the current density is relatively high but the observer is able to estimate the actual current density distribution after a few seconds (4 s). The simulated local current density distribution converges after several more seconds (9 s) but is not as strongly affected by the wrong re-initialization at $t = 13$ s as other states and therefore the disturbance decays fast for both, simulation and observer ($t = 17$ s). The membrane water content, of particular

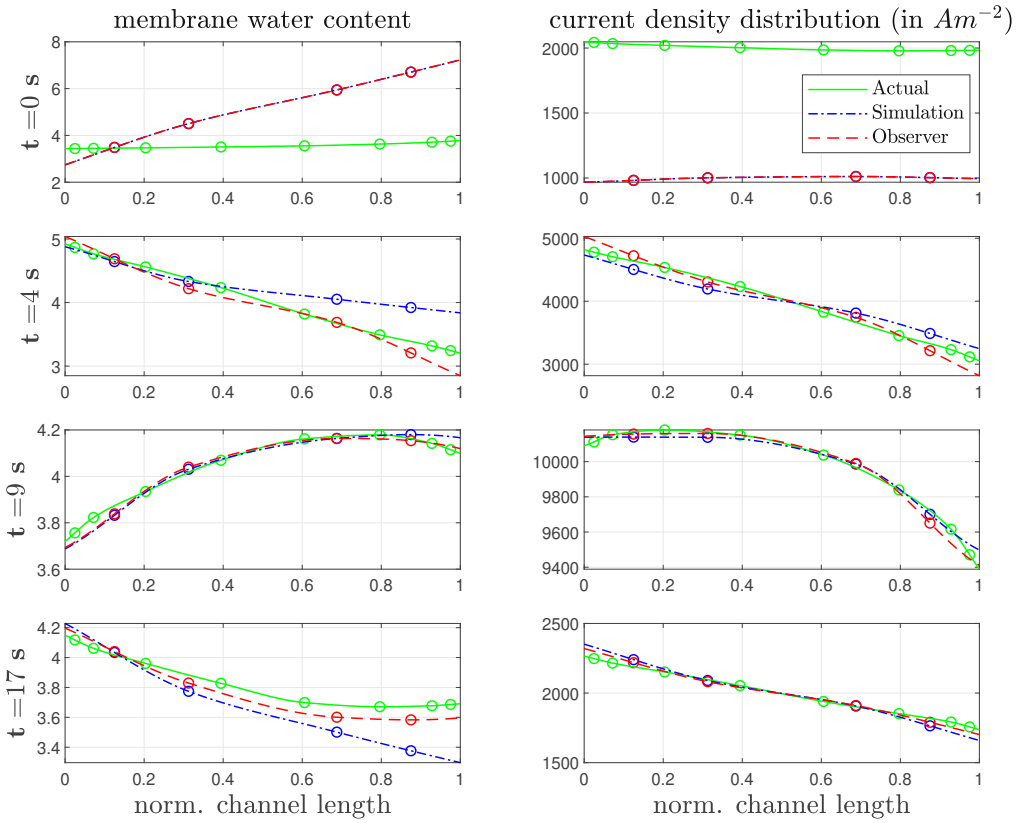

Figure 5.14: Membrane water content & current density distribution for experiment with two dynamic inputs

interest due to the detection of membrane drying or flooding, is estimated visibly faster by the observer than by the simulation. The disturbance after both coarse-grid simulations have converged also shows at $t = 17$ s that the true membrane water content is reached in less time than the simulation without correction. The simulation at this time estimates the water content at the outlet side too low, creating an error from ~ 10 % to the true water content.

The species concentrations of the cathode channel reactants are displayed in Fig. 5.15. The relative initial divergence is highest for the water vapor concentration. The state observer manages to drive all estimated concentrations toward the true states within a few seconds. Although the simulation is converging to the actual distributions in the following seconds, the disturbance again shows the observer's performance. Four seconds after the disturbance ($t = 17$ s), the observer is close to the true cathode

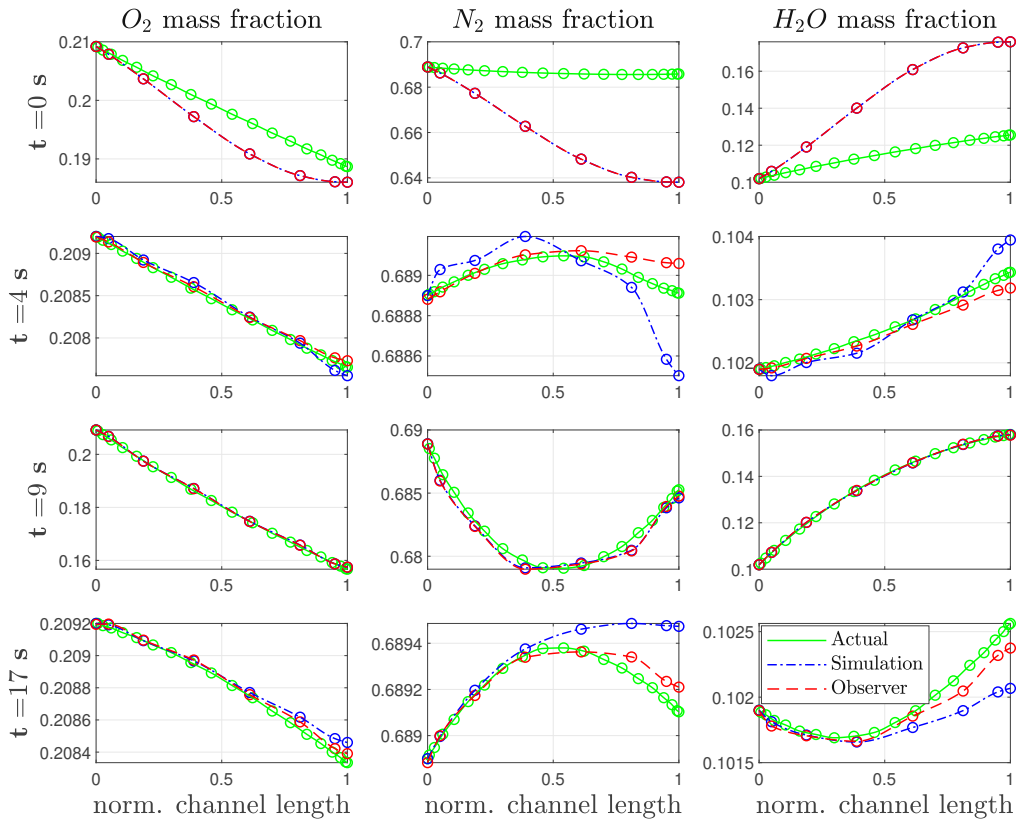

Figure 5.15: Cathode channel species concentrations for experiment with two dynamic inputs

channel species concentrations whereas the simulation takes longer to go toward the actual distributions.

Fig. 5.16 shows the concentrations of anode species. As ever, the inlet composition of the gas (at anode and cathode side) is a constant boundary condition and is therefore equal for all three simulation runs. At $t = 4\ s$, the observer is already close to the actual species distribution whereas the simulation shows relative errors of more than 20 % to the true values at the anode channel outlet. Eventually, the simulated species concentrations converge as seen at $t = 9$ s. After the re-initialization at $t = 13$ s, the observer is again able to push the system toward the true states faster than the uncorrected simulation.

The results show that the observer estimates the true state distributions fast and pre-

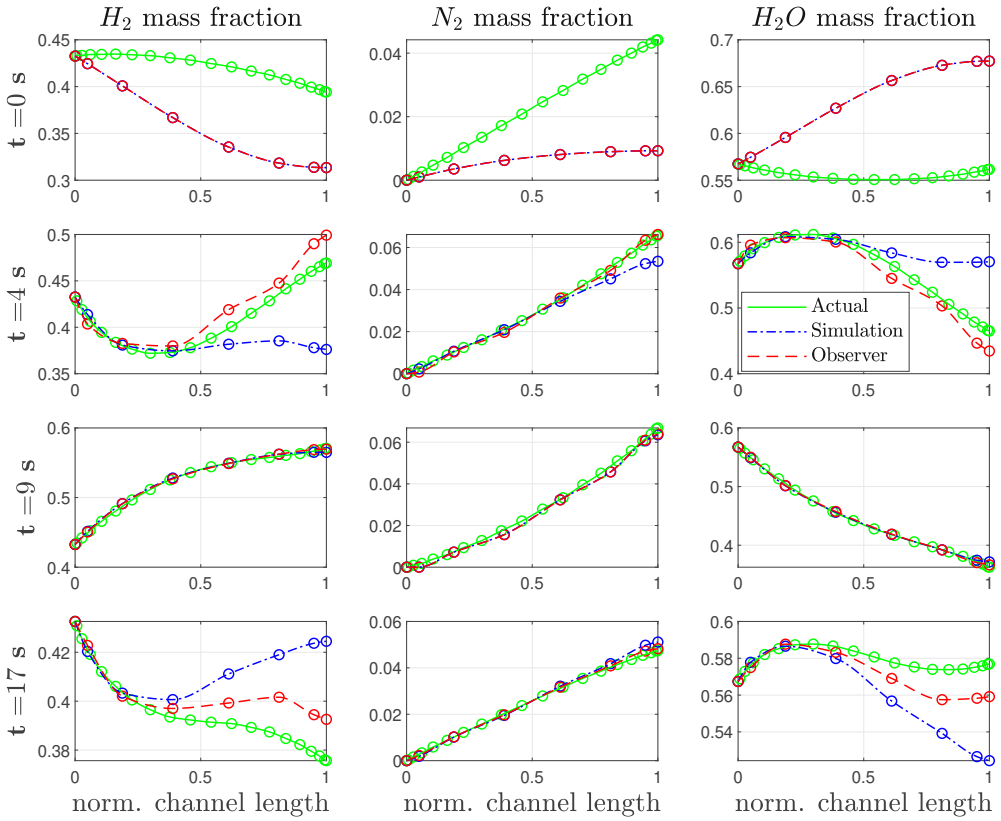

Figure 5.16: Anode channel species concentrations for experiment with two dynamic inputs

cisely. Some fields, e.g., the temperatures in both gas channels are strongly affected by constant boundary conditions and therefore allow fast convergence of the simulation as well. However, in real-life operation, a fuel cell system mostly operates with even more manipulable boundary conditions. It can be seen that the observer detects all actual state distributions as well as the true output signals from the noisy measurements. Once again it is stated that the actual states and distributions (green lines) are unknown for a real-life fuel cell. The comparison to the simulation (blue dash-dot line) shows the advantage of using an observer, that is fast convergence due to the incorporation of measurements to the estimation of states.

Chapter 6

Simultaneous state and parameter estimation

It has been shown that the observer is able to estimate the true states of the system from a wrongly initialized state since the true initial state is generally unknown for a real-life system. However, in addition to the initial state of an actual system, true parameters that cannot be measured might be unknown for a real system as well. The EKF algorithm is capable of being extended to simultaneously estimate unknown system parameters parallel to the state estimation. A method to include an estimation of parameters to the EKF algorithm by augmenting the estimated state vector is presented in [36]. In [37], the estimation of degradation parameters of a PEMFC system is shown using an extended Kalman filter. Following these approaches and the one described in [32], the observer presented in the previous sections is extended for estimating chosen parameters simultaneously to the state distributions. In [14], fitting parameters from Eqs. 3.4-3.6 used to adjust the quasi-2D model to a specific fuel cell are given. While most of those parameters are physical values that are hard to determine, two are dimensionless parameters solely used for fitting the model to an actual cell. Therefore, the parameters to be estimated are selected to be these two fitting parameters f_1 and f_2 of the membrane ionic conductivity (see Eq. 3.6).

6.1 Methodology for simultaneous state and parameter estimation

To estimate parameters and states simultaneously, the state estimation methodology from Chapter 4 has to be extended. At first, the nonlinear state space model (Eq. 3.14) is rewritten so it depends also on the vector containing the parameters to be estimated $\boldsymbol{\theta}$ $(n_\theta \times 1)$.

$$\boldsymbol{x}_k = \boldsymbol{f}(\boldsymbol{x}_{k-1}, \boldsymbol{u}_{k-1}, \boldsymbol{\theta}_{k-1}) \tag{6.1}$$

The system parameters to be estimated can be considered as unknown system inputs. To obtain the matrices needed for the EKF algorithm, Eq. 6.1 again is successively linearized around the current trajectory. Since the true fitting parameters f_1 and f_2 of the actual system are generally unknown for a real fuel cell, the parameters used in the initial state are initial guesses. In this case, the actual parameter values are known due to the simulated reality that is used as actual system. The actual parameters as well as the wrong initial parameter set used for observer and simulation are shown below.

$$\boldsymbol{\theta}_{act} = \begin{bmatrix} f_{1,act} \\ f_{2,act} \end{bmatrix} = \begin{bmatrix} 1.0 \\ 0.8 \end{bmatrix} \tag{6.2}$$

$$\boldsymbol{\theta}_{sim} = \begin{bmatrix} f_{1,sim} \\ f_{2,sim} \end{bmatrix} = \begin{bmatrix} 1.2 \\ 0.6 \end{bmatrix} \tag{6.3}$$

$$\boldsymbol{\theta}_{obs}^{init} = \begin{bmatrix} f_{1,obs}^{init} \\ f_{2,obs}^{init} \end{bmatrix} = \begin{bmatrix} 1.2 \\ 0.6 \end{bmatrix} \tag{6.4}$$

Linearizing the system in Eq. 6.1 with the parameters to be estimated as unknown inputs according to 4.2 yields

$$\Delta\boldsymbol{x}_k = \boldsymbol{A}\Delta\boldsymbol{x}_{k-1} + \boldsymbol{B}\begin{bmatrix} \Delta\boldsymbol{u}_{k-1} \\ \Delta\boldsymbol{\theta}_{k-1} \end{bmatrix}. \tag{6.5}$$

The new $(n_x \times (n_u + n_\theta))$ Jacobian matrix $\boldsymbol{B}$ is partitioned so the first n_u columns correspond to the inputs $\boldsymbol{u}$ and the last n_θ columns correspond to the parameters $\boldsymbol{\theta}$. Additionally including the linearization offset term at the current trajectory (as in Eq. 4.31) gives a reformulated state space model:

$$\boldsymbol{x}_k = \boldsymbol{A}\boldsymbol{x}_{k-1} + [\boldsymbol{B}_u \quad \boldsymbol{B}_\theta \quad \boldsymbol{l}_{k-1}] \begin{bmatrix} \boldsymbol{u}_{k-1} \\ \boldsymbol{\theta}_{k-1} \\ 1 \end{bmatrix}. \tag{6.6}$$

Taking care of the off-equilibrium term $\boldsymbol{l}_{k-1}$ the same way as in Eq. 4.34 and applying the system normalization as presented in 4.2, the linearized system in dependence of the unknown parameters becomes

$$\boldsymbol{x}_{n,k} = \boldsymbol{A}_N \boldsymbol{x}_{n,k-1} + \bar{\boldsymbol{B}}_{u,N} \bar{\boldsymbol{u}}_{n,k-1} + \boldsymbol{B}_{\theta,N} \boldsymbol{\theta}_{k-1} \tag{6.7}$$

$$\boldsymbol{y}_{n,k} = \boldsymbol{C}_N \boldsymbol{x}_{n,k} \quad . \tag{6.8}$$

Applying the balanced truncation transformation to the modal space (Eq. 4.37), the system can be rewritten in reduced order:

$$\tilde{\boldsymbol{x}}_{r,k} = \tilde{\boldsymbol{A}}_r \tilde{\boldsymbol{x}}_{r,k-1} + \tilde{\boldsymbol{B}}_{u,r} \bar{\boldsymbol{u}}_{n,k-1} + \tilde{\boldsymbol{B}}_{\theta,r} \boldsymbol{\theta}_{k-1} \tag{6.9}$$

$$\boldsymbol{y}_{n,k} = \tilde{\boldsymbol{C}}_r \tilde{\boldsymbol{x}}_{r,k} \quad . \tag{6.10}$$

If the reduced-order state vector $\tilde{\boldsymbol{x}}_r$ is extended by the parameter vector $\boldsymbol{\theta}$, the linearized and reduced system can be rearranged as

$$\begin{bmatrix} \tilde{\boldsymbol{x}}_r \\ \boldsymbol{\theta} \end{bmatrix}_k = \begin{bmatrix} \tilde{\boldsymbol{A}}_r & \tilde{\boldsymbol{B}}_{\theta,r} \\ \boldsymbol{0} & \boldsymbol{I} \end{bmatrix} \begin{bmatrix} \tilde{\boldsymbol{x}}_r \\ \boldsymbol{\theta} \end{bmatrix}_{k-1} + \begin{bmatrix} \tilde{\boldsymbol{B}}_{u,r} \\ \boldsymbol{0} \end{bmatrix} \bar{\boldsymbol{u}}_{n,k-1} \tag{6.11}$$

$$\boldsymbol{y}_{n,k} = \begin{bmatrix} \tilde{\boldsymbol{C}}_r & \boldsymbol{0} \end{bmatrix} \begin{bmatrix} \tilde{\boldsymbol{x}}_r \\ \boldsymbol{\theta} \end{bmatrix}_k \quad . \tag{6.12}$$

The extended system matrix from Eq. 6.11 and the extended output matrix from Eq. 6.12

$$\boldsymbol{A}_{r,\theta} = \begin{bmatrix} \tilde{\boldsymbol{A}}_r & \tilde{\boldsymbol{B}}_{\theta,r} \\ \boldsymbol{0} & \boldsymbol{I} \end{bmatrix} \tag{6.13}$$

$$\boldsymbol{C}_{r,\theta} = \begin{bmatrix} \tilde{\boldsymbol{C}}_r & \boldsymbol{0} \end{bmatrix} \tag{6.14}$$

can be used within the update step of the extended Kalman filter algorithm to estimate state distributions and unknown parameters simultaneously. This extended reduced-order system is observable if not only the most dominant modes are observable, but also the fitting parameters f_1 and f_2. The system's observability is investigated with the Kalman observability criterion (Eq. 4.44) in the same way as in Section 4.5 and guarantees observability for the used dimension of the reduced-order system n_r. The observability of the states is again analyzed by investigating the entries of the transformation matrix $\tilde{\boldsymbol{T}}_r$ and leads to the same conclusions as in 4.5.1. As for the states, the EKF algorithm uses the updated parameters in the next time step for predicting states and parameters. The dimensions of the error covariance matrix $\tilde{\boldsymbol{P}}$ and the process noise covariance matrix $\tilde{\boldsymbol{Q}}$ are adapted to match the augmented $((n_r + n_\theta) \times 1)$ state vector. The state back-transformation from reduced-order modal space to full-order state space is performed in the same way as before (Eq. 4.11).

6.2 Results of simultaneous state and parameter estimation

As in Chapter 5, the performance of the simultaneous state and parameter estimation is determined by comparing the EKF results to a simulation without corrective action and the results of a simulated reality using a fine-grid spatial discretization (see Table 4.1 and Table 5.1). The system is set to be pressure-driven and current-driven with all boundary conditions being held constant except the average current density i_{avg} and the cathode channel inlet pressure p_{cc}^{in} which serve as manipulable input signals. The constant values of the remaining boundary conditions can be seen in Table 4.2. The initial state of simulation and observer and the state disturbance after the states have converged are equal to the settings in 5.3. The initial parameter set for simulation and observer is shown in Eqs. 6.3 & 6.4.

The implemented EKF matrices for the simultaneous estimation of states and parameters are given below. It has to be pointed out that the dimensions of the below-stated EKF-matrices $\tilde{\boldsymbol{Q}}$ and $\tilde{\boldsymbol{P}}_0$ are adapted to match the augmented state vector shown in Eqs. 6.11 & 6.12 and are therefore $((n_r + n_\theta) \times (n_r + n_\theta))$, each. The input signals of the average current density i_{avg} and p_{in}^{cc} are given in Fig. 6.1. The snapshot times are set to be $t \in \{0\text{ s},\ 7.5\text{ s},\ 10.5\text{ s},\ 18\text{ s}\}$ and are marked by vertical magenta lines.

$$\tilde{\boldsymbol{Q}} = 7 \cdot 10^{-5} \cdot \mathrm{diag}(50 \;\; 1 \;\; 1 \;\; 1 \;\; 1 \;\; 1 \;\; 9.3 \;\; 1.3) \tag{6.15}$$

$$\boldsymbol{R} = \mathrm{diag}(0.024^2 \;\; 0.0047^2) \tag{6.16}$$

$$\tilde{\boldsymbol{P}}_0 = 2 \cdot \boldsymbol{I} \tag{6.17}$$

The output signals are displayed in Fig. 6.2. The impact of the wrong initialization of the parameters is easily visible in both output signals but especially in the cell potential signal (Fig. 6.2a) since the membrane ionic conductivity fitting parameters (f_1 & f_2) are affecting the membrane conductivity σ directly (Eq. 3.6) and therefore also the cell potential E_{cell} (Eq. 3.4). The simulation without correction is not able to adapt its wrongly initialized parameters and therefore cannot converge to the actual cell potential at all. The observer, however, is aware of the error between its prediction and the measurement of the actual fuel cell and therefore corrects the states and the parameters accordingly, leading to fast convergence to the true value for both outputs. The wrong re-initialization at $t = 13$ s is also handled well as shown in detail in Fig. 6.3.

The results of the parameter estimation are displayed in Fig. 6.4. The initially wrong parameters are estimated by the observer based on the computed residual between measurement and prediction and converge toward the actual parameter values within approximately 7 s. The state disturbance implemented after 13 s also leads to a deviation of the converged parameters but as visible, the estimated parameters are pushed back to the true parameters fast by the EKF. The implemented parameter estimation is especially useful to automatically fit the model within the observer to a real fuel cell system.

For the temperature distribution in both gas channels (Fig. 6.5) there is once again no big deviation visible between the three simulation runs since channel inlet temperatures and bipolar plate temperatures are constant boundary conditions and therefore strictly limit possible differences. However, it is visible that the observer reconstructs the actual channel temperatures better than the simulation in all time steps apart from the initial step. Still, the temperature field in the catalyst layers and in the middle of the membrane (Fig. 6.6) are of higher interest since it is not possible to affect these distributions directly by boundary conditions. It is clearly visible how the wrongly initialized parameters affect the uncorrected simulation. After the initialization, it is not possible for the simulation to reach the actual temperature distribution in the

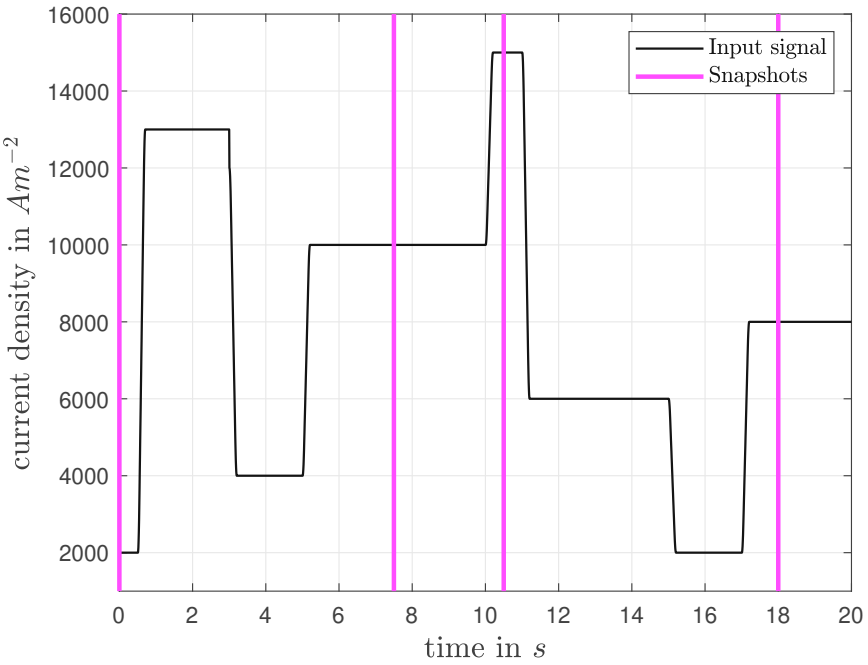

(a) average current density i_{avg}

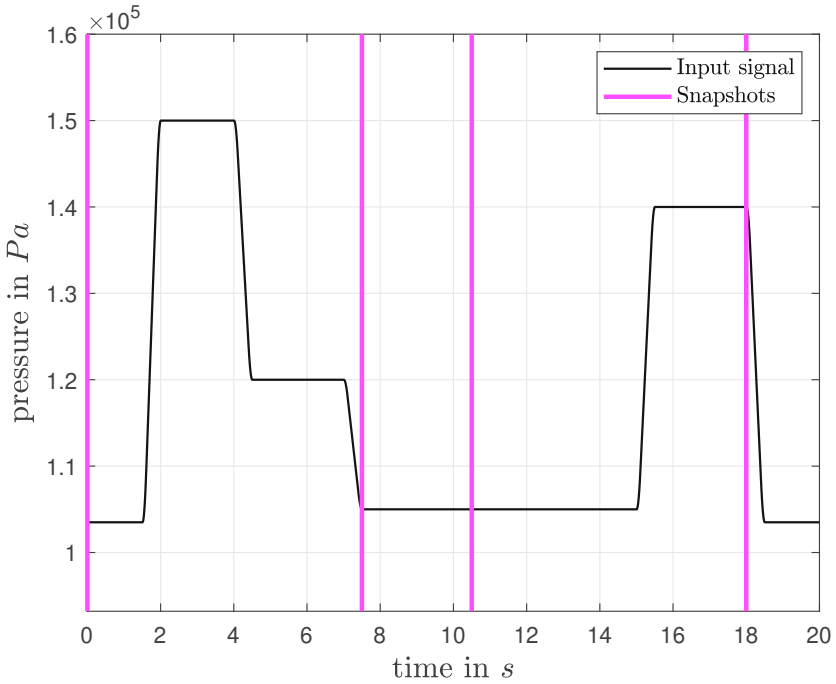

(b) cathode channel inlet pressure p_{in}^{cc}

Figure 6.1: Input signals to system for experiment with parameter estimation

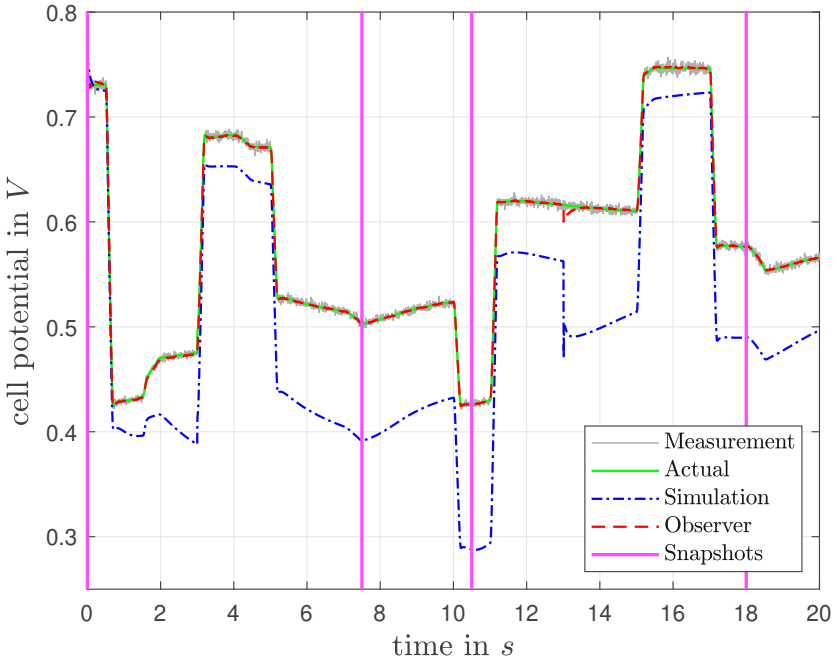

(a) cell potential E_{cell}

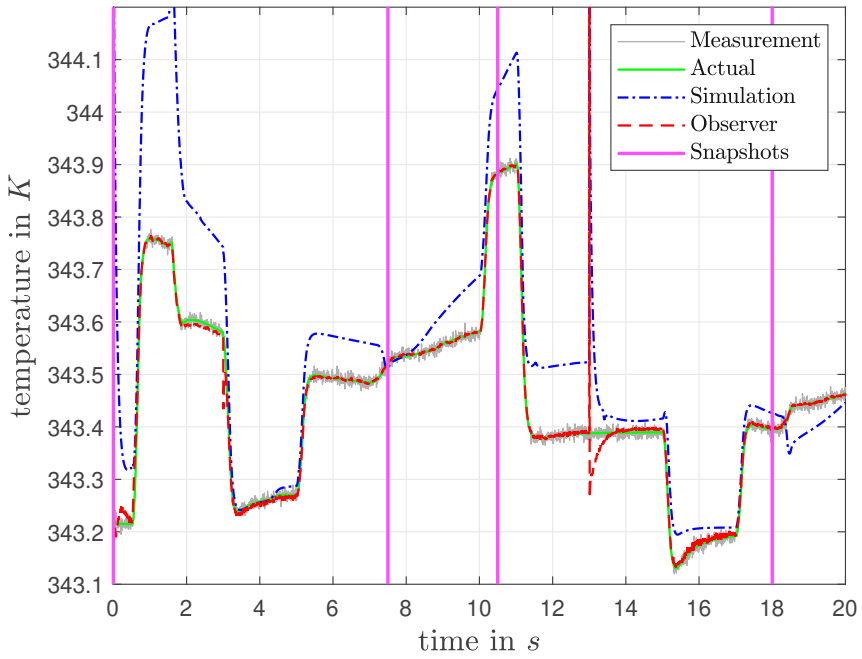

(b) cathode channel outlet temperature T_{out}^{cc}

Figure 6.2: Measured outputs for experiment with parameter estimation

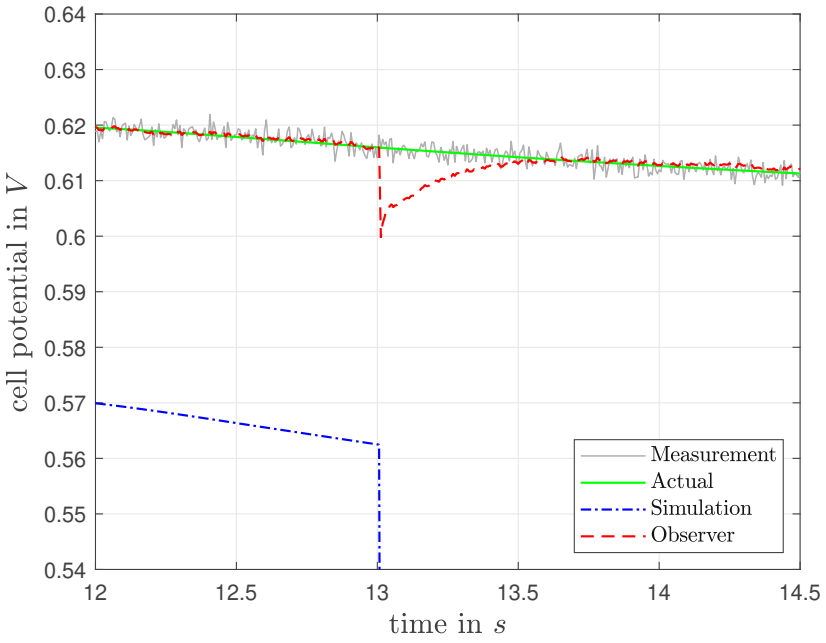

(a) cell potential E_{cell}

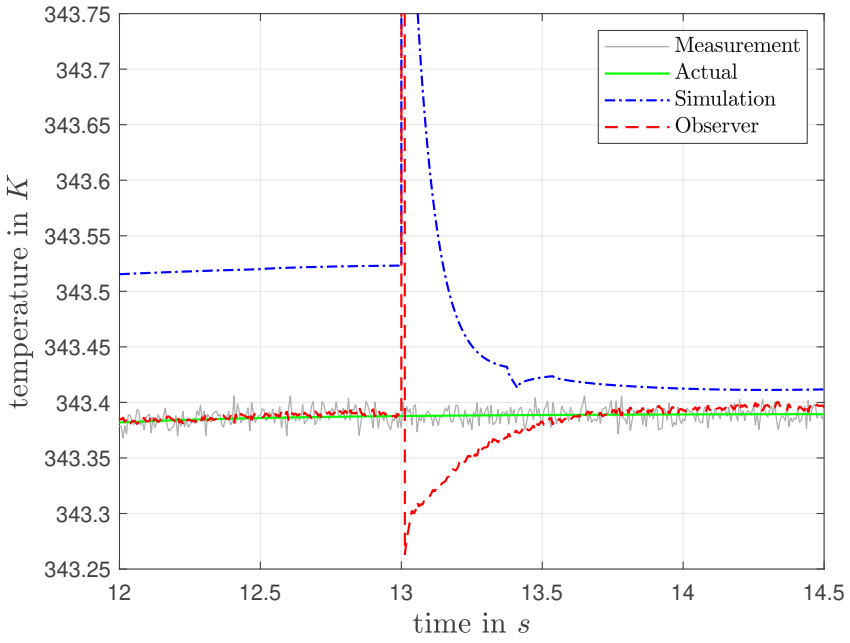

(b) cathode channel outlet temperature T_{out}^{cc}

Figure 6.3: Measured outputs for experiment with parameter estimation (zoom)

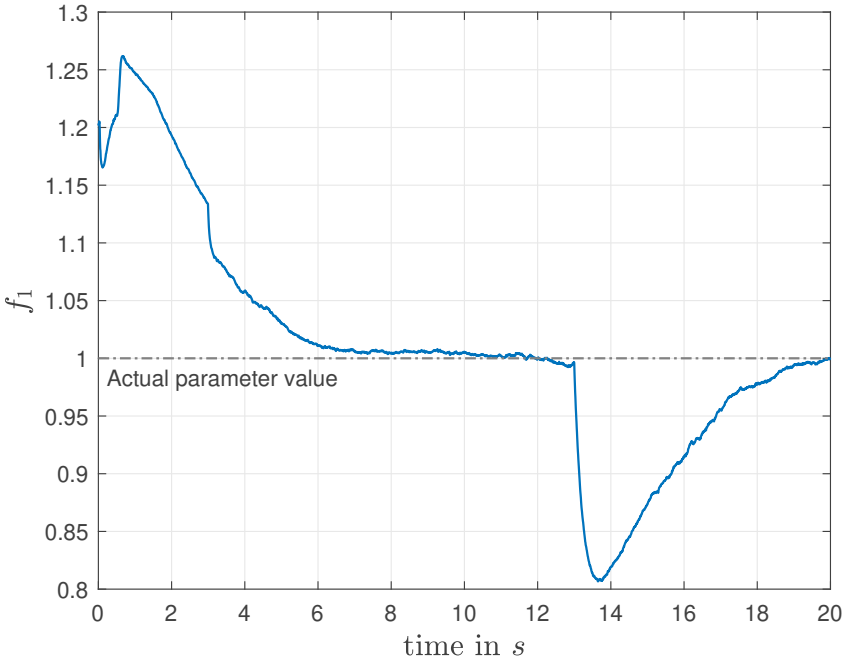

(a) f_1

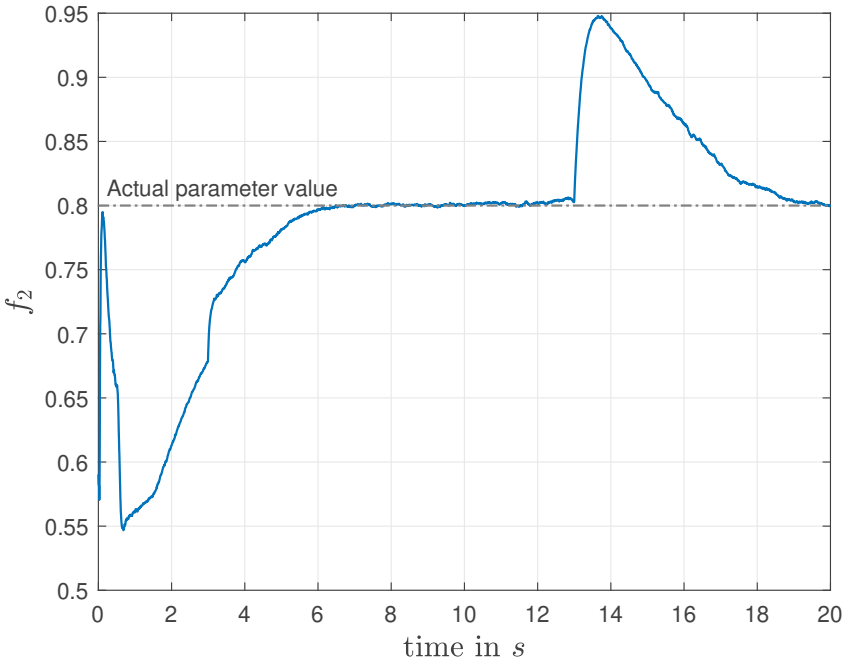

(b) f_2

Figure 6.4: Estimation of membrane ionic conductivity fitting parameters

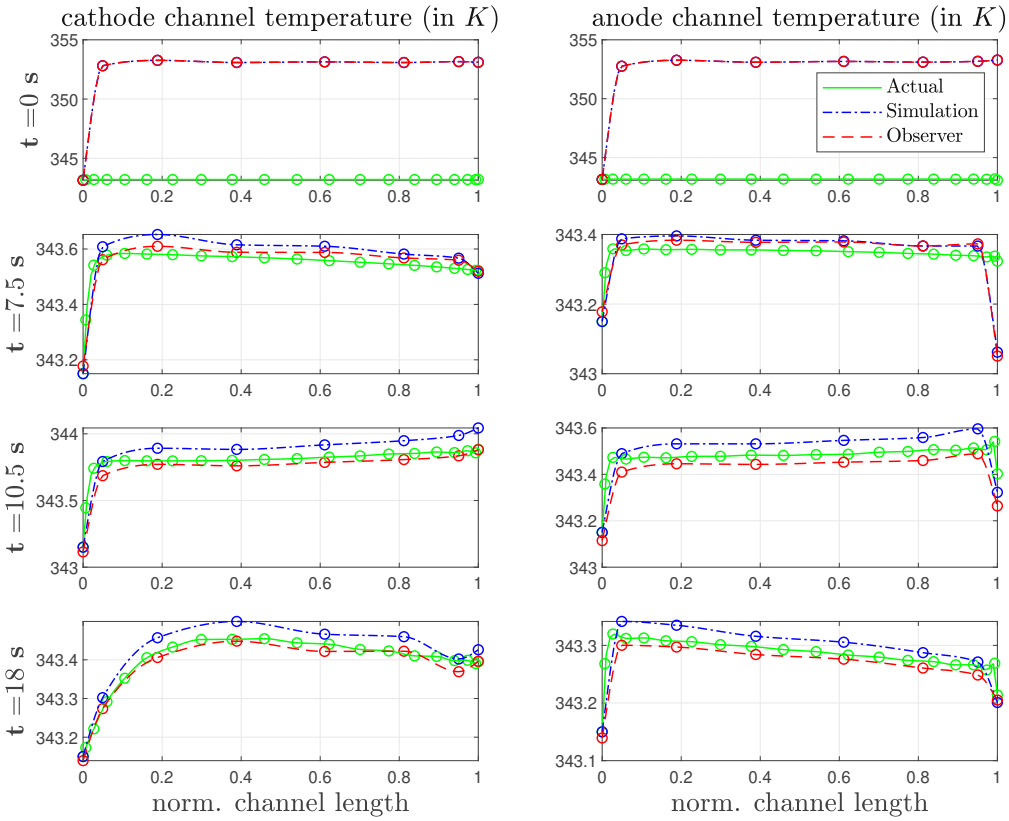

Figure 6.5: Temperature in gas channels for experiment with parameter estimation

membrane and the catalyst layers. The temperature field estimated by the observer, however, shows robust behavior toward wrong initialization of states and parameters and state disturbances and converges toward the true temperature distributions. The temperature difference between simulation and actual distribution might be small in absolute numbers, however, as mentioned in the previous chapter, the temperature gradient within the fuel cell during operation is expected to be $\sim 5-10$ K. This can also be seen when comparing the temperatures in the channel to the membrane temperature at 10.5 s. For the ~ 1 K difference between simulation and actual temperature, this would already mean a $10-20$ % deviation from the true value. Since the polymer membrane is sensitive to temperature, precise estimation is indispensable.

Fig. 6.7 shows the water content in the middle of the membrane and the distribution of the local current density. The current density plots show that the simulation is not

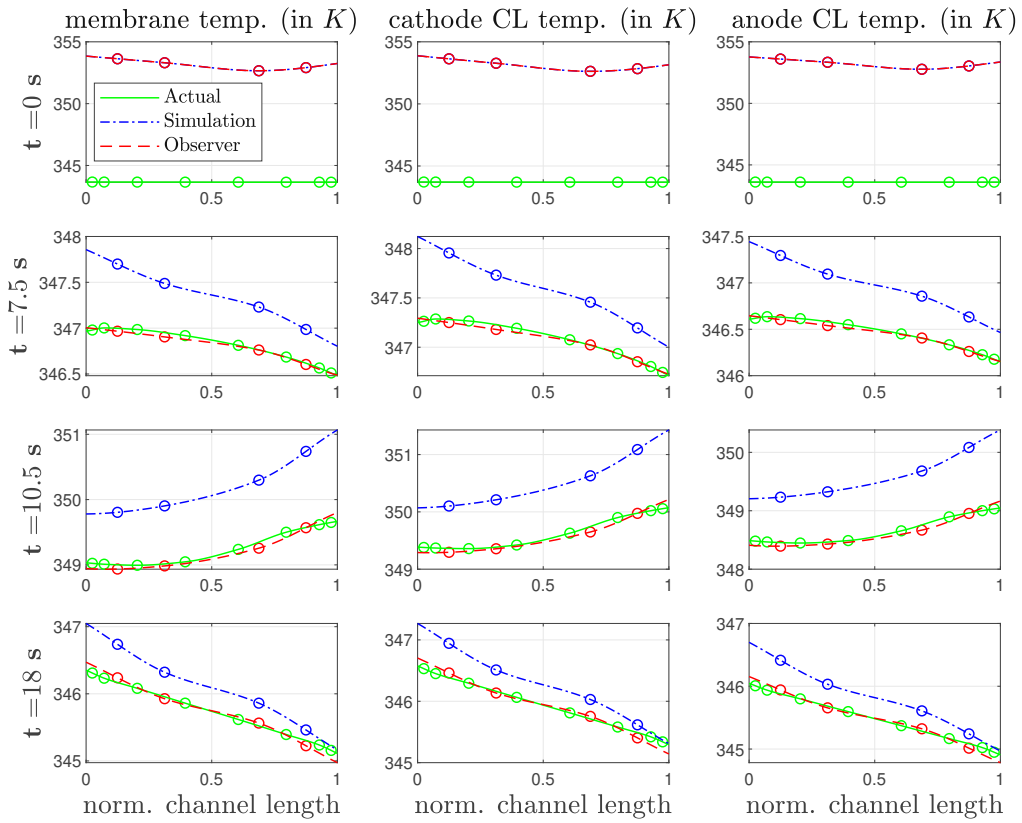

Figure 6.6: Temperature in membrane and catalyst layers for experiment with parameter estimation

able to converge to the true distribution whereas the observer drives the system to the actual distribution already after 7.5 s. Even after the disturbance, the observer converges back to the actual current density distribution fast. For the membrane water content, however, the simulation converges fast as well since the water content does not depend on the (corrected) fitting parameters directly. Furthermore, the fitting parameters converge slower than the membrane water content. This means that the species concentrations of the observer and the simulation converge similarly fast. Even after the re-initialization at $t = 13$ s, the simulation and the observer describe the actual water content equally well.

The distributions of the species concentrations in the cathode and anode gas channel are depicted in Fig. 6.8 and Fig. 6.9, respectively. Similar to the membrane water content, the convergence of the estimated parameters takes longer than the convergence of the

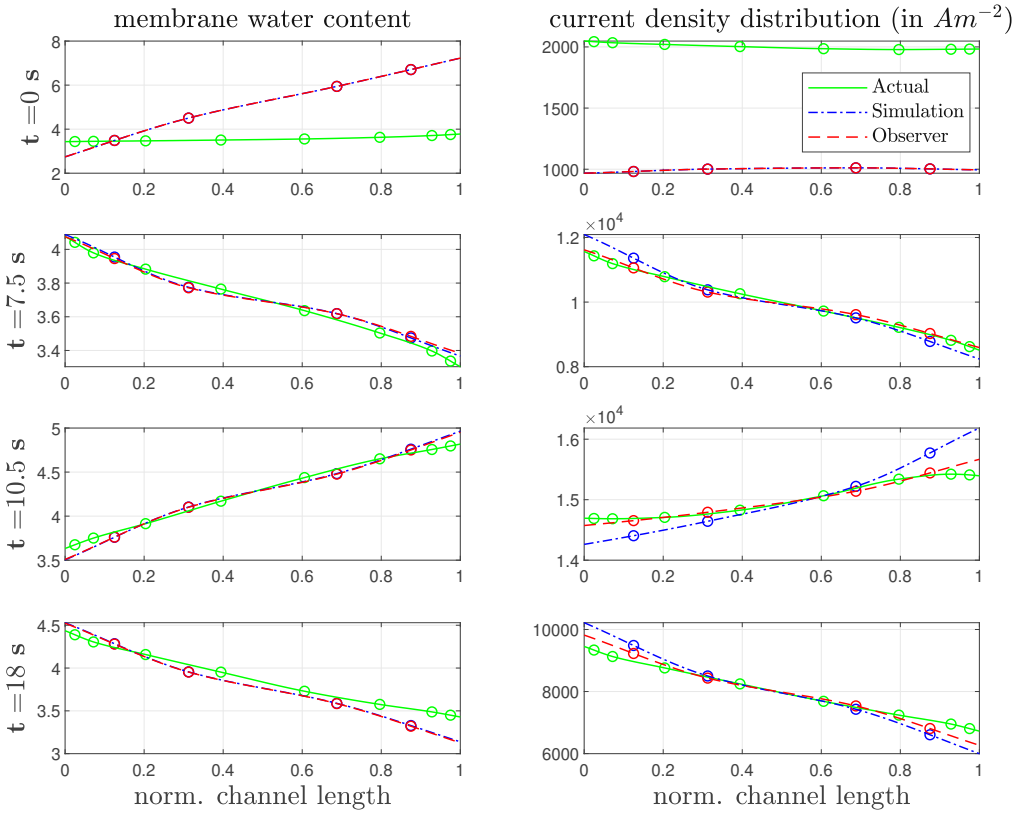

Figure 6.7: Membrane water content & current density distribution for experiment with parameter estimation

simulated distributions. In addition, there is no direct influence of the conductivity fitting parameters on the channel species concentrations, as it is for the cell potential. Therefore, the observer and the simulation converge equally fast to the true species distributions for each component.

The results of the simultaneous state and parameter estimation show that the observer is able to estimate initially unknown parameters and therefore can automatically adapt the underlying model to an actual fuel cell system. The advantage of using additional parameter estimation in the state observer is clearly visible in the signals of cell potential and cathode channel outlet temperature (Fig. 6.2). Without the observer, the cell potential cannot converge toward the true value because of its dependence on the membrane conductivity. The actual internal temperature field of the fuel cell (membrane and catalyst layers) is estimated by the observer nicely as well. States converging

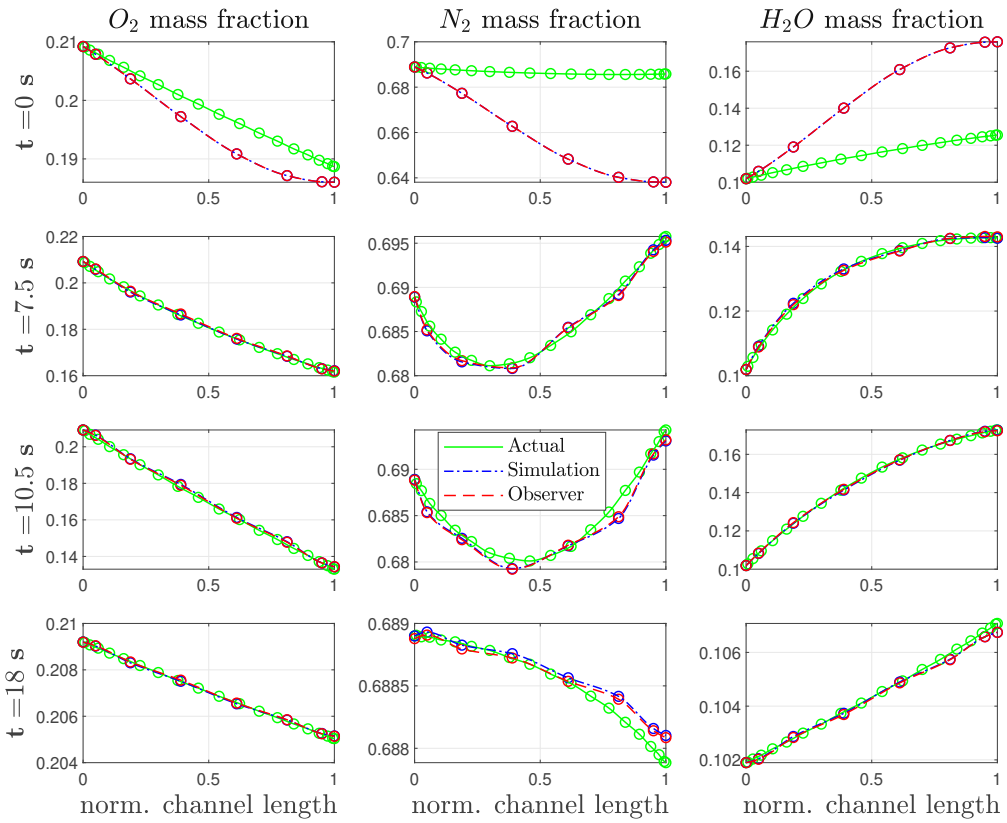

Figure 6.8: Cathode channel species concentrations for experiment with parameter estimation

faster than the parameters without direct dependence on them tend to show equally fast convergence for the simulation and the observer.

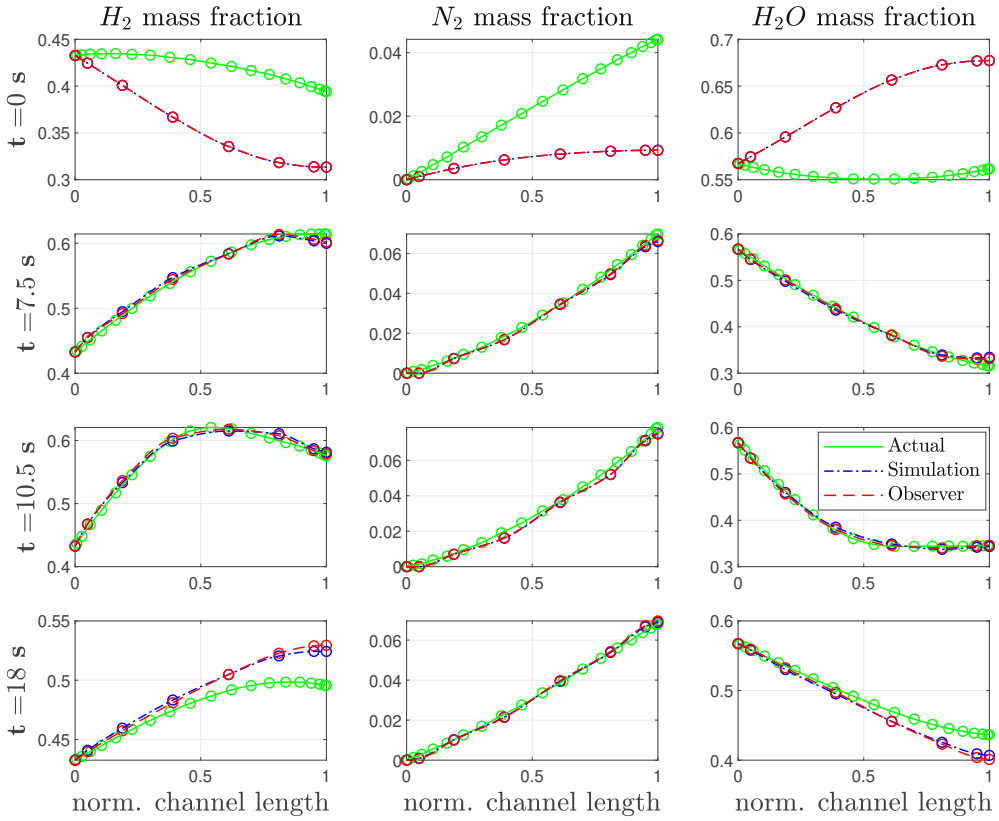

Figure 6.9: Anode channel species concentrations for experiment with parameter estimation

Chapter 7

Conclusion

The use of PEM fuel cells in highly dynamic operations poses a challenge that needs to be managed to establish fuel cell electric vehicles as emission-free alternatives to conventional means of transportation. Transient operations favor the occurrence of adverse fuel cell conditions that lead to accelerated degradation and lifetime reduction. To detect and therefore avoid such conditions, the monitoring of vital fuel cell state distributions is crucial. Internal fuel cell states that cannot be measured directly, can be reconstructed from measurements by state observers using a fuel cell model.

The model used in the observer needs to be a distributed-parameter model in order to estimate state distributions, like temperature, membrane water content, or species concentrations that are vital for detecting adverse fuel cell states, such as hydrogen starvation or membrane drying. To keep computational effort low, a quasi-2D PEM fuel cell model is used. Due to its well-established formulation, also in PEMFC systems ([22, 26]), the observer algorithm is chosen to be an extended Kalman filter algorithm, consisting of a prediction and a correction step [19]. Therefore, the EKF presented in this thesis uses a non-isothermal single-phase quasi-2D PEMFC model to estimate vital fuel cell state distributions where the focus lies on the estimation of the temperature distribution of the fuel cell.

In Chapter 3, the nonlinear distributed-parameter PEM fuel cell model used within the observer is explained. The state vector structures are shown for the gas channels, the gas diffusion layers, and the membrane. The overall state vector consists of the state vector of each cell domain and is used in the linearized-in-time (LIT) system. The entirety of all equations used for modeling the quasi-2D non-isothermal single-phase PEMFC is given in [15] and [14]. This high-order model is used within the EKF prediction step.

The high-order of the used distributed-parameter model leads to high computational

effort of the state estimation. To minimize run-time and allow feasible state estimation, the corrective action of the observer is only computed in the direction of the most dominant system modes. In this work, a reduced-order modal system is derived from the full-order state space system by balanced truncation [31]. Since the balanced truncation only works for linear, scaled systems, the PEMFC model is successively linearized around the current trajectory and scaled to obtain the normalized system Jacobians. This reduced-order modal model is used within the EKF correction step.

The measured outputs of the system are the cell potential E_{cell} and the cathode channel outlet temperature T_{out}^{cc}. With this sensor placement, the most dominant modes are observable and from analyzing the transformation matrix from reduced-order modal space to full-order state space, the state distributions of the FC can be reconstructed.

The observer uses a spatially coarse discretization of the quasi-2D PEMFC model and is validated against a high-resolving discretization of the quasi-2D model that serves as virtual reality. This is done since an actual fuel cell would not allow insight into the actual FC state distributions. The advantage of using a state observer is shown by comparing the estimated states to the simulated states from a coarse-grid quasi-2D simulation without a state observer. Since it is not possible to know the initial state of the actual system, the observer is initialized differently compared to the true system.

In 5.2, the average current density i_{avg} is used as the only dynamic system input. The results show that the observer detects the actual cell potential and cathode channel outlet temperature clearly faster than the simulation without correction despite measurement noise. The actual temperature distribution of the fuel cell is also reconstructed significantly faster with the observer, where the main focus lies on the estimation of the temperature field of the catalyst layers and the membrane. The estimated distributions of the membrane water content, the local current density, and the gas channel species concentrations on anode and cathode side also converge toward the actual distribution in justifiable time.

The observer was tested with a second manipulable system input, the cathode channel inlet pressure p_{in}^{cc}, in 5.3. This is done to investigate the performance of the observer when encountering multiple dynamic boundary conditions. Again, the observer shows fast convergence toward the actual values compared to a simulation without state estimation for all relevant state distributions. The state estimation is therefore proven to be capable of handling multiple excitation signals.

In real-life applications, it is generally not possible to know all system parameters. To

automatically fit the model in the observer to an actual fuel cell, the extension of the observer to simultaneously estimate state distributions and two fitting parameters is presented in 6. For this purpose, the methodology of the state estimation is adapted to handle the simultaneous estimation of unknown fitting parameters. Again, the average current density i_{avg} and the cathode channel inlet pressure p_{in}^{cc} are used as dynamic inputs to the system. As for the states, the parameters are initialized differently because it is not possible to know the real values a priori. The results show that the state observer can estimate the actual parameters simultaneously with the internal state distributions where the state estimation improves with converging parameters. However, the simulation without corrective action cannot adapt its wrongly initialized parameters and therefore is not able to push all states toward the true state distributions.

The presented observer can handle multiple changeable signals as dynamic system inputs and is extendable to a simultaneous state distribution and parameter estimation to automatically adapt its underlying model to an actual fuel cell and therefore can be applied in real-life fuel cell systems. Especially automotive applications, like FCEVs, where highly dynamic operations can easily cause adverse fuel cell conditions are predestinated for the use of the state observer. In upcoming tasks, time-variant parameters that mainly affect degradation and aging effects can be identified and the presented observer can be further adapted to estimate these time-dependent parameters as well.

Bibliography

[1] Frano Barbir. *PEM fuel cells: theory and practice*. Elsevier/Academic Press, Amsterdam ; Boston, 2nd ed. edition, 2013.

[2] Abed Alaswad, Abdelnasir Omran, Jose Ricardo Sodre, Tabbi Wilberforce, Gianmichelle Pignatelli, Michele Dassisti, Ahmad Baroutaji, and Abdul Ghani Olabi. Technical and commercial challenges of proton-exchange membrane (pem) fuel cells. *Energies*, 14(1), 2021.

[3] Tabbi Wilberforce, A. Alaswad, A. Palumbo, M. Dassisti, and A.G. Olabi. Advances in stationary and portable fuel cell applications. *International Journal of Hydrogen Energy*, 41(37):16509–16522, 2016.

[4] Shinichi Sugihara and Hiroshi Iwai. Measurement of transient temperature distribution behavior of a planar solid oxide fuel cell: Effect of instantaneous switching of power generation and direct internal reforming. *Journal of Power Sources*, 482:229070, 2021.

[5] Jian Zhao, Xianguo Li, Chris Shum, and John McPhee. A review of physics-based and data-driven models for real-time control of polymer electrolyte membrane fuel cells. *Energy and AI*, 6:100114, 2021.

[6] Abdelnasir Omran, Alessandro Lucchesi, David Smith, Abed Alaswad, Amirpiran Amiri, Tabbi Wilberforce, José Ricardo Sodré, and A.G. Olabi. Mathematical model of a proton-exchange membrane (pem) fuel cell. *International Journal of Thermofluids*, 11:100110, 2021.

[7] T. E. Springer, T. A. Zawodzinski, and S. Gottesfeld. Polymer electrolyte fuel cell model. *Journal of The Electrochemical Society*, 138(8):2334, aug 1991.

[8] Jay T Pukrushpan, Anna G Stefanopoulou, and Huei Peng. Modeling and control for pem fuel cell stack system. In *Proceedings of the 2002 American Control Conference (IEEE Cat. No. CH37301)*, volume 4, pages 3117–3122. IEEE, 2002.

[9] PR Pathapati, X Xue, and J Tang. A new dynamic model for predicting transient phenomena in a pem fuel cell system. *Renewable energy*, 30(1):1–22, 2005.

[10] Daniel Ritzberger, Christoph Hametner, and Stefan Jakubek. A real-time dynamic fuel cell system simulation for model-based diagnostics and control: Validation on real driving data. *energies*, 13(12):3148, 2020.

[11] Yuyao Shan and Song-Yul Choe. A high dynamic pem fuel cell model with temperature effects. *Journal of power sources*, 145(1):30–39, 2005.

[12] Trung V Nguyen and Ralph E White. A water and heat management model for proton-exchange-membrane fuel cells. *Journal of the Electrochemical Society*, 140(8):2178, 1993.

[13] Guobin Zhang, Zhiming Bao, Biao Xie, Yun Wang, and Kui Jiao. Three-dimensional multi-phase simulation of pem fuel cell considering the full morphology of metal foam flow field. *International Journal of Hydrogen Energy*, 46(3):2978–2989, 2021.

[14] Dominik Murschenhofer, Dominik Kuzdas, Stefan Braun, and Stefan Jakubek. A real-time capable quasi-2d proton exchange membrane fuel cell model. *Energy Conversion and Management*, 162:159–175, 2018.

[15] Florian Altmann. *On multiphase flow and the dynamic temperature distribution in proton exchange membrane fuel cells*. TU Wien, Wien, 2022.

[16] Hao Yuan, Haifeng Dai, Xuezhe Wei, and Pingwen Ming. Model-based observers for internal states estimation and control of proton exchange membrane fuel cell system: A review. *Journal of Power Sources*, 468:228376, 2020.

[17] David G Luenberger. Observing the state of a linear system. *IEEE transactions on military electronics*, 8(2):74–80, 1964.

[18] Rudolph Emil Kalman. A new approach to linear filtering and prediction problems. *Journal of Basic Engineering*, 83(1):95–108, 1960.

[19] Andrew H Jazwinski. *Stochastic processes and filtering theory*. Courier Corporation, 1970.

[20] Simon J Julier and Jeffrey K Uhlmann. Unscented filtering and nonlinear estimation. *Proceedings of the IEEE*, 92(3):401–422, 2004.

[21] Christopher V Rao, James B Rawlings, and David Q Mayne. Constrained state estimation for nonlinear discrete-time systems: Stability and moving horizon approximations. *IEEE transactions on automatic control*, 48(2):246–258, 2003.

[22] Martin Vrlić, Dominik Pernsteiner, Alexander Schirrer, Christoph Hametner, and Stefan Jakubek. Reduced-dimensionality nonlinear distributed-parameter observer for fuel cell systems. *Energy Reports*, 10:1–14, 2023.

[23] Julio Luna, Attila Husar, and Maria Serra. Nonlinear distributed parameter observer design for fuel cell systems. *International Journal of Hydrogen Energy*, 40(34):11322–11332, 2015.

[24] José Manuel Andújar and Francisca Segura. Fuel cells: History and updating. a walk along two centuries. *Renewable and sustainable energy reviews*, 13(9):2309–2322, 2009.

[25] Kenneth A. Burke. Fuel cells for space science applications. Technical Report NASA/TM-2003-212730, NASA, 2003.

[26] Lukas Böhler, Daniel Ritzberger, Christoph Hametner, and Stefan Jakubek. Constrained extended kalman filter design and application for on-line state estimation of high-order polymer electrolyte membrane fuel cell systems. *international journal of hydrogen energy*, 46(35):18604–18614, 2021.

[27] Shahrokh Akhlaghi, Ning Zhou, and Zhenyu Huang. Adaptive adjustment of noise covariance in kalman filter for dynamic state estimation. In *2017 IEEE power & energy society general meeting*, pages 1–5. IEEE, 2017.

[28] Dan Zwillinger. *CRC standard mathematical tables and formulas*. Advances in applied mathematics. CRC Press, Boca Raton, 33rd edition edition, 2018.

[29] MathWorks. Symbolic math toolbox documentation, 2023. `https://de.mathworks.com/help/symbolic/` [Accessed: 2023-08-04].

[30] Peter Benner, Serkan Gugercin, and Karen Willcox. A survey of projection-based model reduction methods for parametric dynamical systems. *SIAM review*, 57(4):483–531, 2015.

[31] Bruce Moore. Principal component analysis in linear systems: Controllability, observability, and model reduction. *IEEE transactions on automatic control*, 26(1):17–32, 1981.

[32] Dominik Pernsteiner, Alexander Schirrer, Lukas Kasper, René Hofmann, and Stefan Jakubek. State estimation concept for a nonlinear melting/solidification problem of a latent heat thermal energy storage. *Computers & Chemical Engineering*, 153:107444, 2021.

[33] Rudolf Emil Kalman. On the general theory of control systems. In *Proceedings First International Conference on Automatic Control, Moscow, USSR*, pages 481–492, 1960.

[34] Rudolf Emil Kalman. Mathematical description of linear dynamical systems. *Journal of the Society for Industrial and Applied Mathematics, Series A: Control*, 1(2):152–192, 1963.

[35] Robert Hermann and Arthur Krener. Nonlinear controllability and observability. *IEEE Transactions on automatic control*, 22(5):728–740, 1977.

[36] Emmanuel D Blanchard, Adrian Sandu, and Corina Sandu. Parameter estimation method using an extended kalman filter. In *Proceedings of the Joint North America, Asia-Pacific ISTVS Conference and Annual Meeting of Japanese Society for Terramechanics*, 2007.

[37] Mathieu Bressel, Mickael Hilairet, Daniel Hissel, and Belkacem Ould Bouamama. Extended kalman filter for prognostic of proton exchange membrane fuel cell. *Applied Energy*, 164:220–227, 2016.